Characterizing low-sulfide instrumented waste-rock piles: image grain-size analysis and wind-induced gas transport

by

Xiaotong Chi

A thesis
presented to the University of Waterloo
in fulfillment of the
thesis requirement for the degree of
Master of Science
in
Earth Sciences

Waterloo, Ontario, Canada, 2010

©Xiaotong Chi 2010

AUTHOR'S DECLARATION

I hereby declare that I am the sole author of this thesis. This is a true copy of the thesis, including any required final revisions, as accepted by my examiners.

I understand that my thesis may be made electronically available to the public.

Abstract

This study is part of the Diavik Waste-Rock Pile Project taking place at the Diavik Diamond Mine in the Northwest Territories, Canada. The project involves the construction of three 15m-scale low sulfide test waste-rock piles and monitoring of fluid flow, geochemical reactions, heat and gas transport within the waste-rock piles and characterization of the physical properties of the waste-rock piles. The focus of this thesis is characterizing grain-size distribution of the waste-rock and quantifying gas transport in the test waste-rock piles.

Grain size of waste rock ranges from millimeters to meters. Sieve analysis typically only provides information of grain size <0.1 m at a single location. A computer program was developed using digital image-processing techniques to obtain a spatial grain-size distribution from photographs of tip faces of the test waste-rock piles acquired in the field. The program characterizes grain size >0.1 m and employs a region-growing algorithm for segmentation of waste-rock grains with pre- and post-processing techniques to improve the accuracy of segmentation. The program was applied to photographs of six different tip faces of the test waste-rock piles. For grain size <0.1 m, data from sieve analyses were attached to the grain-size curves generated from image grain-size analyses to obtain a full spectrum grain-size analyses ranging from boulders to fines. The results show that fine fractions are retained at the top of the tip faces and grain size increases non-linearly from top to bottom of a waste-rock pile. Calculations show that although the greatest mass is associated with the medium and coarse fractions, the greatest surface area is associated with the fine fractions. The results are consistent with field observation that the initial solute concentrations are greatest at the top of the pile and saturated hydraulic conductivity are lower at the top of the

pile than in the pile interior. Statistical moments show that the test waste-rock piles have mean grain size of granules and are very poorly sorted, coarse skewed and leptokurtic. Permeability is calculated using empirical formulae and good agreement is obtained between calculated values and field measurements. The heterogeneity of grain size obtained from this study can provide a basis for future modeling efforts.

Gas transport analysis focused on 1) substantiating the relationship between wind flow external to the waste-rock pile and gas pressures within the pile, 2) determining the gas flow regime in the pile, and 3) quantifying the temporal variation in wind speed and direction and determining the relevant time scales. Differential gas pressures were measured in 2008 at 49 locations within one of the three test waste-rock piles and 14 locations on the surface of the pile at one-minute intervals. Wind speed and direction were measured at 10-min intervals. Correlations between wind vectors and pressure measurements show that the wind influences pressure fluctuations in the test pile. The strength of the correlation is roughly inversely proportional to the distance between measurement ports and the atmospheric boundary. The linear relationship between internal pressure measurements and surface pressure measurements demonstrate that gas flow is Darcian within the test waste-rock pile. Spectral analysis of wind data and a one-dimensional analytical solution to the flow equations show that the persistence of wind in a certain direction has most pronounced effects on transient gas flow within the pile. The penetration depth of wind-induced gas pressure wave is a function of the periodicity of the wind and permeability of the waste-rock pile.

Acknowledgements

I sincerely thank:

Dr. David Blowes

Dr. Marek Stastna

Dr. Carol Ptacek

Dr. Walter Illman

Brenda Bailey

Dr. Richard Amos

Dr. Leslie Smith

My Parents: Guodong and Ying

Ashley Stanton

DDMI

Dr. David Sego

Stacey Hannam

NSERC

Anyone I may have forgotten

Dedication

To my loving wife, Jingying Zhang-Chi.

Table of Contents

List of Figures

Chapter 2 Waste-rock pile grain-size analysis using digital image processing

Chapter 3 Implications of wind-induced pressure in a waste rock pile

List of Tables

Chapter 2: Waste-Rock Pile Grain-Size Analysis Using Digital Image Processing

Chapter 1: Introduction

Open-pit mining results in the generation of waste rock, which is the large volume of rock whose mineral content is too low to be economically recovered. Waste rock is typically retained in large unsaturated stockpiles at the mine site. When sulfide minerals are present in waste-rock piles, acid mine drainage (AMD) can be produced by sulfide oxidation. Waste-rock piles that have a relatively low sulfide content, also may have low acid neutralizing potential, and therefore may generate AMD. The generation of AMD can persist for a long period of time and is one of the most costly environmental challenges for the mining industry (Singer and Stumm, 1970; Nordstrom and Alpers, 1999; Moncur et al., 2005).

Sulfide oxidation is a complex process involving several steps of reactions. The generally accepted overall reaction for pyrite oxidation is:

$$FeS_2+3.5O_2+H_2O\rightarrow Fe^{2+}+2SO_4^{2-}+2H^+ \quad (1)$$

The processes in waste rock piles that affect the rate of sulfide oxidation include gas transport, thermal transport, water flow, and geochemistry. Gas transport controls oxygen supply and becomes the limiting factor of sulfide oxidation in many cases (Cathles and Apps, 1975; Pantelis and Ritchie, 1992; Ritchie, 1994; Garvie et al., 1997: Lefebvre et al., 2001a, b). The mechanisms of gas transport include diffusion, advection due to thermal gradients, barometric pumping and wind-driven pressure gradients (Ritchie, 1994; Bennett et al., 1995; Lefebvre et al., 2001a; 2001b; Massmann and Farrier, 1992; Auer et al., 1996; Anne and Pantelis, 1997; Ritchie and Miskilly, 2000; Moghtaderi et al., 2000).

Gas transport has been studied extensively using numerical models. Bennett et al. (1995) applied the numerical model FIDHELM, which accounts for gas transport caused by convection and diffusion, to a waste-rock pile at the Heath Steele mine in New Brunswick, Canada with the goal of determining gas-transport mechanisms. Using homogeneous domain and constant boundary conditions, the model was unable to predict oxygen concentrations observed in the field. The authors concluded that the pressure change at the boundary, and heterogeneity might have contributed to the observed variations in oxygen concentration. Lefebvre et al. (2001a,b) conducted a multiphase modeling study using TOUGH AMD to simulate sulfide oxidation in two different waste-rock piles and proposed gas-transport control strategies. Anne and Pantelis (1997), and Ritchie and Miskilly (2000) coupled computational fluid dynamics (CFD) models to simulate wind-induced gas transport. The results show that wind flow may have significant effects on oxygen transport and sulfide oxidation. Amos et al. (2009a,b) measured wind-induced pressure gradients in a waste-rock pile and compared results to a numerical model using a homogeneous domain. The discrepancy between the field observations and modeling results suggests that the heterogeneity of the waste-rock pile influences gas transport significantly.

Thermal transport plays a key role in limiting sulfide oxidation, especially in cold northern regions. This limitation occurs because when the temperature drops below zero, water, one of the reactants in the sulfide oxidation reaction freezes. Furthermore, thermal conditions affect gas convection within the waste rock piles. Kyhn and Elberling (2001) demonstrated that thermal covers are effective in limiting acid mine drainage from mine tailings using a one-dimensional numerical model. Arenson and Sego (2007) showed that a

coarse rock cover on top of tailings ponds may promote freezing of the tailings underneath. Ritchie (1994) identified thermal gradient as the most important process in driving gas convection in waste-rock piles.

Water flow provides reactants for sulfide oxidation and also carries oxidation products. Therefore, understanding water flow is key in determining the extent and duration of acid mine drainage. Water flow in unsaturated water rock piles is greatly influenced by the heterogeneity. Preferential flow patterns often are observed in waste-rock piles. Murr et al. (1981) conducted leaching and dye-staining experiments on mine heap leach materials and found relatively small amounts of waste rock produced the majority of the leached metals. Nichol et al. (2004) described a tracer test on a waste-rock pile at Cluff Lake mine, Canada, but was unable to quantify wetting front velocity and the relative contributions from matrix flow and preferential flow.

Ultimately, the extent of AMD generation is determined by geochemical reactions. Sulfide oxidation is affected by mineralogy, surface area and microbiology. Mineralogy controls the stoichiometry of the oxidation reaction and hence the amount of acid and metal released by the reactions. Material with a larger surface area reacts faster than the same material with a smaller surface area because the larger surface area allows oxygen to reach the reaction site faster (Berner, 1980; Hollings et al., 2001). Heterogeneity controls the distribution of surface area and hence the reaction rate. Bacteria may act as catalysts for sulfide oxidation and have significant effect on the rate of sulfide oxidation. *A. thiooxidans* and *A. ferrooxidans* are the two most commonly found bacterial species in mine wastes (Gould and Kapoor, 2003). *A. ferrooxidans* requires O_2 and CO_2 for growth. Gas transport

controls O_2 and CO_2 supply and is an important factor controlling maintaining bacterial growth and the sulfide oxidation rates.

Coupling between the physical and biogeochemical processes active in a waste-rock pile is highly complex. Cathles and Apps (1975) developed a one-dimensional transient model of copper-waste dump incorporating an oxygen balance, a heat balance and air convection and applied the model to a small copper waste dump. Pantelis and Ritchie (1992) identified the physiochemical processes and suggested when the geochemical reactions do not limit the oxidation, physical process that controls oxygen supply controls AMD production. Hockley et al. (1995) identified the types of coupling between physiochemical processes into one-way, two-way and indirect coupling. Lefebvre et al. (2001a) proposed an oxygen-supply conceptual model: gas first enters waste rock piles through diffusion and wind-induced gradients. Because the oxidation of pyrite is highly exothermic, it creates a thermal gradient, which drives convective gas transport. Also, as oxygen is consumed by sulfide oxidation, the concentration gradient between the interior of the waste-rock pile and the atmosphere drives oxygen transport. The concentration of the effluent is controlled by the coupling between unsaturated water flow and chemical reactions. Malstrom et al., (2000) suggested the difference in reaction rate between laboratory tests and field investigations is the result of significant channelization of flow and incomplete flushing of oxidation products. Smith and Beckie (2003) showed that the greatest uncertainty in predicting solute mass loading is associated with the quantification of transient unsaturated flow. Wagner et al. (2006) monitored the geochemical and hydrological condition of an instrumented waste rock pile over a period of 4 years. The authors found that sulfate concentrations negatively

correlate with flow rates during short periods of time such as an individual rainfall event when the macro flow is active but positively in the long term (monthly scale).

Much of the discrepancy between numerical modeling results and field observations of gas transport (Bennett et al., 1995; Amos et al., 2009) and water flow (Smith and Beckie, 2003; Neuner 2009) are due to lack of knowledge of heterogeneity. Reactive transport simulations also are influenced by heterogeneity because they are linked to hydrological models. In addition, the grain-size distribution and particle surface area provide a basis for estimates of the rate of sulfide oxidation. Much effort has been put into characterizing heterogeneity of waste-rock piles. Stockwell et al. (2006) conducted sieve analysis on over 60 samples at random locations in a waste-rock pile. The results showed a large variation of grain size but similar grain-size distributions. The authors did not account for particles > 0.1m due to the limitation posed by sieve size. Smith (2009) conducted grain size analysis on over 500 samples from two different waste-rock piles and measured sulfur content of various grain size fractions. The author also conducted a single large-scale grain-size measurement. Traditional sieve analysis is limited by sieve size and is poorly suited for analyzing waste-rock piles that contain large particles.

This thesis addresses two fundamental questions: how can the heterogeneity of the waste-rock piles be characterized better to determine the effects of physical characteristics on transport processes and AMD generation; and what is the impact of wind-induced gas transport on the processes involved in AMD generation from waste-rock piles.

1.1 Site description

This thesis is part of a waste-rock research project taking place at the Diavik Diamond Mine in Canada's Northwest Territory. The Diavik Diamond Mine is located on a 20 km^2 island in Lac de Gras, approximately 300 km from Yellowknife, NWT, Canada. The Diavik mine consists of three kimberlite pipes located beneath the waters of Lac de Gras with a total mine life of 16 to 22 years (DDMI, 2009). The mine started as an open-pit mine and, at the time of this study, is in transition into underground mining operations.

The Diavik country rock is comprised of approximately 75% granites, 14% granitic pegmatites, 10% metasedimentary biotite schists and 1% diabase dykes. The granite and granitic pegmatite contain only trace amount of sulfide minerals and are considered to be non-acid generating (Smith, 2009). However, because the carbonate content of this rock is very low (Smith, 2009), their neutralization potential also is very limited. The biotite schist contains the sulfide mineral pyrrhotite ($Fe_{1-x}S$), which oxidizes rapidly in the open air (Jansen et al., 2000). The carbonate content of the biotite schist also is very low (Smith, 2009). Static tests indicate biotite schist is potentially acid generating due to the balance between acid generating potential and acid neutralization capacity. Diabase dykes are geochemically insignificant due to their small volume.

Country rock (waste rock) excavated during mining operations at Diavik Diamond Mine is analyzed for sulfur content and segregated into Type I, Type II and Type III. Type I rock is comprised primarily of non-acid generating granite with sulfur content < 0.04 wt% S and is primarily used as construction material. Type II rock is predominantly granite with some biotite schist having sulfur content of 0.04 to 0.08 wt% S and is considered to have

little acid generating potential. Type III rock is classified as having acid-generating potential with sulfur content > 0.08 wt% S and is comprised of granite with a greater proportion of biotite schist.

Three instrumented waste-rock piles were constructed using the Diavik country rock from 2004 to 2007. The piles were designated Type I 'TI', Type III 'TIII', Test Cover 'TC' based on their country-rock type. The TI pile is constructed with Type I rock and the TIII pile is constructed with rock designated as Type III within the open pit. The TC pile has a core of TIII rock and an engineered cover composed of a 1.5 m layer of till overlain by 3 m of TI rock. Chemical analysis of samples collected during construction indicate the Type I test pile has an average sulfide content of 0.035 wt. %, the Type III test pile has an average sulfide content of 0.053 wt. % S and the interior of the TC pile has an average sulfide content of 0.082 wt.%. S.

The test piles are 15 m high with an upper surface area of 20 m by 50 m. The angle of repose is about 37.5 degrees (1.3 horizontal vs. 1 vertical) for the TI and TIII piles and 18.4 degrees for the TC pile (3 horizontal vs. 1 vertical). The test piles were constructed using standard waste-dump method from an access ramp. Instruments were installed on the base of the pile and tip faces of the piles. Instruments installed include: a basal drain system on an impermeable liner at the base of each pile to capture the drainage water, soil-water solution samplers (SWSS) to analyze pore-water chemistry, time-domain reflectometer (TDR) probes to measure volumetric water content, thermistors to monitor the thermal state of the piles, gas-sampling lines to measure O_2, CO_2 and differential pressure, air-permeability probes to obtain point permeability measurements, thermal conductivity access ports, and

microbiology access ports to determine bacteria population (Smith, 2009). The instrumentation was designed to allow three dimensional analysis and modeling of the three piles.

1.2 Scope

This thesis consists of four chapters featuring image grain-size analysis of the TI and TIII test piles (Chapter 2) and data analysis and modeling of gas transport in the TIII test pile (Chapter 3). These two chapters are written in journal article format. Chapter 1 provides a global introduction and Chapter 4 provides conclusions and recommendations for future work.

Chapter 2 of this thesis describes the development and application of an image grain-size analysis method to obtain grain-size information from digital photographs. These grain-size analyses were used to assess the spatial variability of grain size within the test waste-rock piles, and to determine the presence of any systematic trends in grain-size distribution. In addition, the grain-size measurements were used in conjunction with previously established correlation techniques to estimate the permeability of the test piles. Comparisons between the estimated permeability values and measurements of gas permeability made at the field site indicate close agreement between these estimates. The grain-size distribution information was used to assess the spatial variability of permeability.

Chapter 3 of this thesis focuses on wind-induced gas transport. Wind-induced gas transport in waste-rock piles is the less well understood than diffusion and convection. Most studies of wind-induced gas (oxygen, in particular) transport employ modeling tools (Anne

and Pantelis, 1997; Ritchie and Miskilly, 2000; Moghtaderi et al., 2000). There are few field investigations of wind-induced subsurface gas transport. Weeks (1993) used regression analysis to correlate gas discharge from an open borehole in Yucca Mountain to wind speed and wind direction. Amos et al. (2009a,b) presented wind-induced pressure gradients in a test waste-rock pile and compared the results to numerical models. However, Amos et al. (2009a, b) did not quantify the relationship between wind and pressure change within the waste-rock pile. Chapter 3 of the thesis provides a more in-depth investigation the pressure data presented by Amos et al. (2009a,b) and describes a transient model of wind-induced pressure fluctuation in the test waste-rock pile.

Chapter 2: Waste-rock pile grain-size analysis using digital image processing

2.1 Overview

Recent developments in digital image processing provide an opportunity to gain a better understanding of large-scale grain-size distribution that is otherwise difficult to obtain through mechanical sieve analysis. An innovative method to obtain grain-size distribution information from photographs of waste-rock piles was developed and applied to a well-characterized study site in the Canadian arctic. The method is based on a region-growing algorithm with edge enhancement and image dilation as pre- and post-processing techniques and demonstrates sound reproducibility. The method was applied to photographs of six exposed faces of two test-scale waste-rock piles. The results are presented both as grain-size distribution curves and d50 contours. The results show that fine fractions are retained at the top of the tip faces and grain size increases non-linearly from top to bottom of the test-scale waste-rock pile. Calculations show that although the greatest mass is associated with the coarse fractions, the greatest surface area is associated with the fine fractions. Statistical moments demonstrate that these waste-rock piles have mean grain size of granules and are very poorly sorted, coarse skewed and leptokurtic. Field large-scale grain-size measurements are consistent with the image grain-size analysis results. Permeability is calculated using Hazen and Kozeny-Carmen empirical formulae, and reasonable agreement between field and laboratory measurements was obtained. The results also are consistent with the observation that the initial solute concentrations are greatest at the top of the pile and saturated hydraulic conductivity is lower at the top of the pile than in the pile interior.

2.2 Introduction

Mining requires the excavation of large volumes of rock to gain access to ore bodies. Rock with a mineralized content too low to be economically recovered as ore usually is retained in unsaturated waste-rock piles at the mine site. The oxidation of sulfide minerals

such as pyrite and pyrrhotite in waste-rock piles has the potential to lead to the release of acid mine drainage (AMD) that may pose an environmental threat (Ritchie, 2003).

Much effort has been put into characterizing waste-rock piles in the last decade (Lefebvre et al., 2001a; Tran et al., 2003; Ritchie, 2003; Sracek et al., 2004; Montero et al., 2005; Stockwell et al., 2006; Azam et al., 2007). One property of primary concern is the grain-size distribution of a pile. Grain size controls key parameters such as reactive surface area and permeability of the pile, and thus controls various processes such as fluid flow, chemical composition and the oxidation rate of sulfide minerals. Hollings et al. (2001) showed that oxidation of pyrite strongly depends on grain size using laboratory kinetic cells. Through numerical modeling studies, Molson et al. (2005) suggest sulfide oxidation may vary two orders of magnitude due to small changes in moisture content and grain size. Smith (2009) showed that the fine fraction of waste rock tends to have higher sulfur content.

Waste-rock piles contain variable grain sizes (Munroe et al., 1999). The most common and routinely used method to determine grain-size distribution, sieve analysis, is limited by the largest sieve size and only reveals grain-size distribution at a single sampling location. For the results to be representative of a large pile, large numbers of samples need to be collected and analyzed. Stockwell et al. (2006) conducted sieve analysis on over 60 samples at random locations in a test waste-rock pile, and results showed a large range of grain sizes but similar grain-size distributions. Smith (2009) conducted grain-size analysis on over 500 samples from two different test-scale waste-rock piles and sulfur content of various grain-size fractions was measured. These analyses only considered grain size of the less than < 0.1m fraction. Little work has been done to characterize the two-dimensional spatial variation of waste-rock grain sizes considering the full spectrum of grain size within the waste-rock piles. In other fields of science and engineering, researchers have attempted grain-size analyses using digital image processing (DIP) techniques and yielded encouraging results (Mora et al., 1998; Kwan et al., 1999; Mora and Kwan, 2000; Fernlund, 2005a, b, c, Igathinathane et al. 2008). However, images for these methods are acquired in highly controlled laboratory environments. Waste-rock images taken from the field suffer from problems such as shadows and blurry rock grain boundaries caused by natural lighting and

limited resolution that pose considerable challenges to digital image processing. The objective of this study is to develop an image analysis technique to provide information on the full spectrum of grain size within a test-scale waste-rock pile, ranging from fines to boulder size. The technique is applied to a well- characterized study site.

2.3 Background

Three test-scale waste-rock piles ("test piles) were constructed at the Diavik Diamond Mine located 300 km northeast of Yellowknife, NWT, Canada and from 2004 to 2007. The test piles are approximately 15 m high and were instrumented so that detailed measurements can be obtained including water flow, aqueous chemistry, gas pressure and concentration, temperature and microbiological evolution. During construction samples were collected for the grain-size and sulfur and carbon analyses (Smith, 2009). The piles were named Type I 'TI', Type III 'TIII', and Test Cover 'TC' (Figure 2 - 1). The TI test pile is comprised primarily of non-acid generating rock with average sulfur content of 0.035 wt% S. The TIII test pile is classified as having acid-generating potential with average sulfur content of 0.053 wt% S. The TC test pile contains TIII core with an engineered cover composed of a 1.5 m layer of till overlain by 3 m of TI rock. The TI and TIII piles are the focus of this study.

The test piles were constructed using standard mining equipment dumping waste rock from an access ramp. Both end dumping with haul trucks and dozer push dumping techniques were used. The test piles are 15 m high. The upper surfaces are 20 m by 50 m, and the angle of repose is approximately 37.5 degrees (1.3 horizontal vs. 1 vertical) for the TI and TIII piles. The rock piles have grain sizes ranging from sub-millimeters to meters. During the construction samples of < 50 mm fraction were taken for grain-size analysis according to ASTM standard D422-63 (ASTM, 2002). A total of 244 samples were taken from the TI pile and 313 samples were collected from the TIII pile. The d50, the diameter that 50 % of the material is finer than, is approximately 7 mm for the < 50 mm fraction of the TIII and 9 mm for the < 50 mm fraction of the TI pile (Neuner, 2009). Two large-scale grain size measurements for the <900 mm fraction of the TI and TIII pile were taken: one consisting of a single truck load of TI run of mine (ROM) collected prior to construction of

the test piles in 2006 (Neuner, 2009) and another consisting of a single truck load of TIII ROM collected after construction in 2010.

2.4 Methods

2.4.1 Digital images

Images of multiple colors were represented as stacking a group of single-color images. The digital photographs taken for the project were acquired in RGB color format, which consists of a *R*ed matrix, a *G*reen matrix and a *B*lue matrix. The three matrices were overlaid to generate a variety of colors. The photographs of waste rock were fairly monotonic. All three matrices had similar pixel intensity distribution and provide similar information and one matrix was sufficient to represent the features in the image. Each single-color digital image was represented as an intensity matrix. Each pixel in the image has a unique entry *(x, y)* in the matrix, and was assigned a value corresponding to the intensity of the pixel. In Matlab coordinate convention, an *N* pixel x *N* pixel intensity image was represented in matrix form as:

$$\begin{bmatrix} f(1,1) & f(1,2) & f(1,3) & \dots & f(1,N-1) \\ f(2,1) & f(2,2) & f(2,3) & .... & \dots \\ f(3,1) & f(3,2) & f(3,3) & \dots & \dots \\ \dots & \dots & \dots & \dots & \dots \\ f(N-1,1) & \dots & \dots & \dots & f(N-1,N-1) \end{bmatrix}$$

Photographs for image analysis were taken of the exposed tip faces of the TI and TIII piles. These exposed faces include the east, west and north faces of the TI pile (TIE, TIW and TIN, respectively) and the north, south and west faces of the TIII pile (TIIN, TIIIS and TIIIW, respectively). Photographs of the faces were taken with a Nikon D5000 digital camera from ground surface in May 2010. The distance from the foot of the pile to the camera was approximately 30 m. Perspective corrections were made with GNU software GIMP's backward perspective transformation tool before the grain size analyses were performed (GIMP, 2009).

2.4.2 Survey of methods

To construct a grain-size distribution curve from a waste-rock image, the image was first divided into regions each containing a rock particle through a process called segmentation. There are three main categories of segmentation techniques (Fu and Mui, 1981): clustering, edge detection and region extraction. Clustering is a multidimensional version of thresholding, which is a simple and widely used technique. In thresholding, an upper and lower bound of a feature value such as intensity is chosen and pixels with intensities within that range are selected. Two or more features are used to perform a clustering segmentation (Wacker, 1969). The advantage of edge detection is that boundaries between objects in an image have more abrupt intensity changes. For example, in a rock image, pixels at the boundaries of rocks are darker than interior rock pixels. There is an array of techniques in this category: including watershed transformation methods, and partial-differential equation based methods e.g., the level-set method and the snake method (Osher and Fedkiw, 2002; Kass, et al., 1988). The idea of the region extraction method is to divide the image into regions of similar properties (Zucker, 1976). This can be accomplished by 1) region-growing: starting with small regions and merging similar regions, 2) region splitting: starting with large regions and splitting them 3) or a combination of both methods (Fu and Mui, 1981).

2.4.3 Region-growing segmentation

Region-growing was chosen as the segmentation technique here for its simplicity. The principal approach of region-growing is to take a set of arbitrary or user-chosen seed regions as input. The seed regions mark the objects to be segmented. These regions grow iteratively by including more neighboring pixels of similar properties until no more pixels can be included or the maximum iteration is reached (Figure 2 - 2). Intensity is the most commonly used property and was used in this study.

Two major challenges exist when segmenting waste-rock images with the region-growing method. First, unlike in the laboratory where the light source is controlled, natural lighting and the angular nature of rocks result in heavy shadows and “salt-and-pepper” noise in the photographs. Second, boundaries are often blurry which causes “leakage” or

overgrowth problems. Pre- and post-processing techniques were employed to overcome these challenges. Instead of using seed points, seed regions were used at the start of the program so that "salt-and-pepper" noises were averaged out when the mean of the region is calculated. In addition, regions were dilated after region-growing is performed to fill in the "holes" caused by imperfect rock surfaces and a Sobel mask is added to the original gray scale image to enhance the rock edges (Duda and Hart, 1973).

Image dilation is a morphological operator that enlarges region boundaries. Holes in the region can be filled or reduced in size. To perform dilation, two inputs are needed: the target image and a structure element (Gonzalez and Woods, 1992). The structure element specifies the extent of dilation. An example is shown in (Figure 2 - 3a). The original image is a binary image in which 1 is represented as white and 0 is black. In a dilation operation with a 3x3 structure element, for each black pixel, all its eight neighboring pixels are checked, and if at least one white pixel is detected, the respective black pixel is changed to a white pixel. The resulting white boundary of the region is enlarged or "dilated". More importantly, small holes in the region are filled by dilation (Figure 2 - 3b), which makes it a useful post-processing technique to fill the holes left by region-growing. The dilation operation causes a slight artificial enlarging of the grain size, but the introduced error is relatively small compared to the size of an image that is tens of thousands of pixels.

A Sobel mask is a 2D filter that enhances object boundaries in an image by calculating the derivatives of the image. A 3x3 Sobel mask is

$$\begin{bmatrix} -1 & 0 & 1 \\ -2 & 0 & 2 \\ -1 & 0 & 1 \end{bmatrix}$$

for horizontal edge enhancement and,

$$\begin{bmatrix} 1 & 2 & 1 \\ 0 & 0 & 0 \\ -1 & -2 & -1 \end{bmatrix}$$

for vertical edge enhancement. A filter is applied to an image by moving it across the image and calculating the product of the filter and the image. In the case of the Sobel mask, the product is the derivative of the image, which amplifies abrupt changes. The boundaries of a

rock are normally darker than the interior. The intensity difference is amplified by the Sobel mask and hence the boundaries are enhanced.

A white 1m x 1m PVC square is included in each photograph as a link between length in the image and a defined distance (Figure 2 - 4). Rock particle-size information is translated into sieve size by bounding the particle with a rectangle (Figure 2 - 5). Because rock particles orient themselves to pass the sieves, the shorter side length of the bounding square defines the sieve size of the particle. The final algorithm is shown in Figure 2 - 6.

2.4.4 Reproducibility and limitations

The image segmentation and hence grain-size curve results depend heavily on the selection of seed points/regions. Because the user defines this information, uncertainties are introduced into the results. It is difficult to quantify the overall uncertainty because each image is different and each user is different. As a demonstration, five users were asked to run the algorithm two times each on the same image and results are presented in Figure 2 - 7. The fluctuation of grain size distribution is approximately within 10% of the mean grain-size distribution.

There were two additional limitations in the use of this algorithm. 1) The size reference, the white 1m x 1m PVC square, was considered of constant size throughout the image. However, because the perspective transformation was not perfect, the reference size may vary at different locations of the pile. But the influence of this difference on the final grain-size results was modest compared to the variation in grain diameters, which vary by orders of magnitude. 2) The minimum grain size detectable in an image using this method was about 5 pixels. Depending on the image, this minimum size may correspond to grain sizes of 0.01 m to 0.2 m. To overcome this limitation, for the grain size fraction of less than 0.1 m, mean grain-size distribution from sieve analysis on hand samples was attached to all image grain size analysis results to obtain full grain-size distributions. Because the grain-size curves obtained from sieve analysis fall closely together (within +/- 2 standard deviation), mean grain-size distribution from the entire pile was used to represent the less than 0.1 m fractions for each tip face.

2.5 Results and discussions

2.5.1 Image-analysis results and observations

Each photo was divided into a grid of squares, three vertical by six horizontal, and the segmentation algorithm was applied to each square to obtain a grain size curve for each square (Figure 2 – 8). Grains that cross boundaries of multiple squares were considered as smaller grains in each square. Considering each square contains tens to hundreds of grains, the errors induced by cutting several large grains at boundaries into smaller grains are not very significant when overall grain-size distribution is examined. Squares are labeled using the convention "(row, column)", with (1,1) representing the upper left corner of the photograph. The elevation of each square is referred to as "top", "middle" and "bottom" instead using physical scales because the physical coordinates were unevenly skewed by the imperfect perspective transform. The photograph and the grain-size distribution for TIN are presented in Figure 2 - 9a and b. The photographs and grain-size distribution for the remaining faces are included in Appendix A. Curves representing squares of the same vertical displacement are presented using the same color, and curves representing squares of the same horizontal displacement are presented using the same marker symbol. All 18 curves of a face form an "envelope" that defines overall grain-size property of the face.

Grain-size distributions for the six exposed faces of the TI and TIII piles (Figure 2 – 10) show a wide range of grain size distribution. The proportion of fines, defined as grains with diameters < 0.01 m, ranges from ~10% to over approximately 40%. In general, the upper portions of the faces, represented by red curves in each plot, have significantly more fine grains than the lower portions of the faces. This is likely the result of compaction from the heavy vehicle traffic on the top of the pile. The blue and green curves lie more closely together, indicating the middle and the lower portion of the faces are more similar in grain size. The steepness of a grain-size-curve envelope reflects the homogeneity of the grain-size distribution of the individual face. The narrower the envelope of grain-size curves, the more homogeneous the grain size distribution is across a tip face. The TIIIW, TIN and TIW faces have the narrowest grain-size distributions, suggesting that segregation of these faces is less extensive than on other faces. The TIIIN face has the broadest distribution suggesting that

segregation was extensive on this face. It should be noted that TIIIW and TIN are dump faces, i.e., the faces from which waste rock was dumped. Direct push by dozers during the construction may have resulted in less extensive particle segregation and a more uniform grain-size distribution.

The large-scale grain-size measurements obtained of TI and TIII materials are compared to the image grain-size analysis results (Figure 2 - 11). The measured grain-size distribution falls within the envelope of each face determined by image analysis, suggesting there is reasonable consistency between the measurement techniques. Furthermore, because each of the large grain-size analysis is a single truckload with no segregation, the distribution of each grain-size envelope determined by image analysis around the measured truckload grain size is consistent with the hypothesis that tip faces represent segregated truckloads.

Assuming grains are ideal spheres, surface area and mass distribution among different grain-size fractions were calculated based on 1 kg of sample (Figure 2 - 12). The results indicate that although the greatest mass on the faces is associated with the coarse grains, the greatest surface area is associated with the fine-grain fraction (< 0.01 m). To obtain method of moment statistics, grain-size distributions were converted to logarithmic Udden–Wentworth grade scale using $\phi = -\log_2 d$ where ϕ is converted Udden–Wentworth grade scale value and d is grain diameter in millimeters (Udden, 1914; Wentworth, 1922). Statistical moments for each grain-size curve were calculated using logarithmic method of moments (Krumbein and Pettijohn, 1938). The results are listed in Table 2 - 1 and summarized in Figure 2 - 13. The four moments (equations included in Appendix C) are: 1) mean grain size, 2) standard deviation (sorting) of grain size, 3) skewness, the degree of preferential spread to one side of the mean and 4) kurtosis, the degree of concentration around the mean. A brief description of how values of the moments correspond to physical interpretations is included in the table caption. Both the TI and TIII piles have mean grain size of granules and are very poorly sorted, coarse skewed and leptokurtic (which means the distribution is more concentrated around the mean grain size than spread-out among all grain sizes).

In addition to grain-size distribution curves, d-n values, the diameter of grain that n% of the material is finer than, are determined on the 3 x 6 grid for each face to visualize the spatial grain-size variations. Trial-and-error showed that d50 contours provide the most detailed information regarding pile heterogeneity (Figure 2 - 14). All photos are included in Appendix A for reference and comparison with d50 contours. Visual inspection shows that the method provides reasonable accuracy and detail in representing pile heterogeneities (Figure 2 - 9a and c and Figures A1 to 5). The d50 ranges from approximately 0.01 m to 0.4 m. The finer grains are mainly retained at the top of the test piles. Vertically, grain size increases from top to bottom of the piles, demonstrating the effects of gravity sorting, and raveling of large boulders on the tip face. The average d50 value at each vertical displacement is plotted and a similar pattern is observed as for the grain-size curves (Figure 2 - 15a). The slopes are gentler from middle to bottom of the test piles than from top to middle of the test piles indicating a more distinct grain-size variation within the upper half of the test piles. TIIIN shows an anomaly with a vertically symmetric d50 distribution pattern with the highest d50 value in the middle and decreasing towards both higher and lower height. TIIIW also shows a high d50 value in the middle of the face. This pattern may reflect placement of a single load, dominated by large boulders at this location. Although not as significant as in the vertical direction, d50 varies horizontally; however, there is no clear relationship between horizontal displacement and d50 values (Figure 2 - 15b). Horizontally, the relative magnitude of d50 values is consistent at different vertical displacements. For example, in Figure 2 - 16, at the top of TIN, Location 1 and 3 have smaller d50 values than Location 2, and at the same horizontal displacement but the bottom of the face, Location 1’ and 3’ have smaller d50 than Location 2’. These bands of coarse and fine grain sizes (dashed lines in Figure 2 - 13) are likely the result of truck dumping and dozer pushing during the construction. For instance, if an individual truckload of waste rock is finer than another one, a vertical band of finer-grained material may result.

2.5.2 Implications

This analysis demonstrates that the fine fraction of the waste rock is preferentially retained at the top of the exposed tip face of the test piles and as a consequence, grain size

varies non-linearly along a pile face with the upper half finer than the lower half. Since the internal tip faces were constructed using the same truck-dumping and dozer-pushing methods, the interior of the pile is expected to of similar heterogeneity. The proportion of fine-grained material determines surface area and permeability of a waste rock pile and hence affects fundamental acid-generating processes including reaction rate, water flow and gas flow. This analysis is limited to tip faces and cannot account for filling of open voids by deposition of subsequent loads of waste rock over the tip face.

2.5.2.1 Permeability

Permeability is an intrinsic property directly affected by grain-size distribution that has a strong influence on the physiochemical processes in the waste rock piles. Permeability was calculated using both Hazen (1911) and Kozeny–Carmen (Kozeny, 1927; Carmen 1938; Carmen 1956) formulae and compared to field measurements obtained using air permeability balls (Amos et al., 2009a and b). Despite formulae were developed for finer sandy materials, reasonable agreement between predicted values and field measurements is obtained (Table 2 - 2). The d10 of individual squares within each analyzed face of the test-piles ranges between 0.0001 m to 0.01 m, which corresponds to a permeability of 10^{-11} m^2 to 10^{-7} m^2 using the Hazen formula and 10^{-12} m^2 to 10^{-8} m^2 using the Kozeny-Carmen formula. The range of average calculated permeabilities for each row of the analyzed faces is 10^{-10} m^2 to 10^{-8} m^2 using Hazen formula and 10^{-11} m^2 to 10^{-9} m^2 using Kozeny-Carmen formula. This is consistent with the range of measured permeabilities, which range 10^{-10} to 10^{-9} m^2, but are limited to six points in each test pile. Permeability contours are constructed using Kozeny-Carmen formula (Figure 2 -17). The contours show that permeability is lowest in the top layers of the test piles and highest in the middle layers of the piles. Neuner (2008) conducted permeameter tests on a 16 m^3 waste rock sample from the Diavik site. The reported saturated hydraulic conductivity was 10^{-2} m/s, which corresponds to a permeability of 10^{-9} m^2. However, the results may have been limited by the screen pipe at the drain of the permeameter. Neuner (2008) concluded that the permeability is at least 10^{-9} m^2. The calculated permeability values in this study were up to 10^{-7} m^2. This is consistent with the measurements by Neuner (2008).

2.5.2.2 Reaction rate

Fine grains correspond to higher surface area and hence greater potential for oxidation. Reaction rates are generally assumed to be proportional to the surface area of minerals exposed at the particle surface. Using batch reactors Stromberg and Banwart (1999) demonstrated that there is a difference in sulfur-mineral reaction rates between fine and coarse grains, with the fine-grained fraction reacting more quickly than the coarse-grained fraction. Smith (2009) analyzed samples of the < 50 mm fraction of the Diavik TI and TIII test pile material and determined that the fine-grained fraction contains a higher concentration of sulfur, suggesting that the greatest potential reactivity is associated with the fine-grained fraction. Calculations based on assuming a unit mass at the face of the TI and TIII piles indicate that although the greatest mass on the face is associated with the large particles, the greatest proportion of surface area is associated with the fine fraction (Figure 2 - 12). This suggests the top of the tip face has the highest reactivity and is of greatest concern.

In addition to affecting the rate of sulfide oxidation, the grain-size distribution controls the waste-rock porosity and permeability and hence affects the oxygen-diffusion rate and the hydraulic conductivity of a waste-rock pile. The availability of oxygen may limit sulfide mineral oxidation. Molson et al. (2005) demonstrated that there is a trade-off between grain size and oxidation rate because finer grains have lower permeability and slower oxygen diffusion, but the high surface area provided by finer grains increases the oxidation rate. Gas concentration measurements consistently indicate that the TIII test pile has atmospheric levels of O_2 and CO_2 througout the pile over time, suggesting that oxygen availability does not limit oxidation reactions (Amos et al., 2009b). Hence, reactions should become less extensive from top to bottom of the test piles. This inference is consistent with early-time analysis of pore water samples collected from soil water solution samplers (SWSS) located at various depths within the TIII test pile, which show concentrations of sulfate and ferrous iron decrease from the top to the bottom of the pile (Bailey et al., in progress).

2.5.2.3 Water flow

The grain size curve envelopes obtained from the analysis can be used to represent grain-size distribution on the scale of a representative elemental volume (REV) of the waste rock piles, which was previously represented by only one large-scale grain size measurement. Fine grains retained at the top of the piles will result in lower hydraulic conductivity in this region. At the field facility, samples taken from the top of the TIII pile after the construction was completed have mean saturated hydraulic conductivity of 3.3×10^{-6} m/s compared to 1.7×10^{-5} m/s for samples representing the interior of the pile (Neuner et al., 2009). Although the measurements are made at a smaller scale than those presented here, these measurements provide a consistent indication that the rock in the upper portion of the test pile is more fine-grained than the lower zones. Previous modeling by Neuner et al. (2009) demonstrats that a homogeneous domain does not adequately describe the hydrogeological field data. The heterogeneity information obtained from the analysis can provide a basis for future modeling efforts.

2.5.2.4 Gas flow

Thermal convection and diffusion are often considered the most important mechanisms for gas flow in waste-rock piles (Ritchie, 1994; Bennett et al., 1995; Lefebvre et al., 2001a; 2001b). It has been recently demonstrated by Amos et al. (2009a and b) and Chi, et al. (Chapter 3) that wind-driven advection is an important factor contributing to gas transport in the Diavik test-scale waste-rock piles. Previous modeling assuming a homogeneous permeability structure showed that the most significant response to wind flow over a waste-rock pile is focused at the upper edges of the rock pile (Anne and Pantelis, 1997 and Ritchie and Miskilly, 2000). The accumulation of fine-grained material at the upper region of the pile observed from the analysis presented here can be expected to 1) limit gas flow by lowering permeability and 2) promote oxygen consumption through oxidation reactions enhanced by the higher surface area of the rock in this zone. However, due to the relatively low oxidation rate of the Diavik test piles, and the relatively high permeability, oxygen depletion is not observed despite the finer grained materials. Amos et al. (2009a) measured gas-pressure data for the Type III test pile and were unable to obtain reasonable

agreement between gas-pressure data and simulation results using a homogeneous pile configuration. Amos et al. (2009a) concluded that the discrepancy probably was due to a combination of heterogeneity within the test pile and irregular landscape surrounding the test pile. The heterogeneity information provided by this study can be useful in modeling gas transport.

2.6 Conclusions

A digital image analysis method was developed to analyze large-scale grain-size distributions. The image analysis method combined with traditional sieve analysis was applied to photos taken of experimental waste-rock piles in the Canadian arctic. The results were able to quantify the wide range of grain-size variations observed in the piles and provided an analysis of the spatial heterogeneity of the piles. Important observations included: 1) fine-grained material is preferentially retained at the top of the test piles, 2) grain size decreases non-linearly from top to bottom of the test piles and also varies horizontally but with an inconsistent trend, 3) The greatest surface area is associated with fine fractions, 4) The Diavik test-scale waste-rock piles have mean grain size of granules and are very poorly sorted, coarse skewed and leptokurtic. 5) Permeability can be reasonably estimated by empirical formulae based on d10 values obtained from combined image analysis and sieve analysis grain-size distributions. The observations are consistent with permeability measurements, measured large-scale grain-size analysis performed in the field, pore-water chemistry demonstrating higher reactivity in the finer material at the top of the test piles, and hydraulic conductivity measurements showing lower hydraulic conductivity at the top of the piles compared to within the piles. The d50 contours provide a visual demonstration of the heterogeneity of the test piles and show distinct trends in grain size with depth and horizontally across tip faces. The interior of the test piles are expected to have similar property because the internal tip faces were constructed using the same methods.

The method provides a means to quantify grain-size distributions for waste-rock piles, which is difficult and expensive to accomplish by traditional sieve analysis. It also provides a two-dimensional visualization of the heterogeneity of waste-rock piles. This information can provide a basis for implementing fluid-flow and gas-transport models in the future.

2.7 Tables

Face	H	V	Mean	Standard	Skewness	Kurtosis	Face	H	V	Mean	Standard	Skewness	Kurtosis
TIE	1	1	-4.5	3.5	0.5	2.3	TIIIN	1	1	-7.2	2.8	1.9	6.1
	1	2	-5.5	3.5	0.8	2.7		1	2	-5.8	3.4	1.0	3.0
	1	3	-5.0	3.5	0.7	2.5		1	3	-6.1	3.6	1.0	2.9
	1	4	-6.1	3.5	1.1	3.1		1	4	-5.0	3.6	0.6	2.4
	1	5	-4.7	3.6	0.5	2.3		1	5	-4.1	3.5	0.3	2.3
	1	6	-4.2	3.4	0.5	2.4		1	6	-5.5	3.7	0.7	2.5
	2	1	-6.5	3.2	1.4	4.1		2	1	-7.9	2.2	2.7	11.0
	2	2	-6.3	3.2	1.3	3.8		2	2	-7.2	2.8	1.9	6.0
	2	3	-6.1	3.5	1.1	3.1		2	3	-6.1	3.0	0.7	3.5
	2	4	-6.6	3.3	1.4	4.0		2	4	-7.4	2.9	1.9	5.9
	2	5	-7.0	3.0	1.7	5.1		2	5	-7.3	2.8	1.9	6.1
	2	6	-6.9	3.1	1.5	4.5		2	6	-5.7	3.3	0.5	2.7
	3	1	-6.1	3.6	1.0	2.9		3	1	-7.1	3.1	1.6	4.8
	3	2	-6.4	3.4	1.2	3.4		3	2	-5.1	3.7	0.6	2.2
	3	3	-6.2	3.6	1.0	2.9		3	3	-6.5	3.3	1.3	3.8
	3	4	-6.6	3.4	1.3	3.5		3	4	-6.5	3.3	1.3	3.7
	3	5	-6.8	3.3	1.4	4.0		3	5	-6.0	3.6	1.0	2.8
	3	6	-6.8	3.4	1.4	3.8		3	6	-4.6	3.7	0.4	2.1
TIW	1	1	-6.1	3.4	1.1	3.3	TIIS	1	1	-4.6	3.7	0.3	2.1
	1	2	-7.0	2.9	1.7	5.4		1	2	-4.3	3.6	0.2	2.1
	1	3	-5.0	3.6	0.6	2.4		1	3	-5.9	3.6	0.9	2.7
	1	4	-7.2	2.7	1.9	6.4		1	4	-5.4	3.8	0.7	2.3
	1	5	-7.1	3.1	1.7	5.0		1	5	-3.8	3.5	0.2	2.3
	1	6	-5.2	3.6	0.6	2.4		1	6	-5.2	3.7	0.6	2.2
	2	1	-6.9	2.4	1.3	6.0		2	1	-5.4	3.6	0.7	2.5
	2	2	-7.7	2.3	2.6	10.3		2	2	-6.0	3.4	0.9	3.0
	2	3	-7.7	2.5	2.4	8.5		2	3	-6.4	3.5	1.2	3.3
	2	4	-7.7	2.4	2.5	9.6		2	4	-6.1	3.5	1.0	2.9
	2	5	-7.7	2.5	2.4	8.9		2	5	-6.5	3.4	1.2	3.4
	2	6	-8.0	2.2	2.9	11.8		2	6	-6.2	3.6	1.0	3.0
	3	1	-6.9	3.2	1.5	4.4		3	1	-4.7	3.5	0.0	2.2
	3	2	-7.6	2.8	2.1	6.9		3	2	-4.7	3.5	-0.1	2.1
	3	3	-6.7	3.4	1.3	3.5		3	3	-5.5	3.4	0.3	2.4
	3	4	-7.3	2.9	1.9	5.7		3	4	-6.0	3.3	0.8	3.0
	3	5	-3.7	3.4	-1.1	2.4		3	5	-6.2	3.5	1.1	3.1
	3	6	-7.6	2.8	2.1	6.7		3	6	-7.2	3.1	1.8	5.3
T1N	1	1	-7.0	3.2	1.6	4.6	TIIIW	1	1	-5.9	3.4	1.0	3.0
	1	2	-6.9	3.2	1.5	4.4		1	2	-6.5	3.3	1.3	3.8
	1	3	-5.7	3.6	0.9	2.7		1	3	-6.5	3.2	1.3	4.0
	1	4	-6.9	3.2	1.5	4.4		1	4	-6.7	3.1	1.5	4.5
	1	5	-5.7	3.5	0.9	2.8		1	5	-4.3	3.4	0.5	2.4
	1	6	-6.3	3.5	1.2	3.3		1	6	-4.2	3.6	0.3	2.2
	2	1	-7.8	2.3	2.6	10.4		2	1	-7.4	2.6	2.1	7.2
	2	2	-7.4	1.9	1.4	8.5		2	2	-7.3	2.8	2.0	6.5
	2	3	-7.9	2.2	2.8	11.2		2	3	-7.7	2.5	2.4	8.8
	2	4	-7.7	2.5	2.4	9.0		2	4	-7.4	2.7	2.0	6.8
	2	5	-7.3	2.8	1.9	6.3		2	5	-7.4	2.5	2.2	7.9
	2	6	-7.6	2.6	2.3	8.0		2	6	-7.3	2.7	2.0	6.7
	3	1	-7.0	3.0	1.7	5.1		3	1	-7.5	2.7	2.1	7.1
	3	2	-8.1	2.1	3.1	13.1		3	2	-7.0	2.8	1.8	5.7
	3	3	-8.2	2.1	3.2	13.9		3	3	-6.9	3.1	1.6	4.7
	3	4	-8.0	2.4	2.8	10.7		3	4	-6.7	3.2	1.4	4.1
	3	5	-8.0	2.2	2.9	11.8		3	5	-6.8	3.3	1.5	4.1
	3	6	-7.9	2.5	2.7	9.7		3	6	-7.5	2.7	2.1	7.2
	3	5	-8	2.23	2.91	11.8		3	5	-	3.26	1.45	4.13
	3	6	-7.92	2.47	2.65	9.6		3	6	-	2.7	2.14	7.17

Table 2 - 1: Moments calculations. *H: horizontal coordinate and V: vertical coordinate. According to Udden-Wentworth scale, cobbles = -11 to -6 phi, pebbles = -6 to -2 phi, granules = -2 to -1 phi, sand = -1 to 4 phi, silt = 4 to 8 phi and clay = 8 to 9 phi (Udden, 1914 and Wentworth, 1922). Standard deviation/sorting: < 0.7 = well sorted, 0.7 to 1 = moderately

sorted and >1 = poorly sorted. Skewness: >0.43 = fine skewed, -0.43 to 0.43 = symmetrical and <-0.43 = coarse skewed. Kurtosis: <2.55 = platykuritic, 2.55 to 3.7 = mesokurtic and >3.7 = leptokurtic (Krumbein and Pettijohn, 1938).

Pile	Row	Mean d10 (m)	Kozeny-Carmen† (m^2)	Hazen* (m^2)	Measured (m^2)		
					Min	Max	Mean
TI	Top	4.57E-4	3.48E-11	2.09E-10	5.0E-10	3.0E-9	1.84E-09
	Middle	5.26E-3	4.62E-09	2.77E-08			
	Bottom	2.59E-3	1.12E-09	6.71E-09			
	Average		1.92E-09	1.15E-08			
TIII	Top	3.52E-4	2.07E-11	1.24E-10	2.0E-10	4.0E-9	1.85E-09
	Middle	1.60E-3	4.27E-10	2.56E-09			
	Bottom	6.12E-4	6.26E-11	3.75E-10			
	Average		1.70E-10	1.02E-09			

Table 2 - 2: Mean calculated permeability for each row of the Type I and Type III test piles compared to mean measured permeability.

†Kozeny-Carmen: $k = C_k f_k(n) d_{10}^2$ where $C_k = 8.3 \times 10^{-3}$, $f_k(n) = \frac{n^3}{(1-n)^2}$, n =porosity=0.23 (Neuner, 2009), d_{10} = 10% passing

*Hazen: $k = Cd_{10}^2$ where k = permeability, C = Hazen empirical coefficient, usually assumed to be 100, d_{10} =10% passing

2.8 Figures

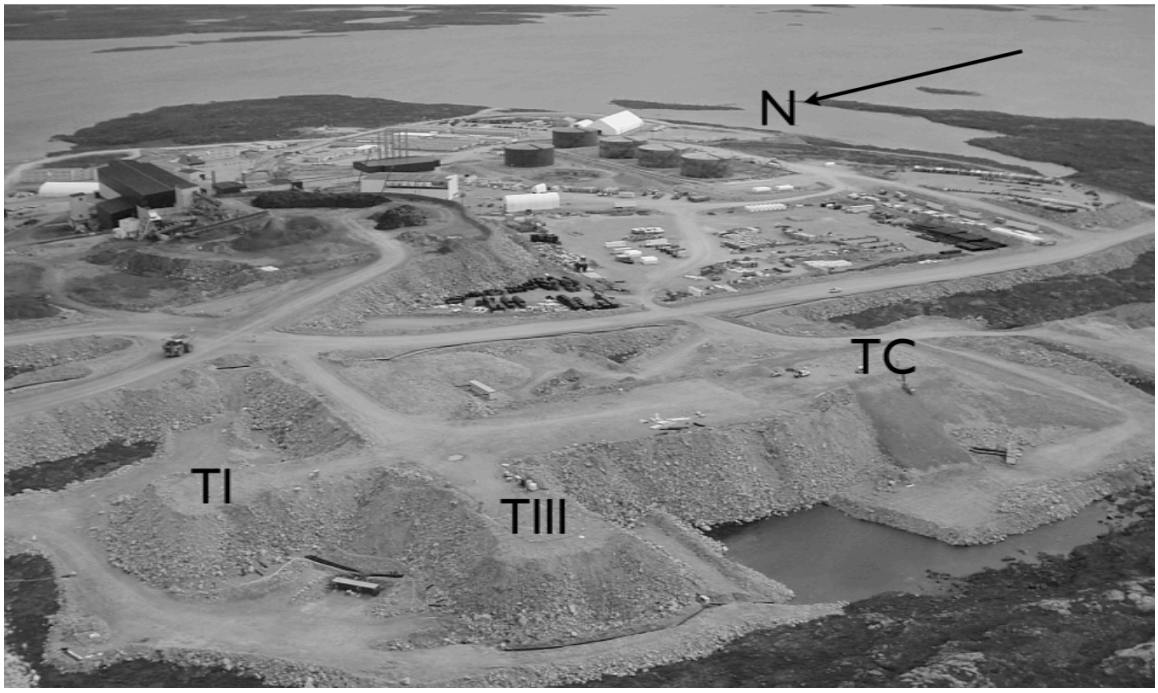

Figure 2 - 1: Aerial photo of the Diavik test-pile waste rock research area.

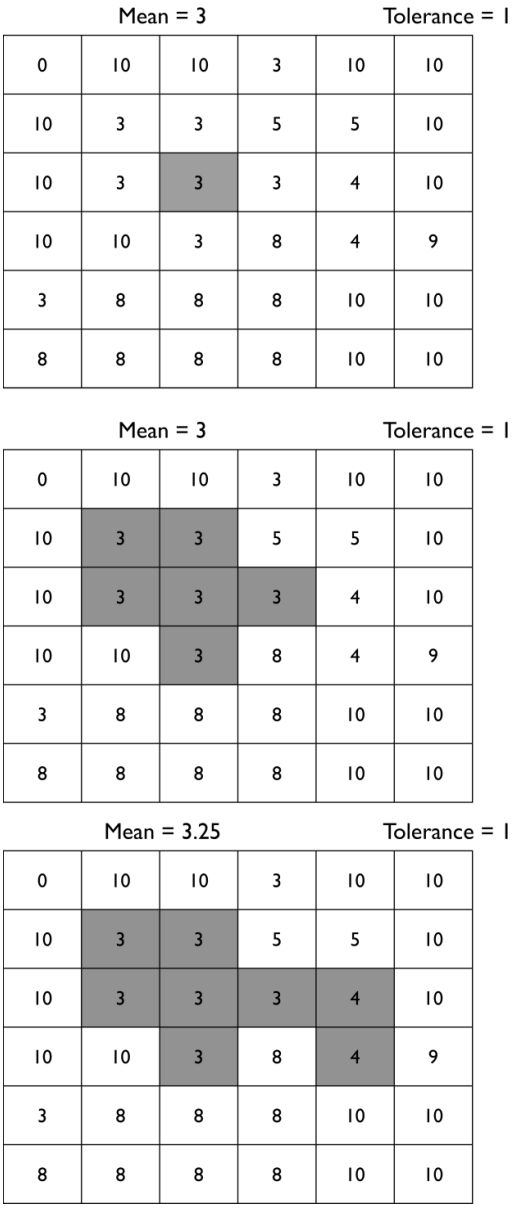

Figure 2 - 2: Illustration of a region-growing algorithm. (a) The algorithm starts with a seed point, (b) The seed point's 8 neighboring pixels are checked. If the difference between mean of the seed region and neighboring pixels is smaller than the tolerance, the neighboring pixel is added to the set, (c) The seed region keeps growing until no more pixels can be included. The mean of the region is updated after each iteration.

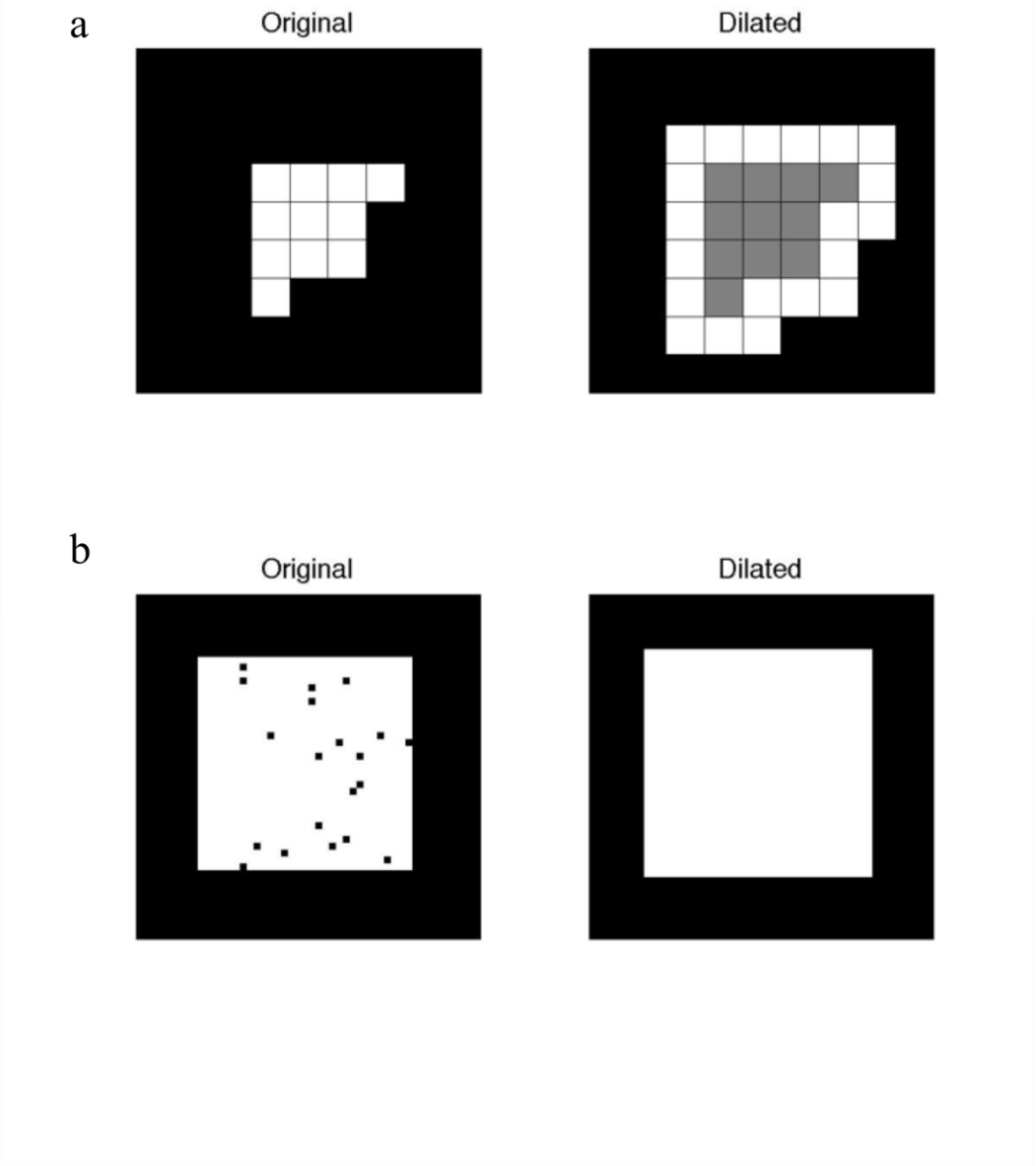

Figure 2 - 3: Image dilation. (a) A region is dilated by 1 pixel. The gray pixels in the right figure show the original pre-dilated region for comparison. (b) Image dilation fills the holes in the image.

Figure 2 - 4: A typical face of the piles with 1m x 1m PVC reference square.

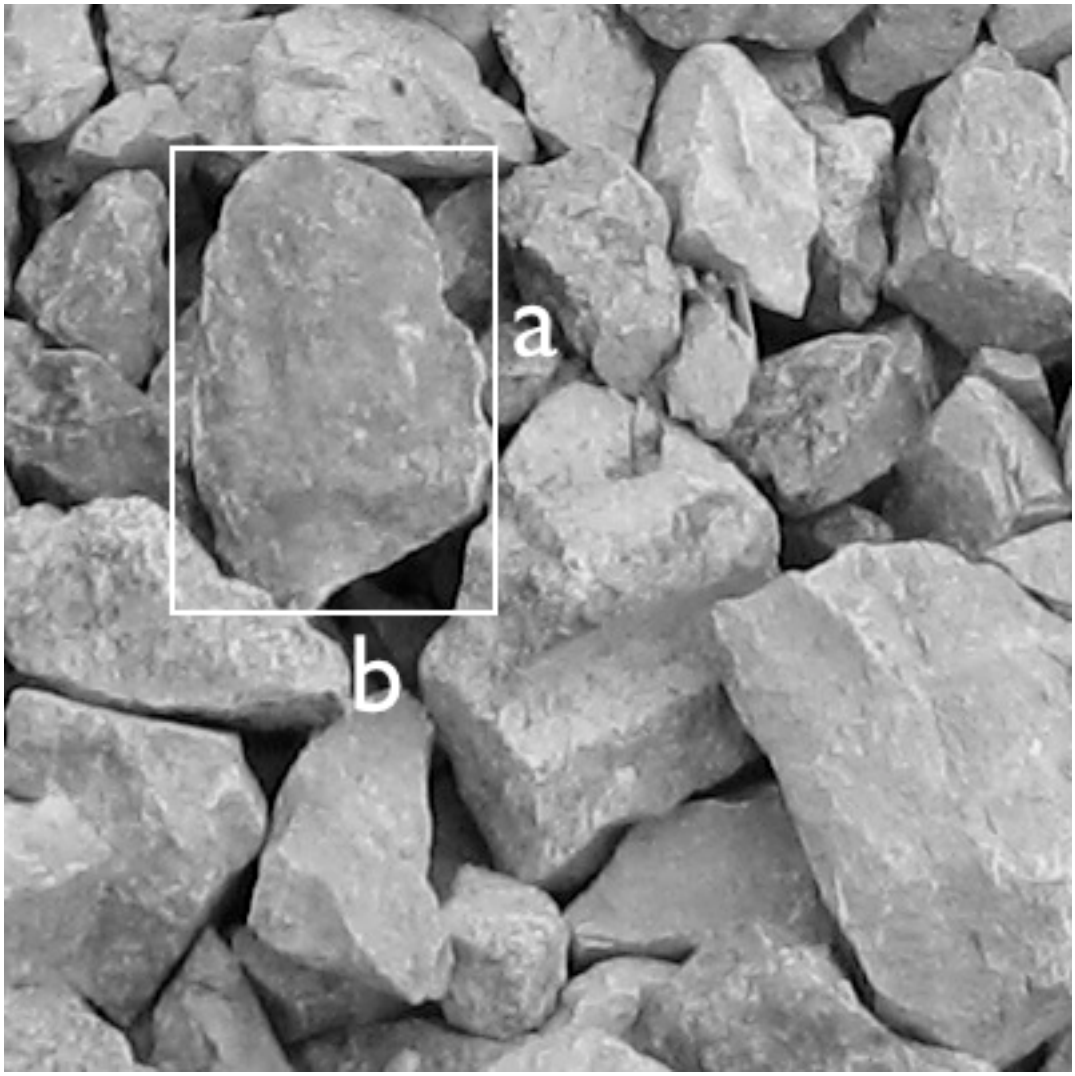

Figure 2 - 5: The rock-bounding square. The minimum value of a and b is used as the passing sieve size.

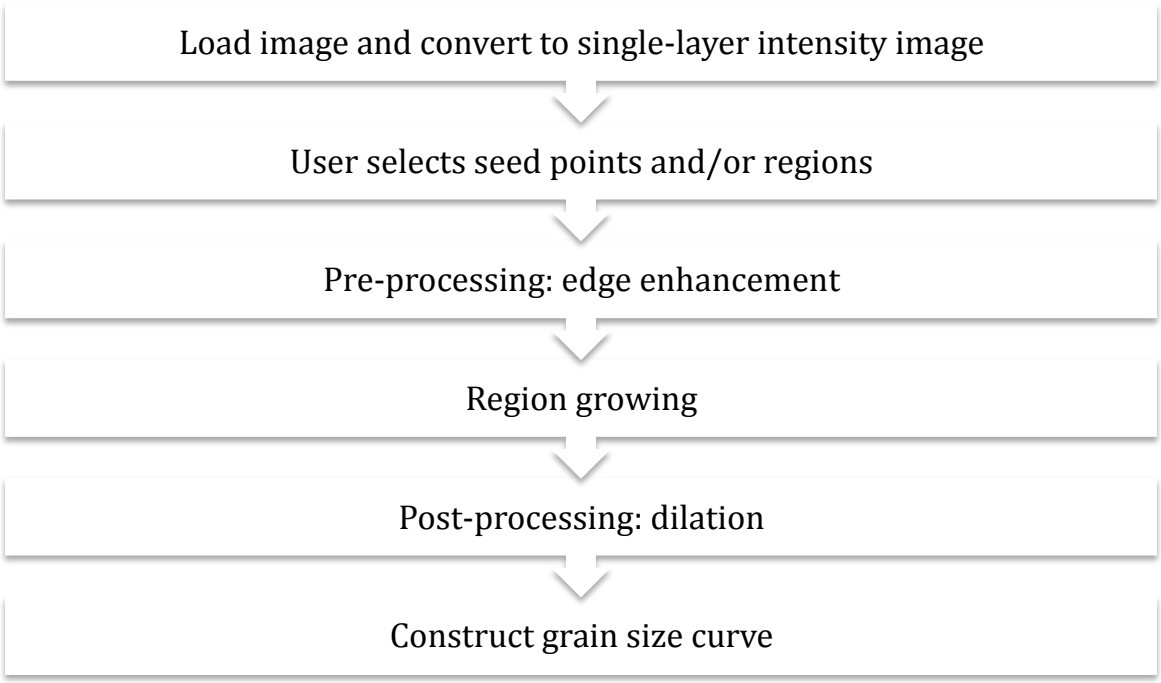

Figure 2 - 6: The region-growing algorithm flowchart.

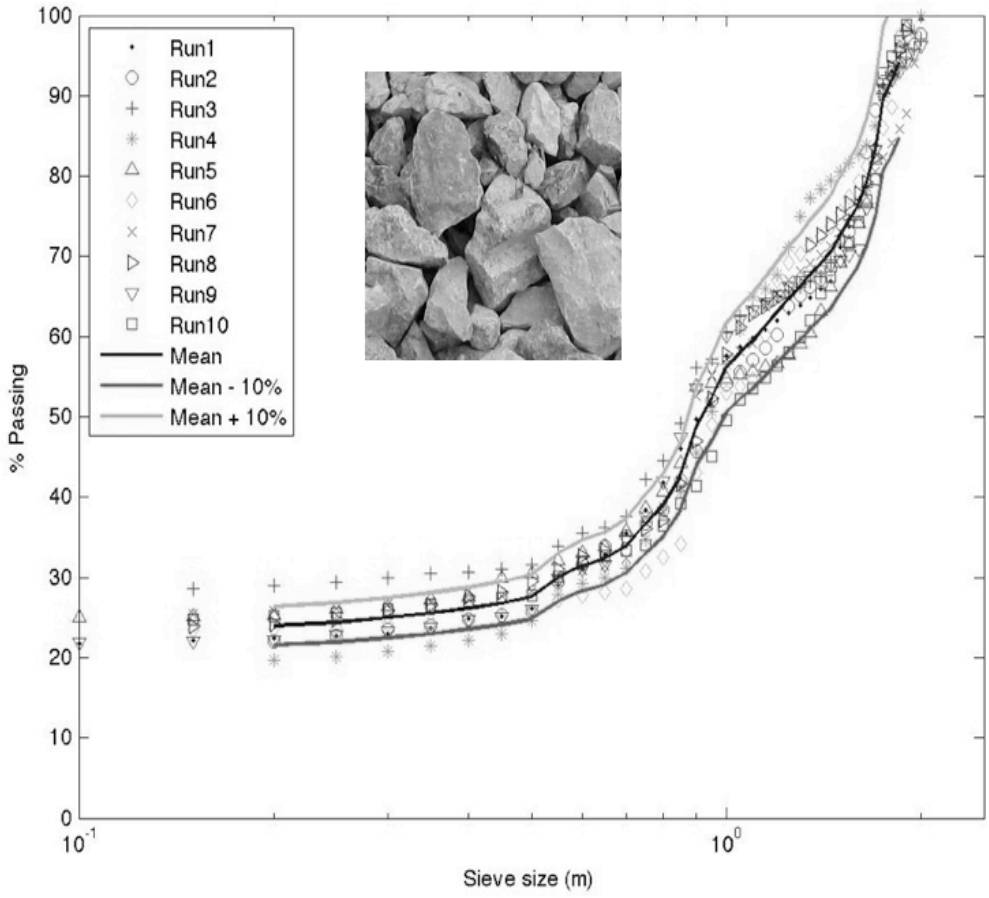

Figure 2 - 7: Grain size curves demonstrating the reproducibility of the algorithm. The algorithm was applied to the inset photograph ten times by five different users.

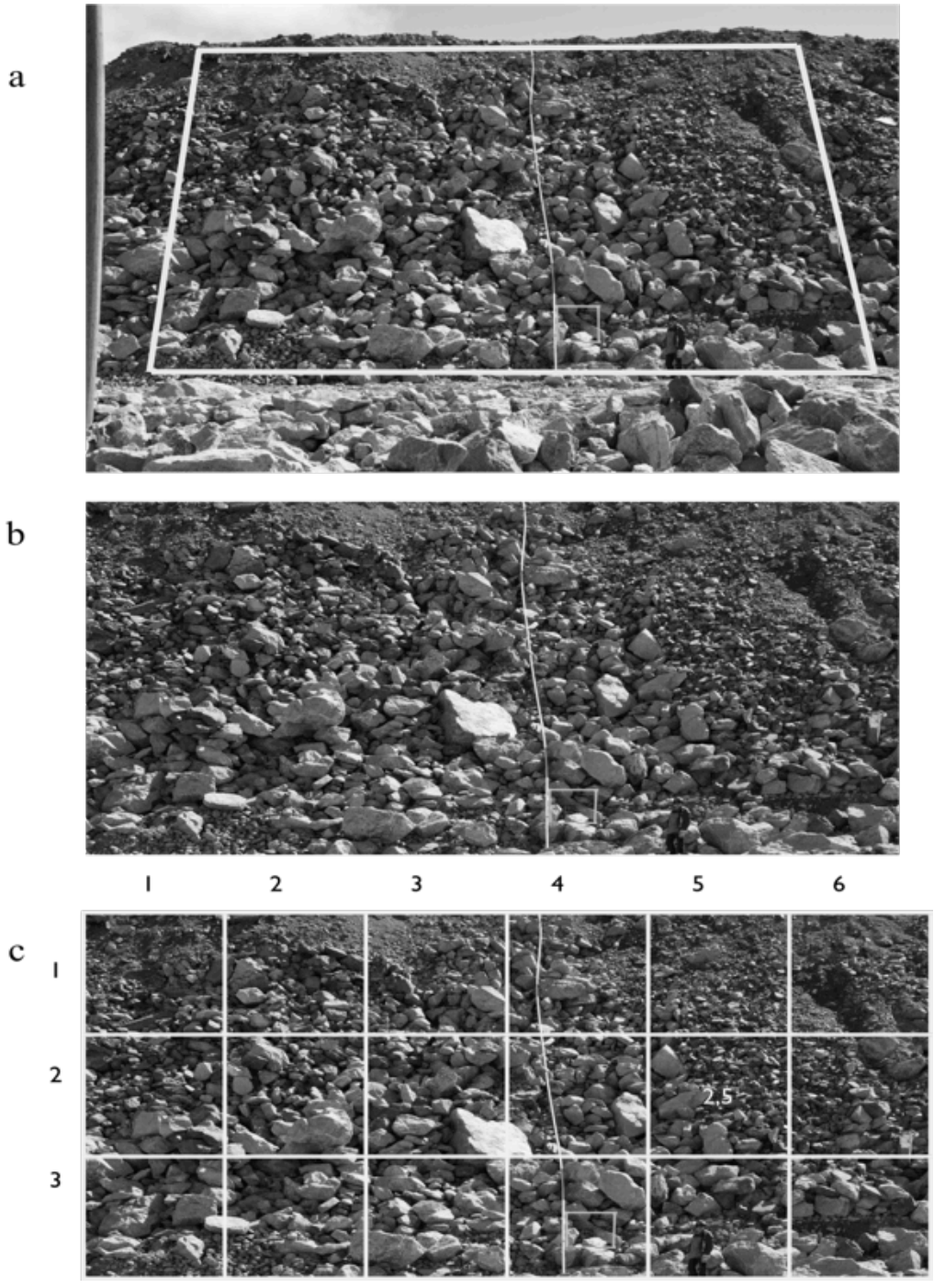

Figure 2 - 8: (a) A test pile face image with a trapezoid marking the region for image analysis (b) The region after perspective transformation (c) The region divided into 3 x 6 sub-regions.

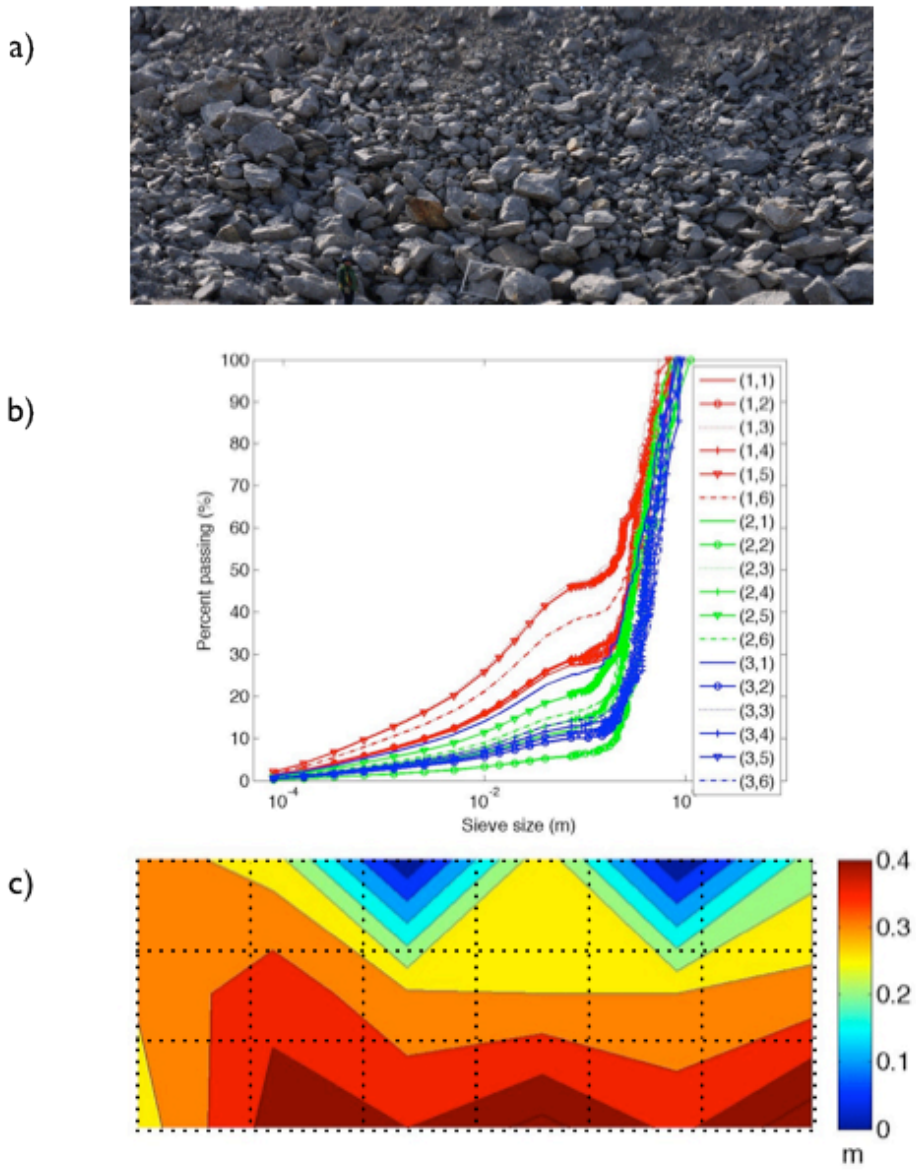

Figure 2 - 9: a) Photo of face TIN b) grain size distribution of TIN obtained from image grain size analysis with sieve analysis results attached for grain size <0.1 m c) d50 contour of TIN. The d50s are interpolated on the center of each square defined in Figure 2 – 8 (dashed lines) to obtain the contours.

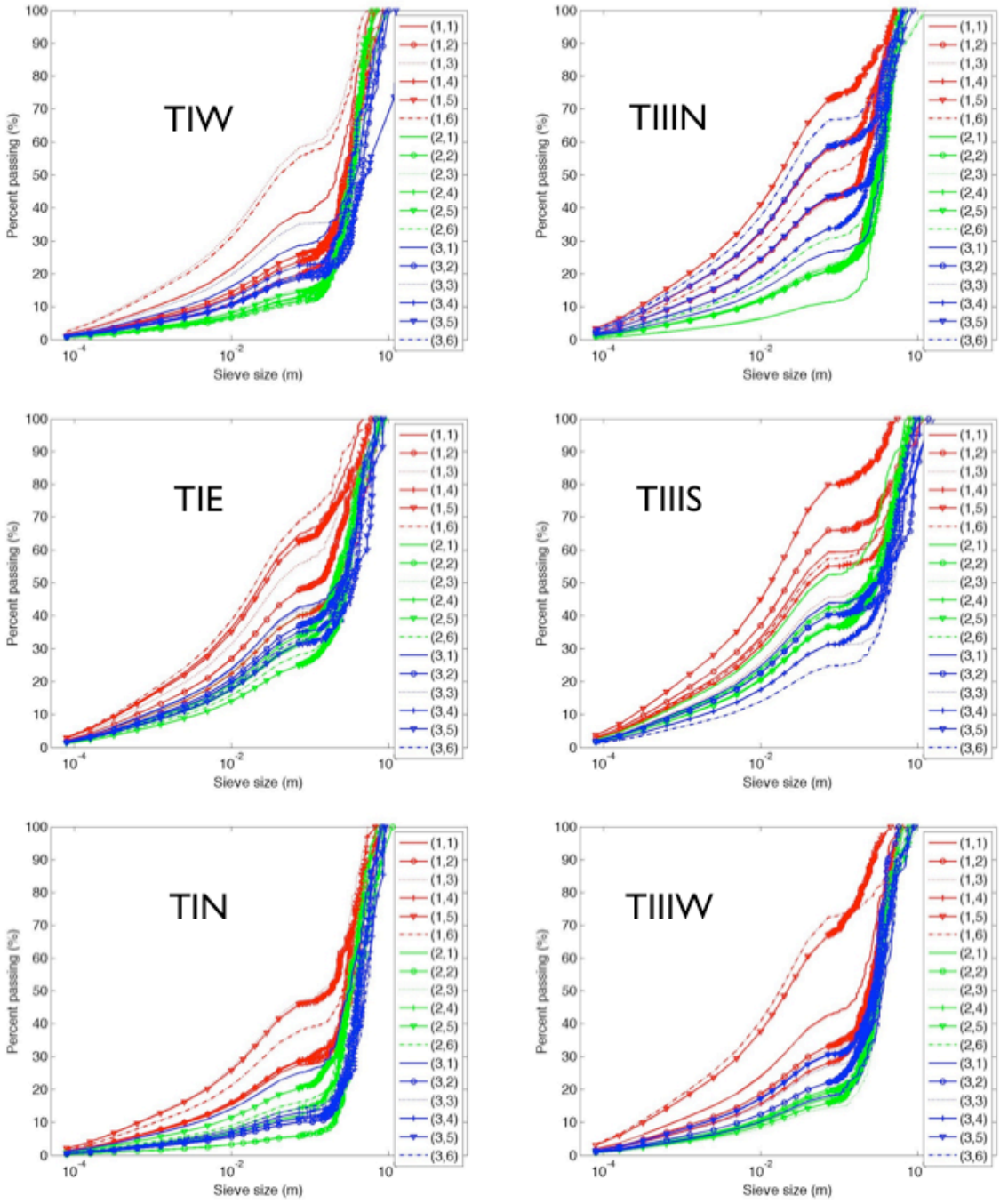

Figure 2 - 10: Grain size curves for the six exposed faces of the TI and TIII test piles. The curves are labeled using the coordinates of the respective squares as defined in Figure 2 – 8.

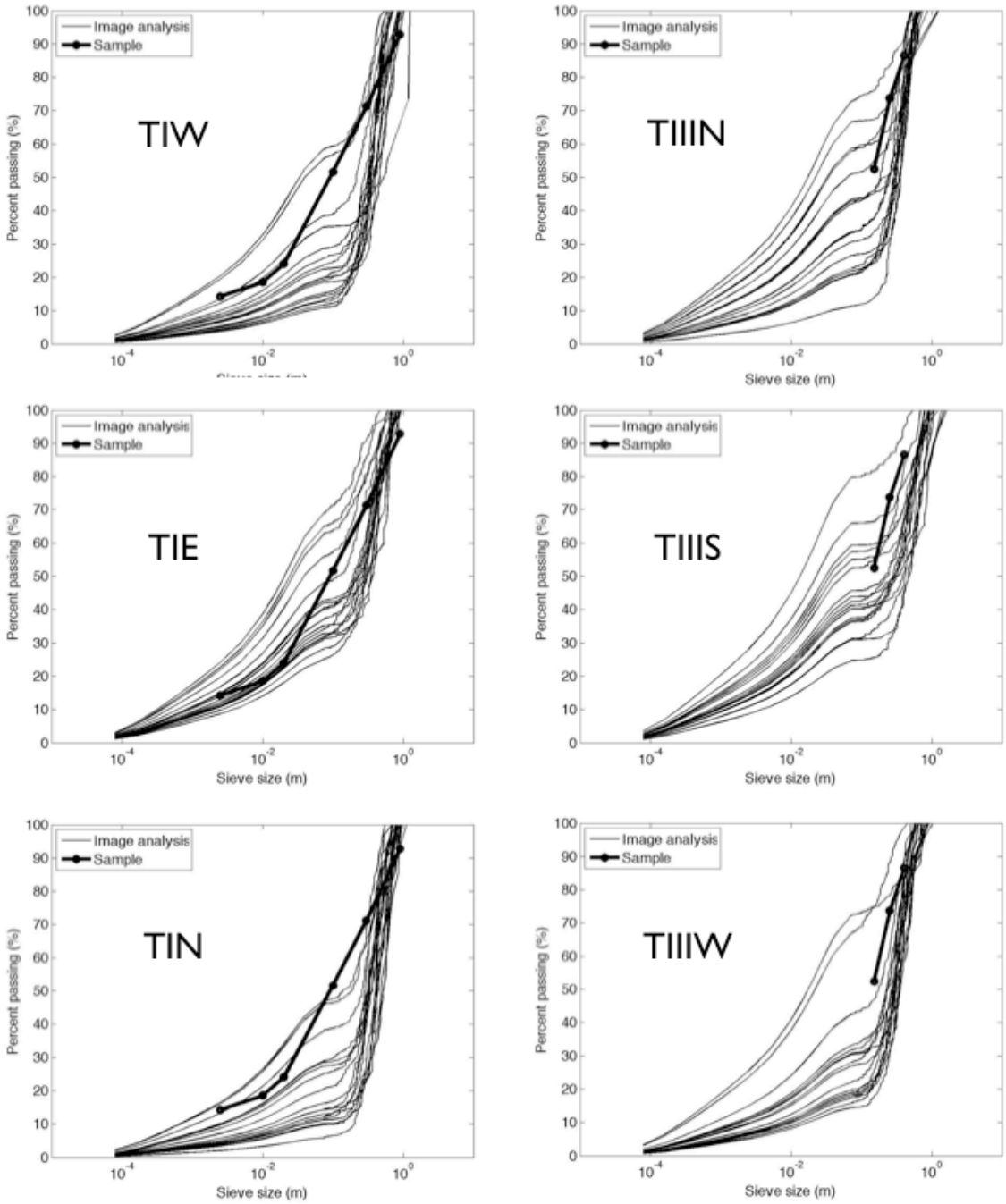

Figure 2 - 11: Field sample of grain size compared with image analysis results.

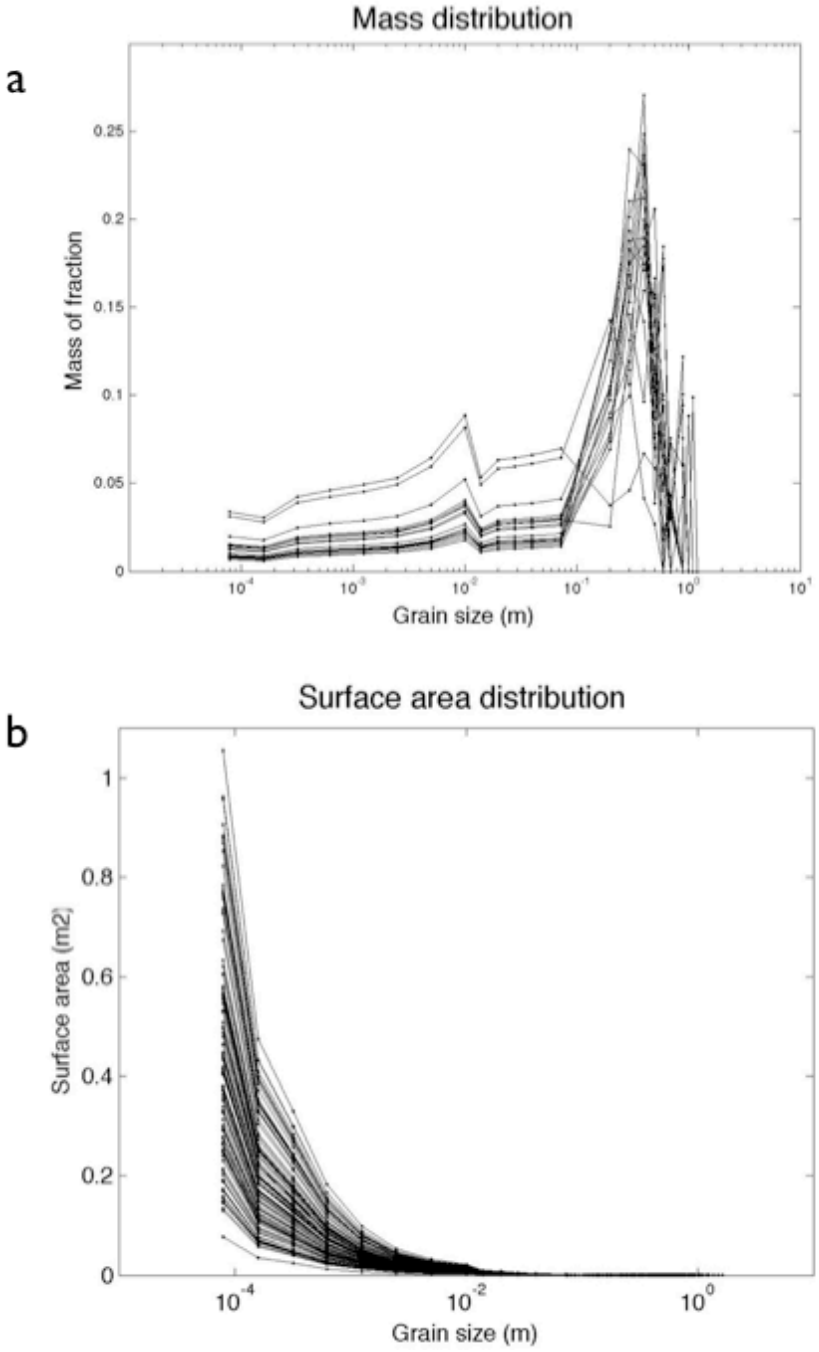

Figure 2 - 12: a) Mass and b) surface area distribution among different grain sizes based on 1 kg of sample. Each line represents a particular sub-region as described in Figure 3 – 8.

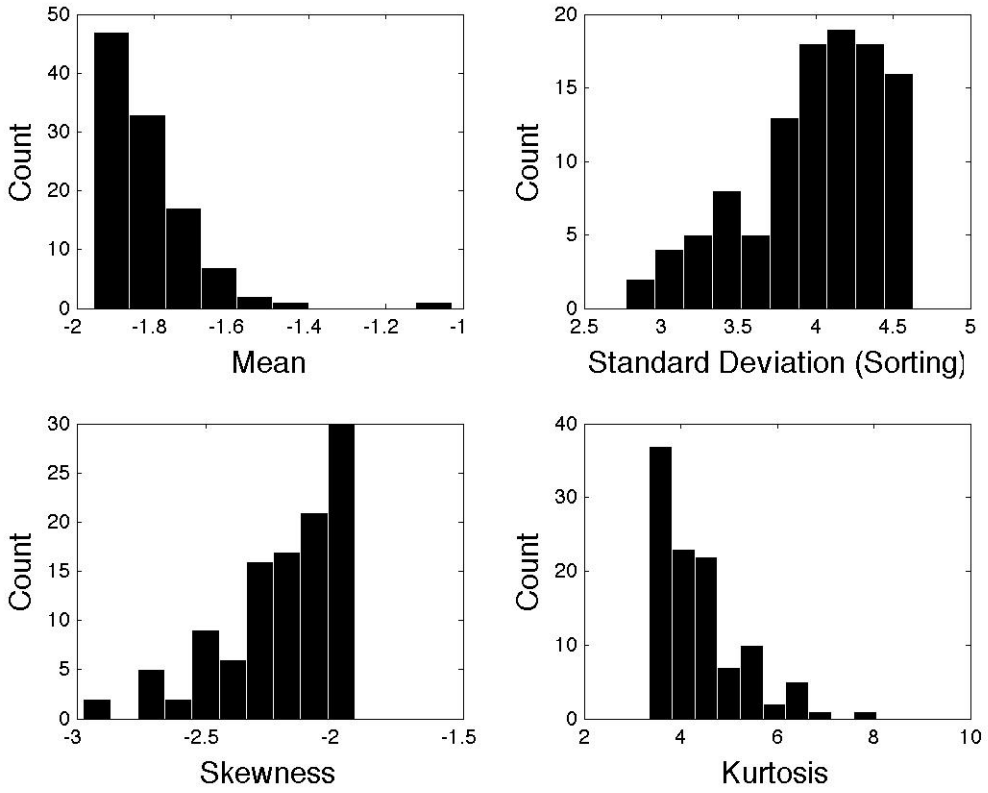

Figure 2 - 13: Histogram of four statistical moments.

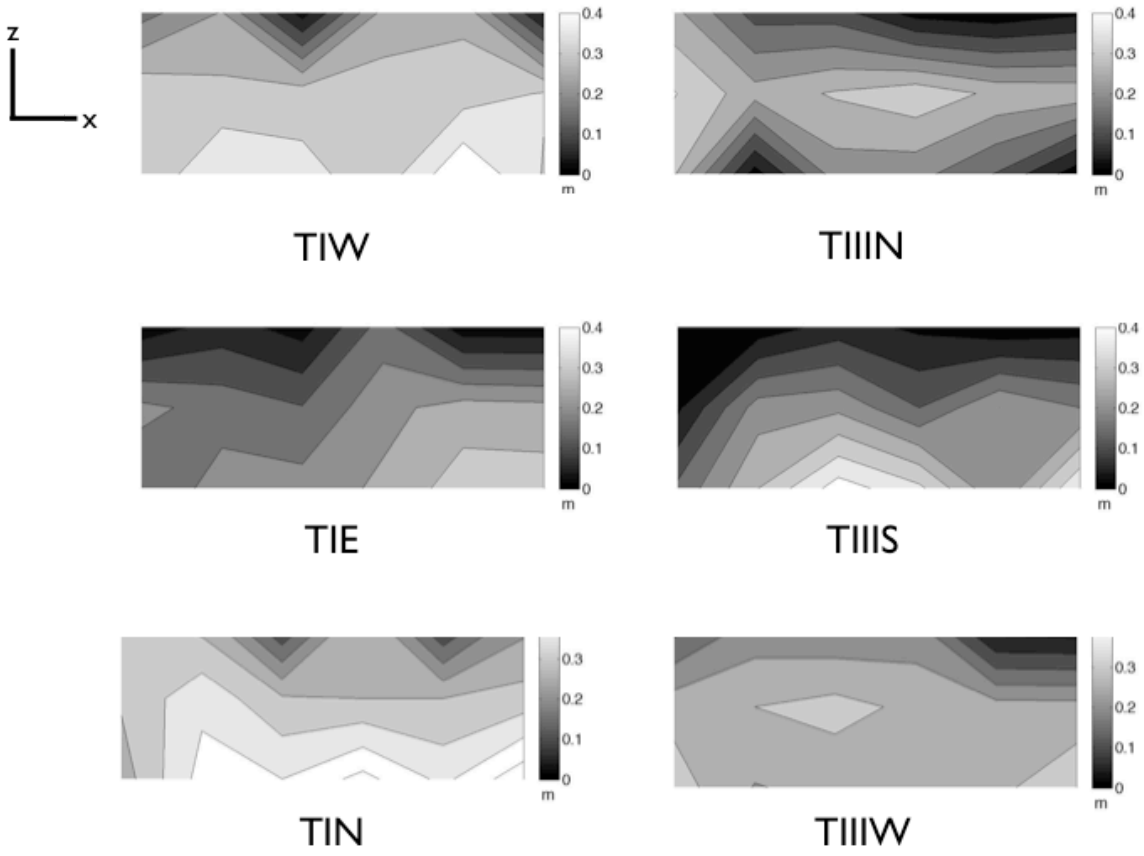

Figure 2 - 14: The d50 contours for the six exposed faces of the TI and TIII test piles. The x-axes represent horizontal displacement and z-axes represent elevation.

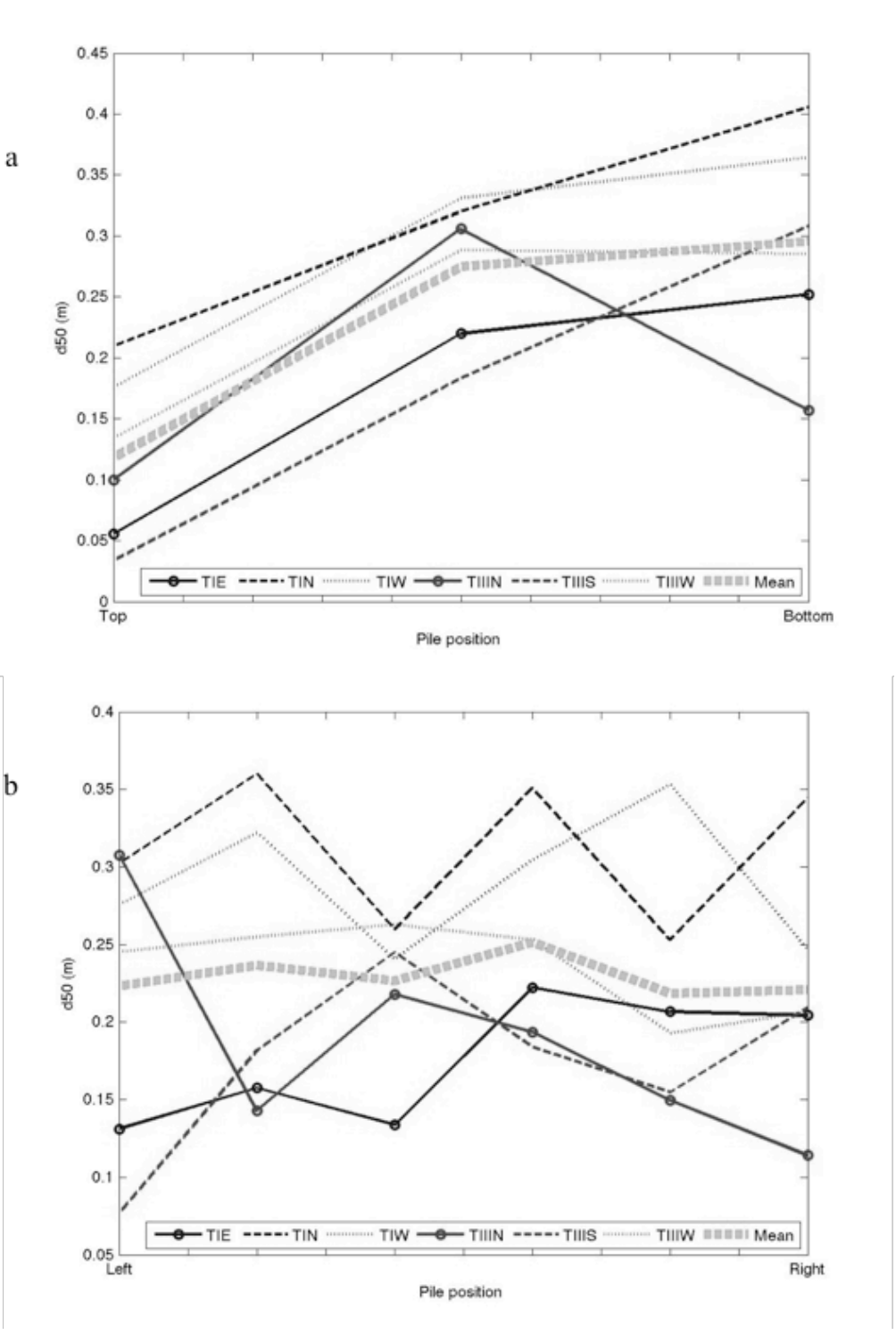

Figure 2 - 15: (a) d50 plotted against vertical displacement, (b) d50 plotted against horizontal displacement.

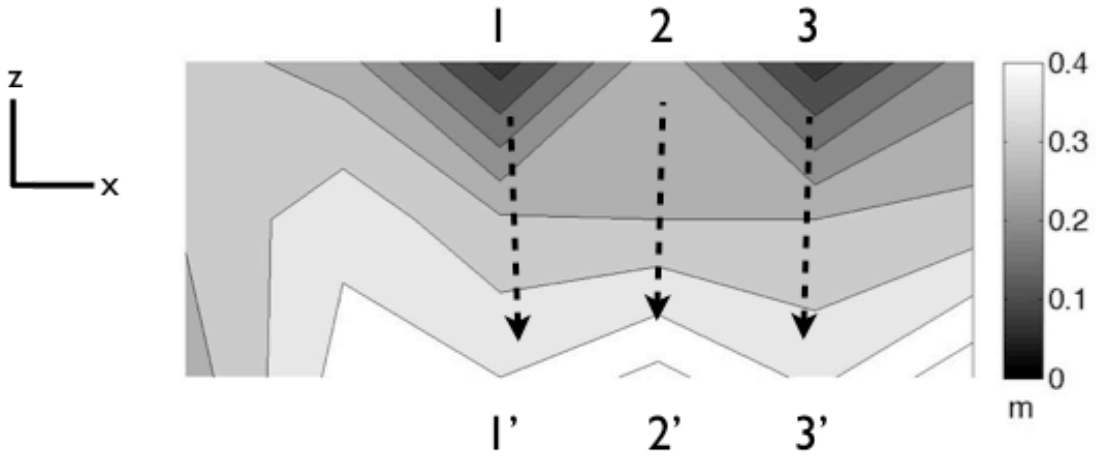

Figure 2 - 16: Grain size bands observed on Face TIN.

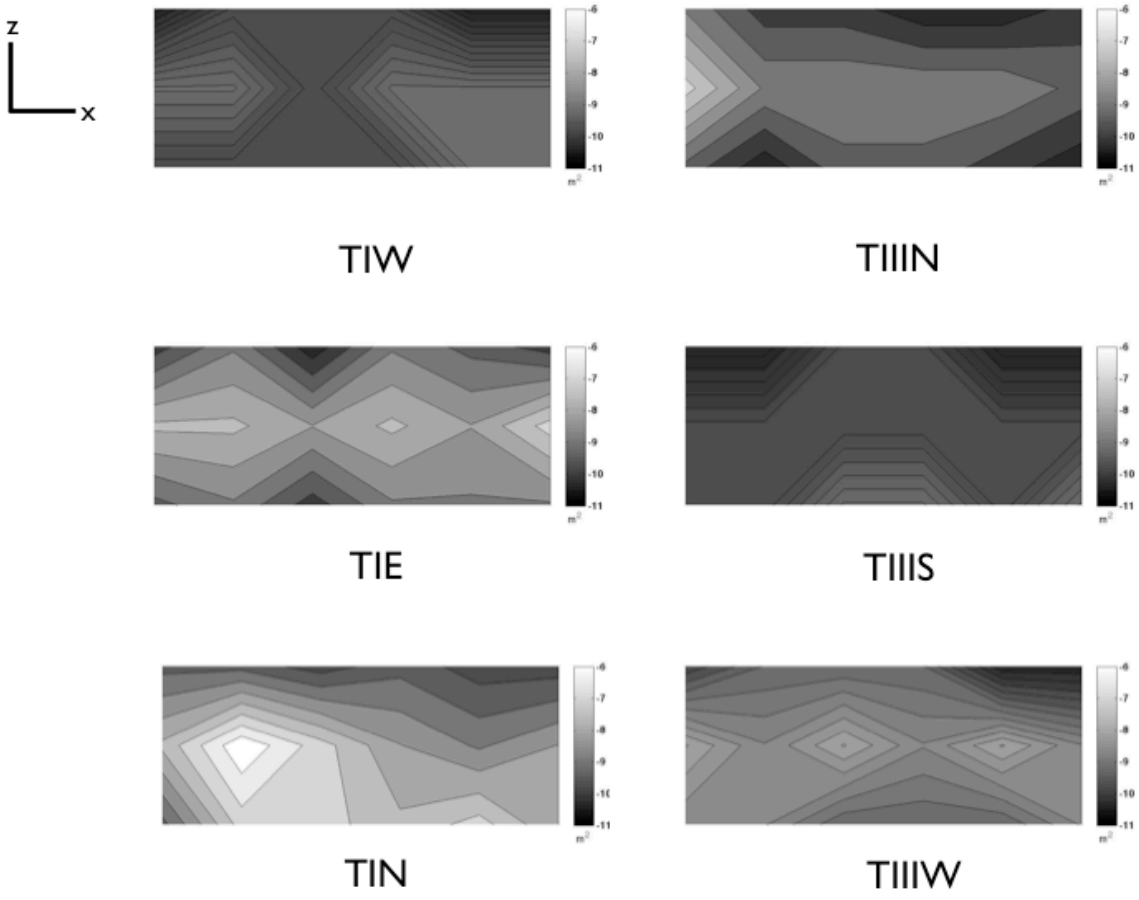

Figure 2 - 17: Permeability distributions calculated using Kozeny-Carmen formula. The contours are in log10-scale.

Chapter 3: Implications of wind-induced pressure in a waste rock pile

3.1 Overview

Wind-induced gas transport in a test-scale unsaturated waste rock pile was investigated at the Diavik Diamond Mine, 300 km northeast of Yellowknife, NWT, Canada. Differential gas pressures were measured in 2008 at 49 locations within the test waste-rock pile and 14 locations on the surface of the pile at one-minute intervals. Wind speed and direction were measured at 10-min intervals and decomposed into north, south, east and west vectors. Correlations between wind vectors and pressure measurements show that the wind influences pressure fluctuations in the pile. The strength of the correlation is roughly inversely proportional to the distance between measurement ports and the atmospheric boundary. The relationship between the magnitude of the wind vector and pressure fluctuations on the surface of the test waste-rock pile was found to be non-linear. However, the relationship between internal pressure measurements and surface pressure measurements was found to be linear, suggesting that gas flow within the pile follows Darcy's Law. Spectral analysis demonstrates that the dominant periods of the wind ranged from 1 to 50 days. A 1D analytical solution to the flow equation demonstrated that the 50-day period had the most pronounced effect on transient gas flow within the pile and the penetration depth of wind induced gas pressure wave is a function of wind periodicity and permeability of the test waste-rock pile.

3.2 Introduction

The recovery of ore from open pit or underground mining operations involves the removal of uneconomical waste rock, which is often stockpiled in large unsaturated piles at the mine site. The biochemical oxidation of sulfide minerals present in the waste rock can result in the generation of acid mine drainage (AMD), characterized by low pH, high dissolved metal content and high concentrations of sulfate, as described by the reaction,

$$FeS_2 + 15/4O_2 + 7/2H_2O \rightarrow Fe(OH)_3 + 2SO_4^{2-} + 4H^+ \qquad (1)$$

Discharge of AMD poses an environmental risk to both surface and groundwater.
The rate and extent of AMD generation can be dependent on a number of factors including the availability of sulfide minerals, the rate of oxygen transport, and the thermal state of the waste rock piles. In many cases the rate of oxygen supply can become the rate-limiting process (Cathles and Apps, 1975; Pantelis and Ritchie, 1992; Ritchie, 1994; Garvie et al., 1997: Lefebvre et al., 2001b) with diffusion and convection generally considered as the dominant oxygen-transport mechanisms (Ritchie, 1994; Bennett et al., 1995; Lefebvre et al., 2001a; 2001b). In northern environments, where the annual average temperature is below 0 ^{0}C, freezing can inhibit water flow while cold temperatures may slow the rates of sulfide oxidation (Neuner et al., 2009; Smith et al., 2009). In waste rock, conduction and density driven convection are typically considered the most significant thermal transport mechanisms (Lu and Zhang, 1997; Lefebvre, 2001a). The availability of oxygen and the thermal state of the waste rock are therefore dependent on the mechanisms and rate of gas transport within the pile.

Anne and Pantelis (1997) and Ritchie and Miskilli (2000) demonstrated the significance of wind driven advective gas transport in waste rock piles. These studies used numerical simulations to demonstrate that wind-induced pressure gradients around a waste-rock pile could significantly enhance oxygen transport into the pile. Similarly, Moghtaderi et al., (2000) simulated gas transport and oxidation in a coal stockpile. These authors found that wind induced advection significantly altered the gas-transport regime within the stockpile, resulting in increased maximum temperatures. Each of these studies assumed a constant wind speed from a fixed direction, and a homogenous internal structure of the piles.

At the Diavik Diamond Mine, in Canada's Northwest Territories, a multidisciplinary project has been conducted to study the physical and geochemical processes controlling AMD generation in waste rock piles in a permafrost environment. The project has involved the construction and instrumentation of three 15 m-scale test waste rock piles ("test piles"), monitoring of thermal, hydrological and geochemical conditions within the pile, and characterization of the physical properties of the waste rock. Amos et al. (2009a) measured gas pressures within and on the surface of one of the test piles and demonstrated that pressure gradients develop within the test pile due to ambient wind conditions, and that the observed gradients could result in significant oxygen transport. In a subsequent study, Amos et al. (2009b) described improvements to the pressure-monitoring system to reduce noise levels. That study more clearly demonstrated the relationship between external wind speed and wind direction to pressures measured within the test pile. Together, the studies showed that erratic changes in wind speed and wind direction have a considerable effect on internal pressure gradients. Furthermore, the observed gradients are distinctly different from those determined from the numerical modeling studies, suggesting that internal heterogeneity is affecting air flow through the pile. Thermal studies of the test piles indicate that the wind driven advection may have significant effects on the depth of the seasonal freeze/thaw layer (Pham et al., 2009)

This paper provides a more detailed and quantitative analysis of the data presented in Amos et al. (2009b) with the specific objective of 1) substantiating the correlation between wind flow external to the test pile and gas pressures within the pile, 2) determining the gas flow regime in the pile, 3) quantifying the effects of changes in wind speed and direction and determining the relevant time scales.

3.3 Site description

At the Diavik Diamond Mine three large-scale experimental waste-rock piles were constructed as described by Smith et al. (2009). This study focuses on the Type III test pile, which contains the highest sulfide content of the waste rock deposited at the site. The rock is predominantly granite, pegamtitic granite and biotite schist with an average sulfide content of

0.052 ± 0.035 wt. % S (n=419). The pile is 15 m high and was constructed by end dumping off a waste rock access ramp using standard mining equipment. The upper surface of the test pile measures 20 m by 50 m and side slopes are at the angle of repose, 1.3 vertical to 1 horizontal (Figure 1). The slopes of the Type III pile are exposed to the atmosphere on the north, west and south sides. Furthermore, there is no physical separation between the eastern margin of the Type III pile and the ramp used for construction.

Measurements of gas pressures are obtained through 3.2 mm (1/8") or 6.4 mm (1/4") O.D polypropylene tubes placed within the waste rock. During construction of the pile, bundles of 15 tubes encased in 50 mm (2") flexible PVC conduit were laid along tip faces at 2.5 and 7.5 m north and south of the east/west centerline. Individual polypropylene tubes in each bundle were terminated through holes in the PVC at 1.3 m intervals to achieve a 1 m vertical sample resolution. Four separate tip faces were instrumented at 20, 15, 10 and 5 m from the external western edge of the pile; labeled faces 1 through 4 in Figure 1.

Pressure measurements were recorded on a subset of the gas-sampling tubes using an automated data-logging system. The system measures differential gas pressures at 49 locations within the test pile and 14 locations on the surface of the pile at one-minute intervals. A detailed description of the data-logging system is given by Amos et al. (2009a) with further enhancements described by Amos et al. (2009b). Briefly, for sampling points within the pile, differential pressure is measured between the sampling point and a reference point approximately 25 mm below the surface of the pile at the location of the sampling bundle using a Modus Series T (±50 Pa) differential pressure transducer. Solenoid valves are employed to allow one transducer to measure seven individual sampling points at each bundle. For sampling points on the surface of the test pile, an additional pressure sensor is located in an instrumentation hut on the top of the pile. This sensor records differential pressure between the surface sampling points and a reference point on the surface at bundle 32N2 (Figure 3 - 1A). Sample tubing for surface pressure measurements are run from the instrumentation hut to the sampling locations through 50 mm PVC conduit to minimize wind effects on the tubing. Additionally, the exposed ends are covered with crushed rock to minimize wind effects on the tubing ends.

Pressure data is recorded at one-minute intervals with a Campbell Scientific CR1000 data-logger. Wind speed and wind direction are recorded at 10 minute intervals using an RM Young Model 05305 wind monitor mounted approximately 7 m above the Type III pile. Pressure data presented in this report was collected from June 9 through November 18, 2008. Data are averaged every 10 minutes to eliminate the short-term oscillations caused by erratic wind changes.

The labels for the measurement ports are shown on Figure 3 - 1. The labeling convention for measurement ports within the pile is as follows: 31N2-12: Type '3' pile, face '1', offset 'N' (north) of centerline, '2' = 2.5 m offset (7 = 7.5 m offset), '-12' = 12 m deep from top surface of the pile ('-S' = surface measurement ≈25 mm deep). For measuring points on the side slopes of the pile the labeling convention is: 3SS-14: Type '3' pile, 'SS' = south slope (NS= north slope, WS = west slope), '-14' = 14 m, vertical distance from the top of the pile (Figure 3 - 1B).

3.4 Results and discussion

3.4.1 Wind characteristics

Wind speed and direction were recorded every 10 minutes from June 10, 2008 to March 15, 2010 (Figure 3 - 2A). Wind speed was highly variable and frequently exceed 20 km/hr. The average wind speed was 15 km/hr and the median wind speed was 13.4 km/hr (Figure 3 - 2B). North and southward winds were most frequent and westward wind was the least frequent (Figure 3 - 2C).

3.4.2 Correlation of wind and pressure measurements

To understand the relationship between pressure and wind from different directions, the original wind speed and wind direction data were decomposed into north, south, west and east vectors. Figure 3 - 3 shows examples of internal pressure measurements 31N2-4, -8, -12 and 32S7-4, -8, -12 plotted against south, north and west vectors with linear regression lines and R^2 values on each plot. The test pile is not exposed to the east and therefore the pressure

response to the east wind vector is weak. The pressure response pattern observed in these plots is typical for other bundles. The response is generally less apparent with winds less than 20 km/hr, and stronger with winds greater than 20 km/hr. The pressure response is different for each wind vector. The responses to north and south vectors are more significant than west because wind is more predominant from the north and south (Figure 3 - 2C), and in addition, structures external to the test pile may influence the impact of a westward wind on the pressures observed within the test pile. The residuals from the linear regression, i.e. the difference between the data and the values predicted by the regression equations, show uneven distributions around zero for high correlation responses (Figure 3 - 4).

Surface pressure measurements at sampling points 3NS-1, -7, -14 and 3SS-1, -7, -14 plotted against south, north and west wind vectors are shown in Figure 3 - 4. Similar pressure response patterns are observed as for the internal pressure measurements with the strongest pressure responses observed at wind speeds greater than 10 to 20 km/hr depending on the location. The strongest pressure responses are observed on the windward side of the pile with residuals unevenly distributed around zero. For example, 3NS measurements show a very weak response to the south and west wind vectors, but a strong response to the north wind vector with the residuals distributed around zero following systematic trends (Figure 3 - 5). These patterns are typical for other surface measurements.

To quantify the relationship between measured wind speed and wind direction with pressure measurements, Pearson's correlation coefficient for four wind vectors and pressure measurements on the surface and within the piles were calculated. The coefficient was between 0 and 1 with 1 being a perfect linear correlation and 0 being no correlation. The closer the coefficient is to 1, the stronger the correlation between the variables (Howell, 2004). In an attempt to account for the non-linear effects on correlation results, Spearman's rank correlations were also calculated. However, because the erratic pressure responses disturbed the ranking, in most cases rank correlations were even weaker than linear correlations. In general, because the relationship between the wind vector and the pressure measurements were only weakly non-linear at high wind speeds, linear correlations appeared to be sufficient to quantify the trends in the data.

The calculated correlation coefficients for pressure measurements on the surface and within the test piles to the north, south, east, and west wind vectors are shown in Figure 3 - 5. For surface measurements (enclosed in dashed rectangle), the correlation to the north wind vector was strong with an average correlation of 0.64 and a maximum correlation of 0.91 for the 14 surface points. The correlation to the south wind vector was slightly weaker with an average correlation of 0.41 and a maximum correlation of 0.84. The correlations to west and east wind vectors were weak with average correlations of 0.32 and 0.20, respectively. This difference occurs because the wind was more predominant from the north and south and the test pile was not exposed to atmosphere from the east (Figure 3 - 1 and Figure 3 - 2C).

In general the correlations to wind vectors were weaker for internal measurements compared to surface pressure measurements. The correlations to the south vector were strongest with an average correlation of 0.41 and a maximum correlation of 0.81. The correlation to the north wind vector was slightly weaker with an average correlation of 0.37 and a maximum correlation of 0.72. The correlations to the west and east vectors were weak with average correlations of 0.25 and 0.12, respectively.

The degree of wind-pressure correlation was roughly proportional to the distance between measurement port and the atmospheric boundary (Figure 3 - 6). For example, a measurement port located close to the north face of the test pile may correlate the north vector with a coefficient of 0.6, but 0.1 with the south vector. The decrease in the correlation coefficient with distance from the atmospheric boundary was likely due to damping of the amplitude of the pressure wave within the pile, and the effects of pile heterogeneity.

3.4.3 Flow regime

As mentioned above, a non-linear relationship exists between the wind vectors and measured pressures within and on the surface of the pile (Figures 3 - 3 and 3 - 4). For example, for 31N2-4, -8, -12 and the north wind vector, the pressure increase is not significant (~ 0 Pa/(km/hr)) with the magnitude of the wind vector at less than 20 km/hr but increases to 2 Pa/(km/hr) when the wind vector exceeds 20 km/hr. The “tipping point” in the magnitude of the wind vector differs at different locations. For example, for 32S7-4, -8, -12

and the south wind vector, the "tipping point" is about 10 km/hr. A similar pattern is observed between wind and surface pressure measurements. However, when internal pressure measurements are plotted against surface pressure measurements, visual inspection shows that the relationship is clearly more linear (Figure 3 - 7). The residuals from the linear regression also show fairly even distributions around zero (Figure 3 - 8). Since the variations can be described by linear models reasonable well, Darcy's Law is considered to be sufficient in describing gas transport in the test piles. This observation also suggests that the non-linearity observed between wind and internal pressure measurements is caused by non-linearity between wind speed and surface pressure measurements.

Reynolds numbers can be calculated to investigate the extent to which fluid inertia dominates the viscous forces, and hence the degree to which the fluid is nonlinear. Reynolds numbers are calculated using:

$$\mathrm{Re} = \frac{VL}{\nu} \qquad (2)$$

where V is the velocity of fluid, L is the traveled length of the fluid and ν is the kinematic viscosity of the fluid. Laminar flow occurs when the Reynolds number is low (order of 10). Transitional flows have typical Reynolds numbers in the hundreds or thousands, and fully turbulent flow occurs when Reynolds number is >4000 (Holman, 2002). Considering wind flow *over* the test pile, using the measured mean wind flow velocity of 15 km/hr (4.2 m/s), the height of the pile (15 m) as a typical length, and 10^{-5} m^2/s as kinematic viscosity for air, a Reynolds number of 6.3×10^5 is calculated. The high Reynolds number indicates that the wind flow over the piles is turbulent and, therefore the pressures induced on the surface of the pile would not be expected to vary linearly in response to the wind speed. Considering gas flow *within* the test pile, based on the observed common pressure gradient 1 Pa/m, kinematic viscosity of air 10^{-5} m^2/s and measured permeability 10^{-9} m^2, a gas-flow velocity of 10^{-4} m/s is calculated (Amos, et al., 2009). The d30, the diameter of particle that 30% of the material is finer than, was determined from image grain size analysis to be approximately 0.01 m (Chi et al., Chapter 2). Using d30 as typical length, a typical flow velocity of 10^{-4} m/s

and kinematic viscosity10^{-5} m^2/s, a Reynolds number of 1 is calculated, indicating that the flow is laminar.

3.4.4 Relevant time scales

The data and analysis presented above demonstrate that the observed pressure gradients within and on the surface of the waste rock pile are highly affected by the variability in wind speed and wind direction. In practice, the extent to which wind penetrates the pile will depend on the persistence of wind events. To understand the timescales relevant to this problem, spectral analysis is performed on wind data collected from June 10, 2008 to March 15, 2010.

The time series of the velocities *C(t)* was decomposed into a sum of sine and cosine components of different frequencies/periods and amplitudes:

$$C(t) = A_0 + \sum A_n \cos\omega_n t + \sum B_n \sin\omega_n t \qquad (3)$$

where ω is frequency and t is time. By decomposing a time series into various frequency components we can investigate the relative importance of these components. The significance, or power, of each component is determined by the magnitude of $\sqrt{A_n^2 + B_n^2}$. The larger $\sqrt{A_n^2 + B_n^2}$ is, the more important the component is. The continuum of all components is represented by the power spectrum. The spectral analysis was implemented by calculating the Discrete Fourier Transform (DFT) of a signal or time series. (Press et al., 1992). The resulting power spectrum is presented in Figure 3 - 8. Frequency is converted to period $T = 2\pi/\omega$ in the plot. The dominant wind components are of periods of approximately 14 days, 17 days and 50 days (Figure 3 - 8A and C). There are also a number of dominant wind components between 1 day and 6 days. These dominant wind periods roughly represent daily, weekly and monthly cycles.

Gas transport can be the main process governing oxygen and thermal transport processes in waste rock piles. Previous modeling efforts on gas flow in waste rock piles assumed constant pressure boundary conditions (Anne and Pantelis, 1997, and Ritchie and Miskilly, 2000). The current observations, however, indicate that the pressure imposed by changes in wind speed and direction can alter gas transport within the waste-rock pile. An

analytical model using the frequency information obtained from spectral analysis is used to investigate the effect of time-dependent boundary conditions. The response to forcing of a single constant frequency (often termed steady state response) at the boundary was considered. Were the forcing to begin from a state of rest, the complete solution would consist of a transient signal that would tend to the steady state response over time. However, the transient cannot increase the depth of penetration into the pile of the pressure imposed at the pile surface. For this reason the conceptually simpler single constant frequency response was considered. The selection of different initial conditions does not influence the results of single constant frequency response.

Consider a 1D transient gas flow in porous media problem governed by Darcy's Law:

$$\frac{\partial P}{\partial t} = D\frac{\partial^2 P}{\partial x^2} \quad (4)$$

where P is pressure, t is time, D is diffusivity with respect to gas flow ($D = \frac{k}{\mu S}$ where k is air permeability, μ is viscosity and S is gas storage factor) and x is distance from the left boundary. Imposing the boundary condition $P\ (x=0,t) = P_0 \cos(\omega t)$, (i.e. the pressure fluctuates with an amplitude P_0 periodically with frequency ω at the pile-atmosphere interface) and $P(x=\infty,t)=0$ (i.e. pressure fluctuations damp out completely very deep into the pile), the analytical solution to Equation 3 is:

$$P(x,t) = P_0 e^{-\sqrt{\frac{\omega}{2D}}x} \cos(\omega t - \sqrt{\frac{\omega}{2D}}x) \quad (5)$$

Pressure profiles for six different times from 0 to 125 days, using a pressure fluctuation period T = 50 days, $\omega = 1/T = 2.3 \times 10^{-7}$ Hz and $D = 10^{-3}$ m s^{-1} (calculated based on measured permeability 10^{-9} m^2, Amos et al., 2009 and assuming gas storage factor is 1,), are shown in Figure 3 - 9. Initially, pressure is highest at the left boundary and exponentially decreases deeper into the pile. The flow direction is towards the pile interior. After 25 days, the pressure peak moves into the pile but the flow direction is still generally towards the pile interior. After 50 days, the pressure peak moves to 100 m into the pile and gas flows both into and out of the pile. After 75 days, pressure at left boundary drops and the flow direction is from the interior of the pile to the pile-atmosphere boundary. After 100 days, the pressure

at the left boundary starts to increase but the flow direction is still generally from the pile interior to the pile-atmosphere boundary. After 125 days, the process has almost completed one cycle, and the pressure profile is back to approximately its initial condition. The change in pressure distribution P/P_0 from 370 m to deeper within the pile remains below 0.01 over the entire cycle.

The 1-D simulation demonstrates that in a large-scale waste-rock pile the pressure within the pile would fluctuate periodically, which would cause periodic changes in the gas flow directions. Pressure fluctuations are most significant close to the pile-atmosphere boundary and drop exponentially deeper into the pile. The degree of pressure drop as depth increases is primarily controlled by the exponential $\sqrt{\frac{\omega}{2D}}$ term. Given that the diffusivity D is fixed, the smaller ω is, the smaller the $\sqrt{\frac{\omega}{2D}}$ term is and the larger $|P(x,t)|$ is at a fixed location. Hence, pressure caused by wind with the longest period "penetrates" deepest into the pile. For example, the penetration depth defined where $P/P_0 < 0.01$ drops from 370 m with a period of 50 days to 250 m with a period of 14 days, 130 m with a period of 6 days and 47 m with a period of 1 day. If ω is fixed and permeability is lowered from 10^{-9} m^2 to 10^{-8} m^2 in the above example, the penetration depth is reduced from 370 m to 100 m. The test-scale waste rock pile has a maximum width of 60 m, which is well below estimated $P/P_0 < 0.01$ penetration depth of 370 m for a wind period of 50 days. This explains why pressure fluctuations are observed even at the deepest measurement ports within the test pile. The 1-D analytical solution also explains why pressure measurements closer to the atmospheric boundary respond to, and correlate better with, the wind. This is because more high frequency/short period wind components can be felt at a shallow depth.

3.5 Conclusions

Correlations between wind and pressure measurements suggest that gas pressures inside a test-scale waste-rock pile responded to wind speed and wind direction external to the pile. A linear relationship between surface and internal pressure measurements suggests a Darcian flow regime within the test pile. Spectral analysis of wind data shows that the most

predominant wind periods are 1, 6, 14, 16 and 50 days. 1-D analytical simulations demonstrated that the penetration depth of the pressure wave was a function of the periodicity of the wind and the permeability of the waste-rock pile. Based on the properties of the test-scale waste-rock pile and ambient wind conditions measured at the site a penetration depth of 370 m would be expected in a large-scale waste rock pile.

3.6 Figures

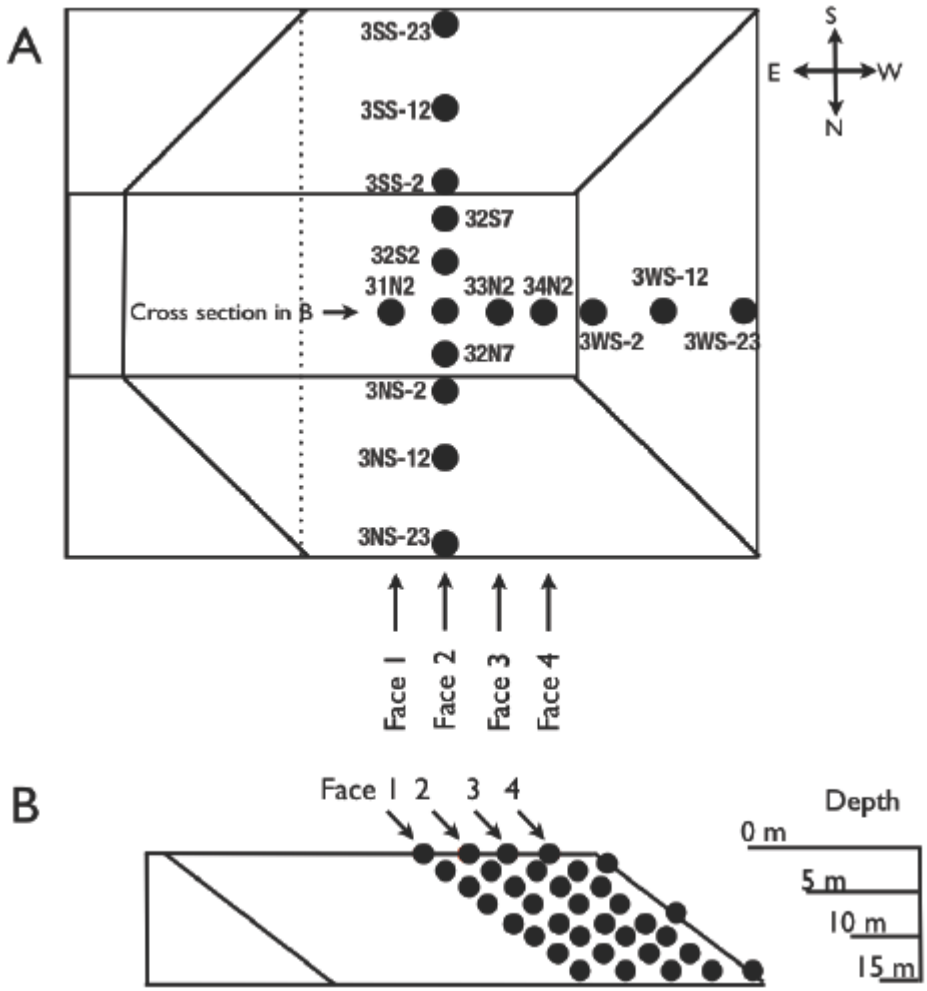

Figure 3 - 1: Illustration of test pile geometry. A: plan view. The symbols on the slopes of the pile represent single sampling points; the symbols shown on top of the pile represent bundles of sampling points. B: Cross section along the line indicated in A.

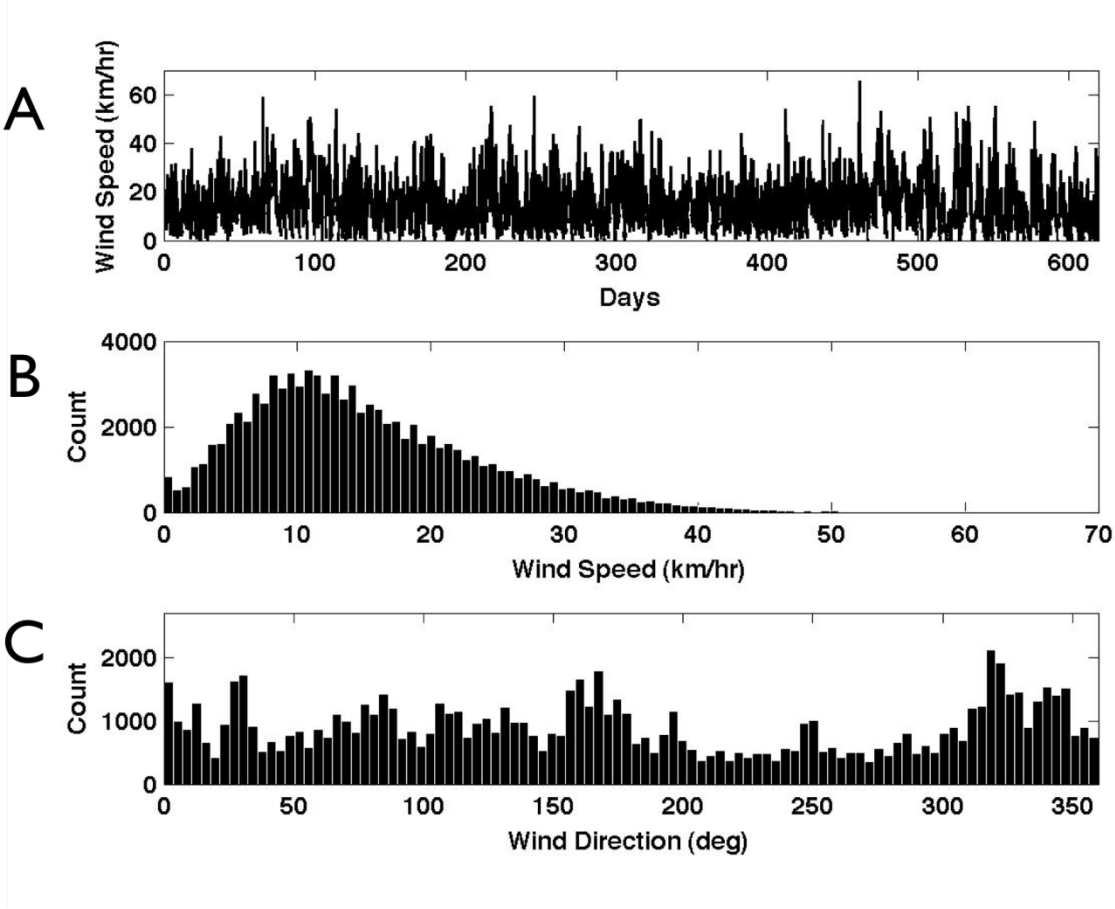

Figure 3 - 2: A: wind time series from June 10, 2008 to March 15, 2010, B: wind speed histogram and C: wind direction histogram. Count is the total number of measurements of a particular wind speed. Direction is related to degree by: north = 360 deg, west = 270 deg

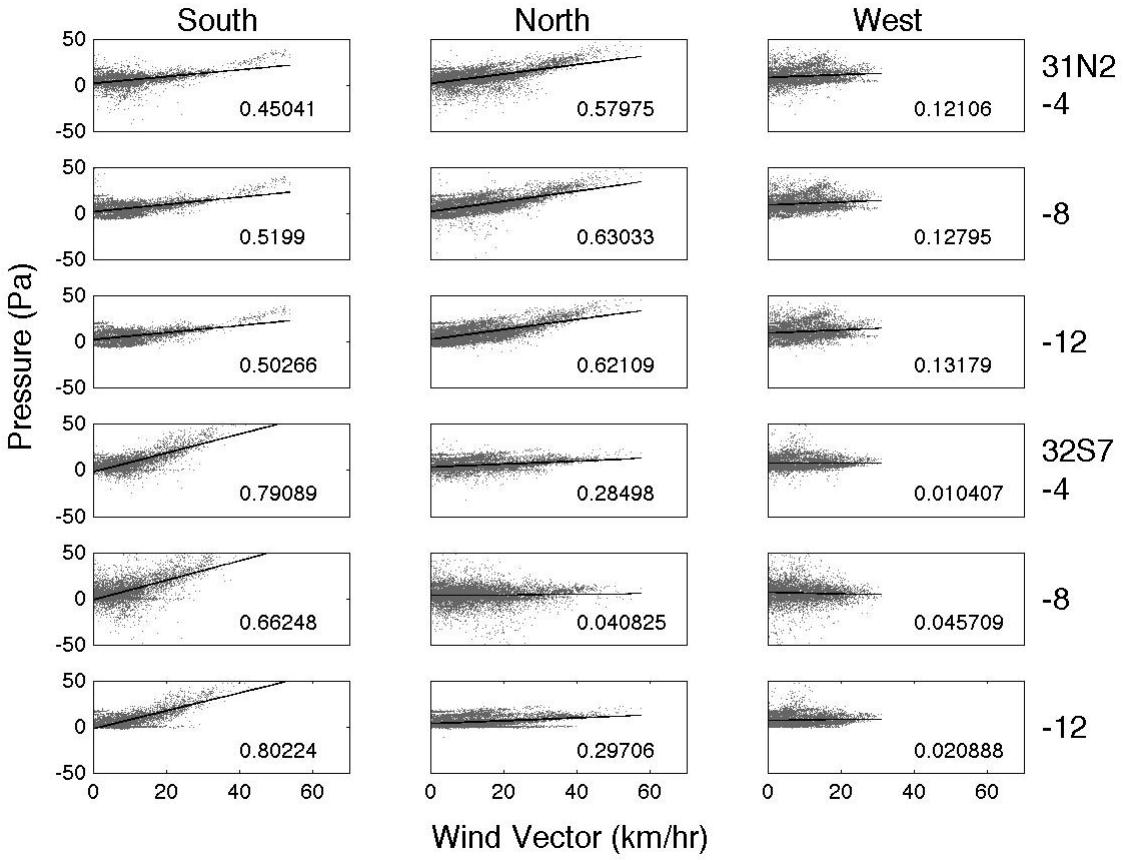

Figure 3 - 3: Differential pressure measurements at internal sampling points 31N2-4, -8, -12 and 32S7-4, -8, -12 plotted against south, north and west vectors. The line in each plot is the best-fit least-square regression line representing linear relationship the pressure measurement and the wind vector. The number in each plot is the R^2 value showing the degree of fit.

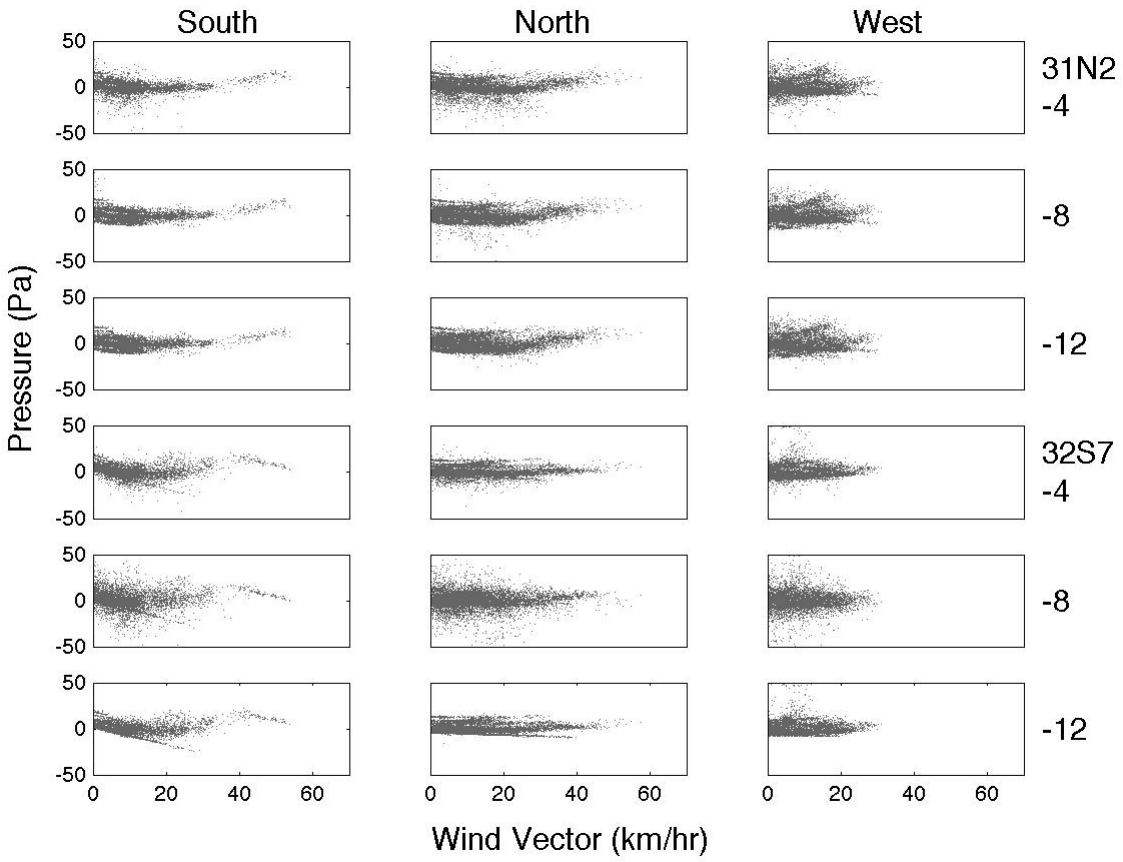

Figure 3 - 4: Residual from the regression lines in Figure 3 – 3. Residual = pressure data - pressure values predicted by the linear models using wind data.

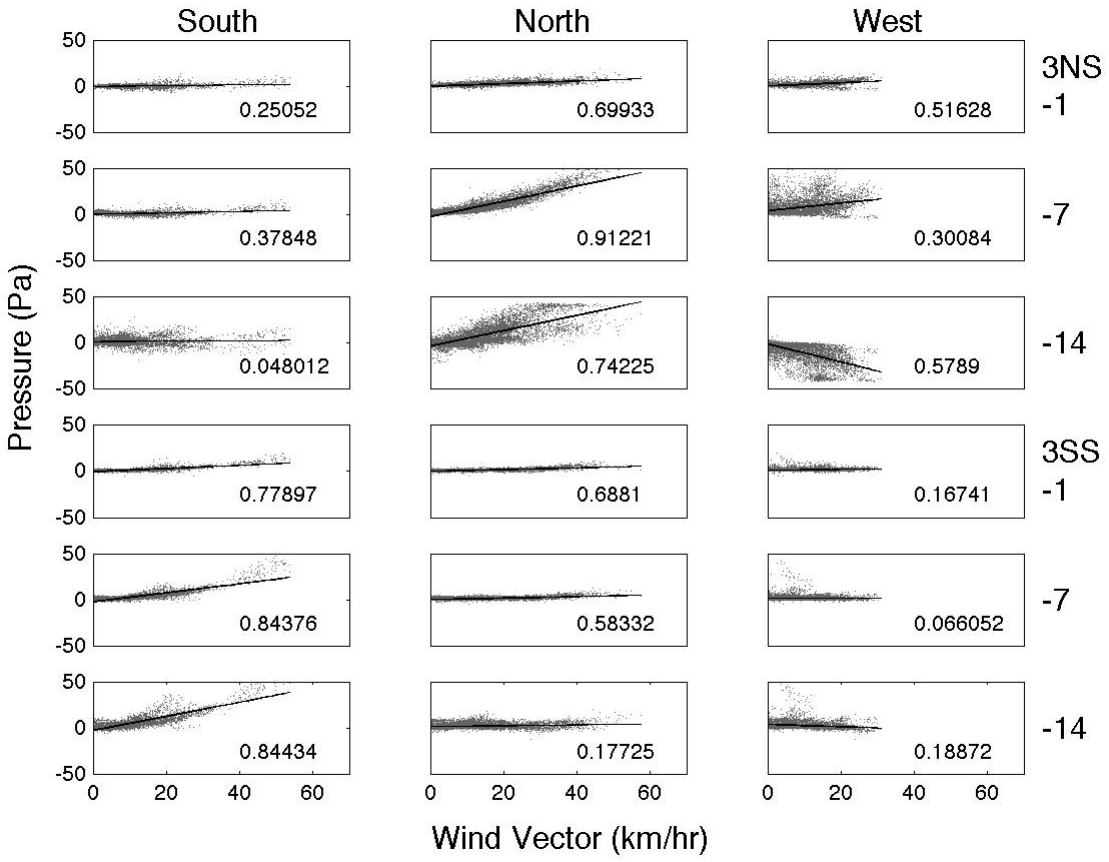

Figure 3 - 5: Differential pressure measurements at surface sampling points 3NS-1, -7, -14 and 3SS-1, -7, -14 plotted against south, north and west vectors. The line in each plot is the best-fit least-square regression line representing linear relationship between the pressure measurement and the wind vector. The number in each plot is the R^2 value showing the degree of fit.

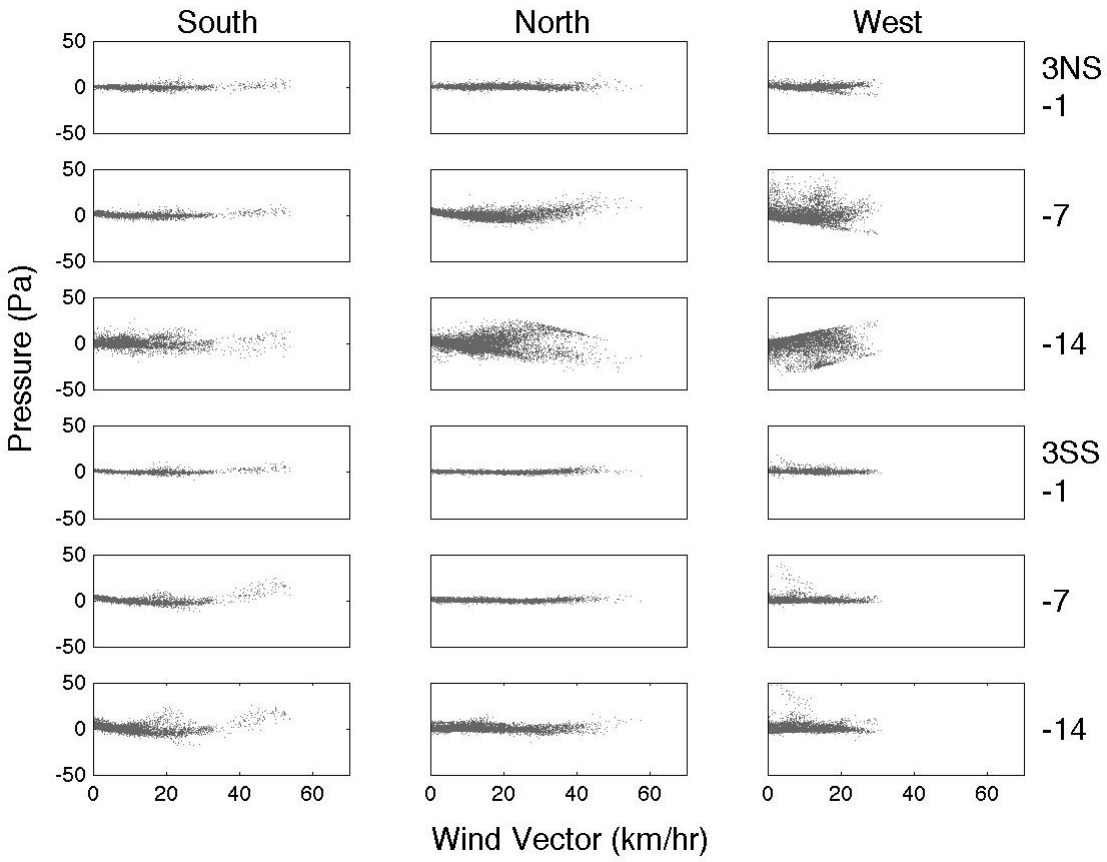

Figure 3 - 6: Residuals from the regression lines in Figure 3 – 5.

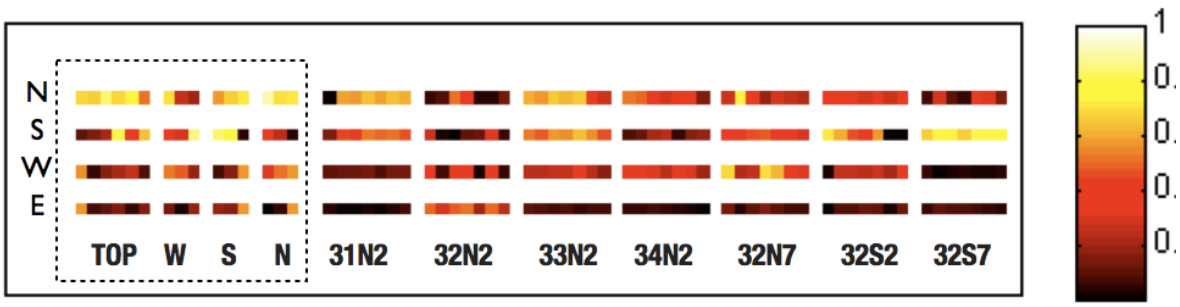

Figure 3 - 7: Correlations coefficients between four wind vectors and all pressure measurements. Dashed rectangle encloses correlations for all surface pressure measurements. "TOP", "W", "S", "N" at the bottom of the dashed rectangle indicate location of the surface measurements (From left to right, "TOP" = 32N2-S, 33N2-S, 34N2-S, 32N7-S, 32S2-S, 32S7-S. "W" = 3WS-14, 3WS-7, 3WS-1. "S" = 3SS-14, 3SS-7, 3SS-1. "N" = 3NS-14, 3NS-7, 3NS-1). "31N2" etc. indicate internal pressure measurement bundles. Measurement port depth increases for each internal bundle from left to right: -2, -4, -6, -8, -10, -12, -14 m.

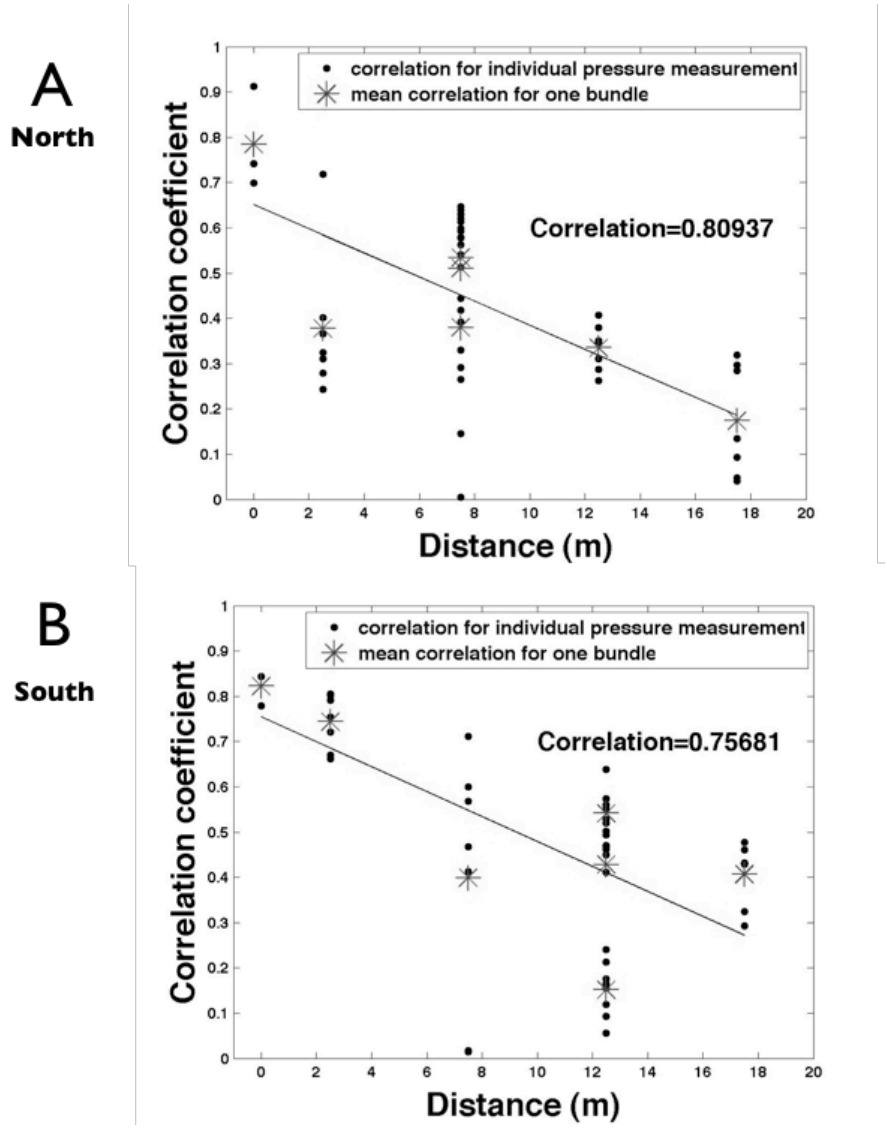

Figure 3 - 8: A: Correlation coefficients of the north wind vector and pressure measurements plotted against distance between pressure measurements to atmospheric north boundary of the pile. B: Correlation coefficients of the south wind vector and pressure measurements plotted against distance between pressure measurements to atmospheric south boundary of the pile. The overall trends are quantified using linear regression of the mean correlations for each bundle.

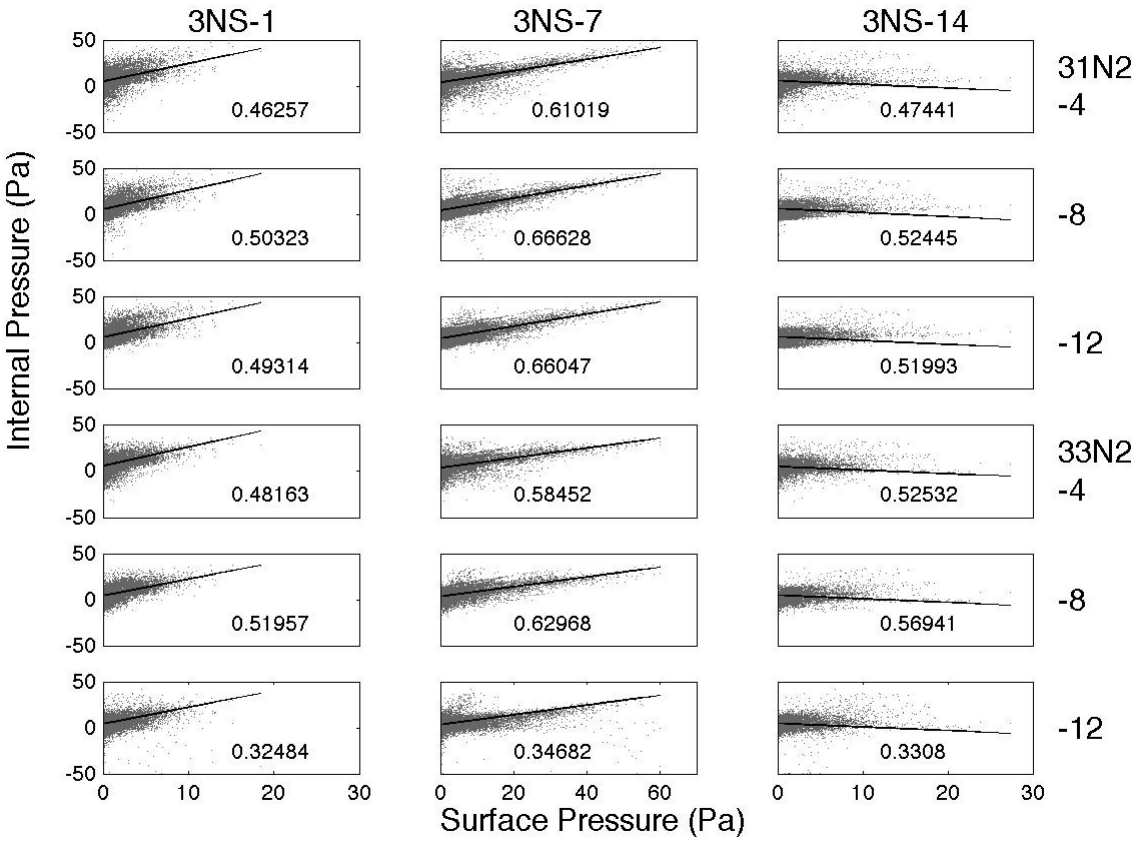

Figure 3 - 9: Internal pressure measurements 31N-4, -8, -12 and 33N2-4, -8, -12 plotted against surface pressure measurement 3NS-1, -7, and -14. Correlation coefficients are shown in each plot. The line in each plot is the best-fit least-square regression line representing relationship between the pressure measurements. The number in each plot is the R^2 value showing the degree of fit.

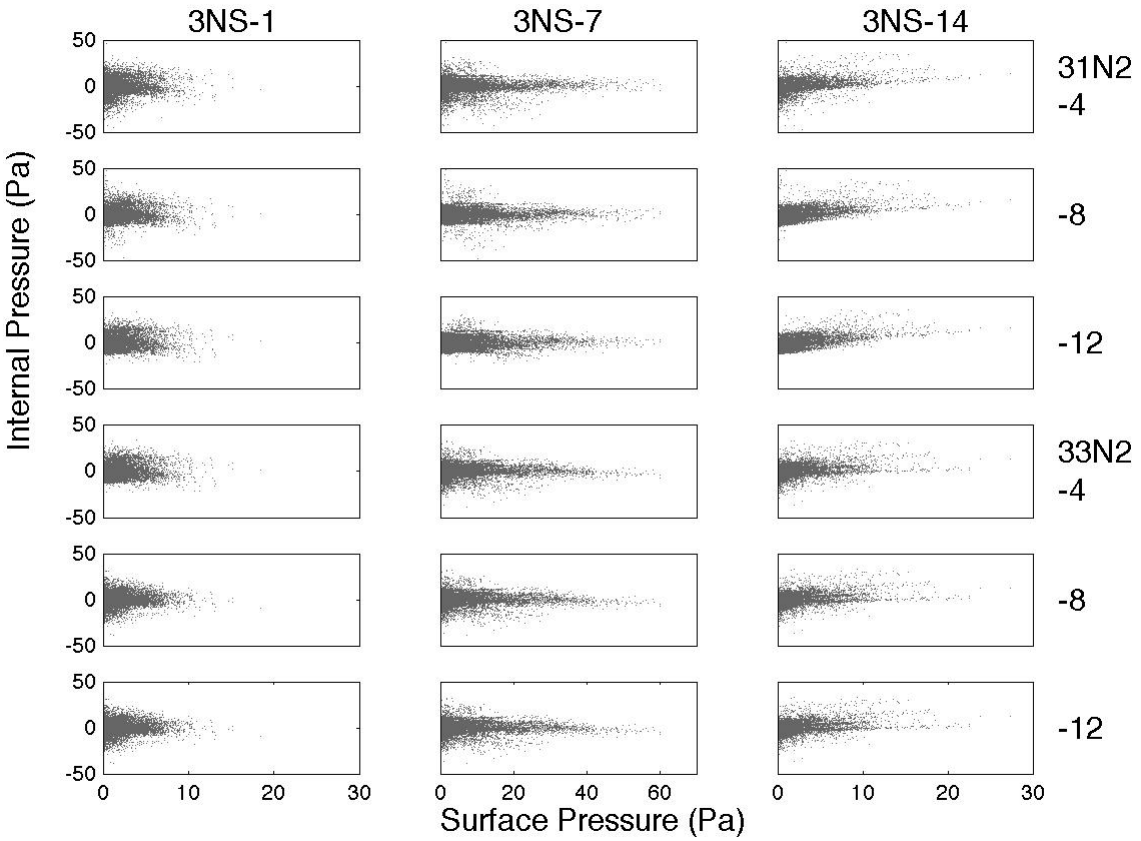

Figure 3 - 10: Residuals from the regression lines in Figure 3 – 9.

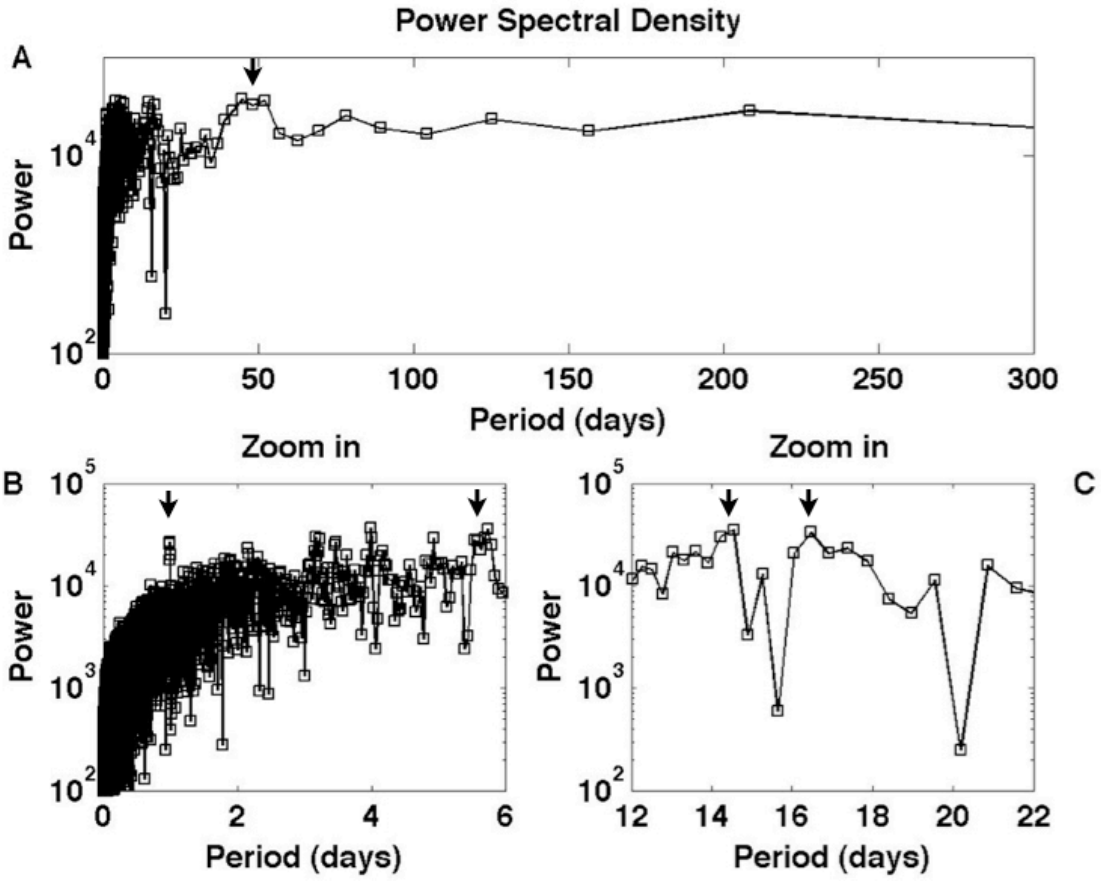

Figure 3 - 11: Power spectral density of wind measurements June 10, 2008 to March 15, 2010. The higher the power, the more important the respective period is. The arrows indicate the predominant periods as discussed in the text.

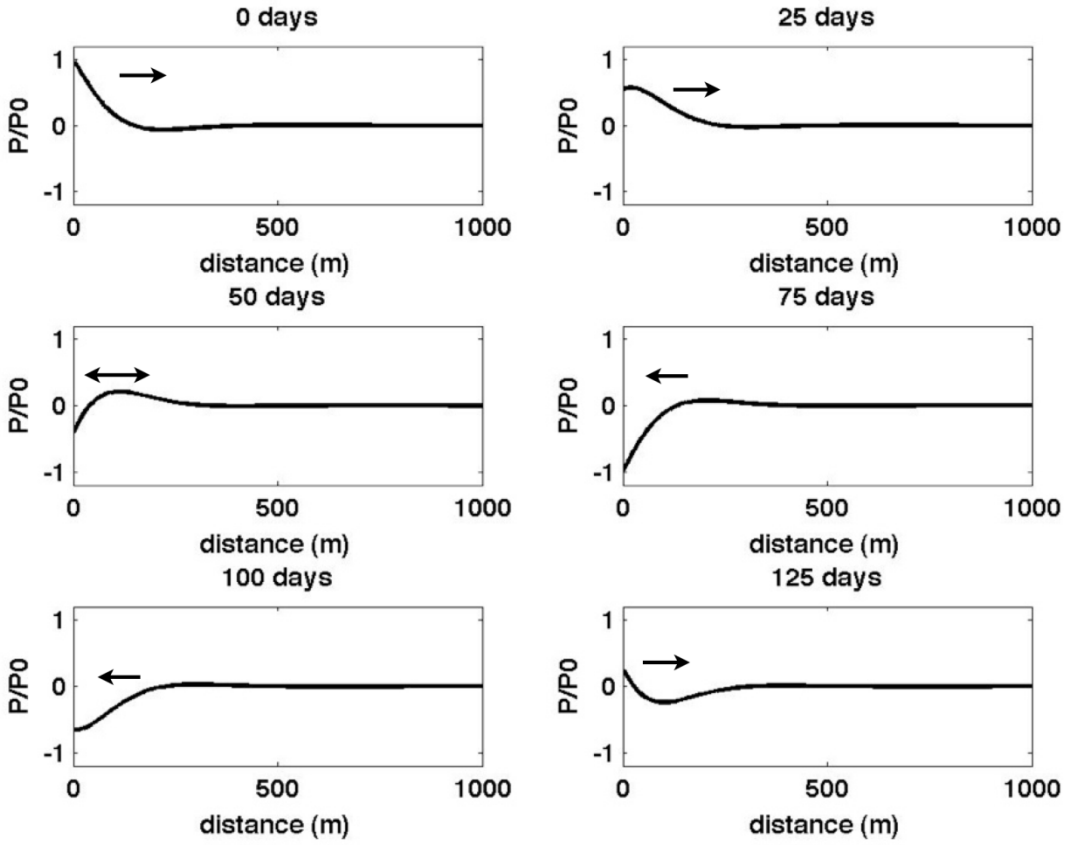

Figure 3 - 12: Pressure profile snapshots at 25 days interval from 1-D analytical solution to the flow equation. The arrow in each plot indicates the direction of major pressure gradient.

Chapter 4: Conclusions

This thesis addresses two issues in waste-rock pile studies that often limit our ability in quantitatively predicting field observations using conceptual and numerical models. These include the heterogeneity of waste-rock piles, and the significance and time-dependence of wind-induced gas transport in waste rock piles.

Heterogeneity was characterized by quantifying spatial grain-size distribution of the test-scale waste-rock piles ("test piles). A digital image processing method was developed to exact grain-size distribution information from photographs of the test pile tip faces. The method was applied to photographs of six tip faces of two test piles. In conjunction with sieve analysis, the image analysis results provide a full-spectrum grain-size distribution, accounting for grain sizes ranging from boulders to sub-millimeter fines. The results show a systematic trend in grain-size distribution: fine-grained material is retained at the top of the test piles and average grain size increases non-linearly from the top to the bottom of the test piles. Calculations show that although the greatest mass is associated with the medium and coarse fractions, the greatest surface area is associated with the fine fractions, which is supported by pore-water chemistry showing more extensive reactions at the top of the test piles and saturated hydraulic conductivity being lower at the top of the test piles than in the pile interior. Statistical moment calculations show that the test piles have mean grain size of granules (17.26 mm< mean diameter <242 mm) and are very poorly sorted, coarse skewed and leptokurtic. These calculations suggest that the permeability of the upper portion of the

test piles are lower than that of the lower zones. Previous measurements also show lower saturated hydraulic conductivity values at the top of the test piles than in the pile interior.

Wind-induced gas transport was studied by substantiating the relationship between wind external to the test piles and pressure within one of the test piles. The correlations between differential pressure data and wind data show that wind has an influence on the pressure fluctuation within the test pile. The strength of the influence is roughly inversely proportional to the depth of the sampling point within the test pile. Pressure responds to wind in a non-linear manner such that the response is more significant at high wind speeds than at low wind speeds. This is likely the result of wind being more persistent in a certain direction at high wind and the non-linear effects exterior to the test pile. The assumption that gas flow within the test pile is Darcian is supported by the observation that there is a linear relationship between pressure measurements made on the surface of the test pile and within the test pile. A one-dimensional analytical solution is used to demonstrate that the depth of wind-induced pressure wave penetration is a function of the frequency of wind and the permeability of the test pile. Based on the properties of the test-scale waste-rock pile and ambient weather conditions, the penetration depth of a large-scale waste-rock pile is estimated to be 370 m. The depth of wind influence is important in understanding the interaction between wind-induced gas transport and other gas, thermal and water transport processes.

The characterization of heterogeneity and time-dependence of wind-induced gas transport can be used in conjunction with conceptual and numerical models such as those described by Bennett et al. (1995), and multi-phase models, for example, described by

Lefebve et al. (2001a,b), to provide improved description of gas transport in waste-rock piles. Because wind brings both gas and thermal energy into the waste rock piles, the following implications to systems of coupled processes can be considered: 1) wind-induced pressure fluctuation is a significant mechanism driving gas transport and potentially an important source of oxygen supply for sulfide oxidation; 2) thermal transport may include wind-driven energy. The estimation of surface-area obtained by grain-size analysis provides a key parameter in geochemical speciation calculations. Multi-dimensional geochemical modeling may help better understand the spatial systematic patterns in aqueous chemistry observed in the field. The spatial permeability distribution will provide a conductivity field for hydrological, thermal and gas flow and transport models.

Recommendations

Since the relative magnitude of spatial permeability can be estimated from the grain-size distribution obtained from image grain size analysis using empirical formulae, inverse modeling methods calibrated against hydrological or geochemical data may be effective in determining permeability distributions. The comparison between estimates made using empirical formulae, inverse modeling, field observations and possibly theoretical development would provide insight into the factors controlling permeability of waste-rock piles. In addition, approaches to quantify the non-linear relationship between wind and pressure should be explored. Darcy's Law with Brinkman's extension can be tested to describe the flow in the "boundary layer" at the wind-atmospheric boundary.

The rich spatial and temporal data set obtained from the Diavik waste-rock project provides an opportunity to examine the coupled relationship between hydrological, geochemical, thermal processes. At the time of this thesis, the field data have only been examined independently or in pairs. Multivariate analysis of the data may reveal more details on the relationship between observations. Specifically, principal component analysis can be conducted to lower the dimensions of variations and identify the processes that account for majority of the variation. Therefore, the relative importance of processes may be determined. Cluster analysis may be used to understand the spatial variation of field measurements.

To limit wind-induced gas transport, waste-rock piles can be constructed to orient the tip faces in the low wind direction. Topographical structures can be constructed around the waste-rock piles to reduce the strength of incoming wind.

References

Chapter 1

Amos, R.T., Blowes, D.W., Smith, L., Sego, D.C. 2009a. Measurement of wind induced pressure gradients in a waste rock pile. Vadose Zone J. 8: 953-962.

Amos, R.T., Smith, L., Neuner, M., Gupton, M., Blowes, D.W., Smith, L., Sego, D.C. 2009b. Diavik Waste Rock Project: Oxygen Transport in Covered and Uncovered Piles. Proceedings of Securing the Future and 8th ICARD, June 22-26, 2009, Skellefteå, Sweden.

Anne, R.D. and Pantelis, G. 1997. Coupled natural convection and atmospheric wind forced advection in above ground reacting heaps. p. 453-458. In International Conference on Computational Fluid Dynamics in Mineral and Metal Processing and Power Generation. Melbourne, Australia. 3-4 July, 1997. CSIRO, Australia.

Arenson, L.U., and Sego, D.C. 2007. Protection of mine waste tailing ponds using cold air convection. In Assessment and Remediation of Contaminated Sites in the Arctic and Cold Climates (ARCSACC). Edited by K. Biggar, G. Cotta, M. Nahir, A. Mullick, J. Buchko, a. Ho, and S. Guigard. Edmonton, AB, Canada. May 7-8, 2007, pp. 256-264.

Benner, S.G., Blowes, D.W., Ptacek, C.J., and Mayer, K.U. 2002. Rate of sulfate removal and metal sulfide precipitation in a permeable reactive barrier. Appl. Geochem. 17: 201-320.

Bennett, J.W., Garvie, A.M., Pantelis, G., Ritchie, A.I.M., Bell, A.V., Noel, M. 1995. Comparison of measured and predicted transport processes controlling oxidation in the waste rock piles at the Health Steel mine site. p. 1017-1026. *In* T.P. Hynes and M.C. Blanchette (eds.), Sudbury ’95, Conference on mining and the environment. Sudbury, Ontraio, Canada. May 28 – June 1, 1995. CANMET, Ottawa.

Berner, R.A. 1980. Early Diagenesis: A Theoretical Approach. Princeton, NJ: Princeton University Press.

Cathles, L.M., Apps, J.A. 1975. A model of dump leaching that incorporates oxygen balance, heat balance, and air convection, Metall. Trans. B 6: 617–624.

Cozarelli, I.M., Hermann, J.S., Parnell, R.A. 1987. The mobilization of aluminum in a natural soil system: effects of hydrologic pathways. Water Resour. Res. 23: 859–874.

DDMI. 2009. Davik Diamond Mine Fact Book, January 2009.

Garvie, A.M., Bennett, J.W., Ritchie, A.I.M. 1997. Quantifying the spatial dependence of the sulfide oxidation rate in a waste rock dump at Mt. Lyell, Tasmania. p. 333-349. In Proceedings of the Fourth International Conference on Acid Rock Drainage. Vancouver, British Columbia, Canada. May 30-June 6: 1997.

Gould, W.D., Kapoor, A. 2003. The microbiology of acid mine drainage. In: Jambor, J.L., Blowes, D.W. and Ritchie, A.I.M. (Eds.), Environmental Aspects of Mine Wastes, Mineral. Assoc. Can. Short Course, 31: 203-226.

Hollings, P., Hendry, J., Nicholson, R., Kirkland, R. 2001. Quantification of oxygen consumption and sulphate release rates for waste rock piles using kinetic cells: CluV Lake uranium mine, Northern Saskatchewan, Canada. Appl. Geochem. 16: 1215–1230

Kyhn, C., and Elberling, B. 2001. Frozen cover actions limiting AMD from mine waste deposited on land in Arctic Canada. Cold Reg. Sci. Technol. 32(2-3): 133-142.

Lefebvre, R., Hockley, D., Smolensky, J. and Gélinas, P. 2001a. Multiphase transfer processes in waste rock piles producing acid mine drainage 1: Conceptual model and system characterization. J. Contam. Hydrol. 52:165-186.

Lefebvre, R., Hockley, D., Smolensky, J. and Lamontagne, A. 2001b. Multiphase transfer processes in waste rock piles producing acid mine drainage 2: Application of numerical simulation. J. Contam. Hydrol. 52:137-164.

Malstrom, M.E., Destouni, G., Banwart, S.A. and Stromberg, B.H. 2000, Resolving the scale-dependence of mineral weathering rates, Environ. Sci. Technol., 34: 1375–1378.

Massmann, J., and Farrier, D.F. 1992. Effects of atmospheric pressures on gas transport in the vadose zone. Water. Resour. Res. 28:777– 791.

Moghtaderi, B., Dlugogorski, B.Z., Kennedy, E.M. 2000. Effects of wind flow on self-heating characteristics of coal stockpiles. Process. Saf. Environ. 78:445-453.

Moncur, M.C., Ptacek, C.J., Blowes, D.W., Jambor, J.L. 2005. Release, transport and attenuation of metals from an old tailings impoundment. Appl. Geochem. 20: 639-659.

Murr, L.E., Schlitt, W.J., Cathles, L.M. 1981. Experimental observations of solution flow in the leaching of copper-bearing waste, in Interfacing Technologies in Solution Mining, Proceedings of the 2nd SME-SPE International Solution Mining Symposium, edited by W. J. Schlitt, pp. 271–290, Soc. for Min., Metal., and Explor., Denver, Colo.

Neuner, M. 2009. Water flow through unsaturated mine waste rock in a region of permafrost. MSc Thesis. University of British Columbia, Vancouver, BC, Canada.

Nichol, C., Smith, L., Beckie, R. 2005. Field-scale experiment of unsaturated flow and solute transport in a heterogeneous porous medium. Water Resour. Res. 41: W05018.

Nordstrom, D.K., Alpers, C.N. 1999. Negative pH, efflorescent mineralogy, and consequences for environmental restoration at the Iron Mountain Superfund site, California. Proc. Natl. Acad. Sci. 96, 3455-3462.

Ritchie, A.I.M. 1994. Sulfide oxidation mechanisms: controls and rates of oxygen transport. pp. 201–245. *In* J.L. Jambor and D.W. Blowes (eds.), Environmental Geochemistry of Sulfide Mine-wastes; Mineralogical Association of Canada, Short Course Handbook Vol. 22.

Ritchie, A.I.M. and Miskelly, P. 2000. Geometric and physico-chemical properties determining sulfide oxidation rates in waste rock dumps. pp. 277-287. In Proceeding Fifth International Conference on Acid Rock Drainage, ICARD-2000. Denver, Colorado. May 21-24, 2000. Society for Mining, Metallurgy, and Exploration Inc., Littleton, Colorado, USA.

Pantelis, G. and Ritchie, A.I.M. 1992. Rate limiting factors in dump leaching of pyritic ores, Appl. Math. Modell. 16, 553–560.

Schnoor, J.L. 1990. Kinetics of chemical weathering: a comparison of laboratory and Weld weathering rates. In: Stumm, W. (Ed.), Aquatic Chemical Kinetics. Wiley-Interscience, New York, pp. 75–534.

Singer, P.C. and Stumm, W. 1970. Acidic mine drainage: the rate determining step. Science 167: 1121–1123.

Smith, L. and Beckie, R. 2003. Hydrological and geochemical transport processes in mine waste rock, Ch 3 in Environmental Aspects of Mine Wastes, Mineral. Assoc. Canada, Short Course Series Volume 31, pp. 51–72, April, 2003.

Smith, L.J.D. 2009. Building and Characterizing Low Sulfide Instrumented Waste Rock Piles: Pile Design and Construction, Particle Size and Sulfur Characterization, and Initial Geochemical Response. MSc Thesis, University of Waterloo, Waterloo, ON, Canada.

Stromberg, B., Banwart, S. 1994. Kinetic modeling of geochemical processes at the Aitik mining waste rock site in northern Sweden. Appl. Geochem. 9: 585-595.

Stromberg, B., Banwart, S. 1999. Experimental study of acidity-consuming processes in mining waste rock: some influences of mineralogy and particle size. Appl. Geochem. 14: 1-16.

Velbel, M.A. 1993. Constancy of silicate-mineral weathering-rate ratios between natural and experimental weathering: implications for hydrologic control of differences in absolute rates. Chem. Geol. 105: 89–99.

Wagner, K., Smith, L., Beckie, R. 2006. Geochemical characterization of mine waste rock from an experimental Pile, Cluff Lake, Saskatchewan, Proceedings of the 7th International Conference on Acid Rock Drainage, St. Louis. Mo., USA, 15 pages, March 2006.

Weeks, E.P. 1993. Does the wind blow through Yucca Mountain. pp. 45–53. *In* D. Evans and T. J. Nicholson (eds.), Proceedings of Workshop V: Flow and Transport Through Unsaturated Fractured Rock Related to High-Level Radioactive Waste Disposal, NUREG CP-0040. U.S. Nucl. Regul. Comm., Rockville, Md. USA.

Chapter 2

Amos, R.T., Blowes, D.W., Smith, L., Sego, D.C. 2009a. Measurement of wind induced pressure gradients in a waste rock pile. Vadose Zone J. 8: 953-962.

Amos, R.T., Smith, L., Neuner, M., Gupton, M., Blowes, D.W., Smith, L., Sego, D.C. 2009b. Diavik Waste Rock Project: Oxygen Transport in Covered and Uncovered Piles. Proceedings of Securing the Future and 8th ICARD, June 22-26, 2009, Skellefteå, Sweden.

Anne, R.D. and Pantelis, G. 1997. Coupled natural convection and atmospheric wind forced advection in above ground reacting heaps. p. 453-458. In International Conference on Computational Fluid Dynamics in Mineral and Metal Processing and Power Generation. Melbourne, Australia. 3-4 July, 1997. CSIRO, Australia.

ASTM D422-63 Standard Test Method, 2002. Standard test method for particle-size analysis of soils. In: Annual Book of ASTM Standards, American Society for Testing and Materials.

Azam, S., Wilson, W.G., Herasymuik, G., Nichol, C., Barbour, L.S. 2007. Hydrogeological behaviour of an unsaturated waste rock pile: A case study at the Golden Sunlight Mine, Montana, USA. Bull. Eng. Geol. Environ. 66 (3), pp. 259-268.

Bennett, J.W., Garvie, A.M., Pantelis, G., Ritchie, A.I.M., Bell, A.V., Noel, M. 1995. Comparison of measured and predicted transport processes controlling oxidation in the waste rock piles at the health steel mine site. pp. 1017-1026. *In* T.P. Hynes and M.C. Blanchette (eds.), Sudbury ’95, Conference on mining and the environment. Sudbury, Ontraio, Canada. May 28 – June 1, 1995. CANMET, Ottawa.

Carman, P. C. 1938. The determination of the specific surface of powders. J. Soc. Chem. Ind. Trans. 57: 225.

Carman, P. C. 1956. Flow of Gases Through Porous Media, Butterworths Scientific Publications, London.

Chi, X., Amos, R., Stastna, M., Blowes, D.W., Smith, L., and Sego, D.C. Implications of wind-induced pressure in a waste rock pile. Chapter 3 of this thesis.

Duda, R. and Hart, P. 1973. Pattern Classification and Scene Analysis. John Wiley and Sons, pp. 271-2.

Fernlund, J.M.R. 2005a. Image analysis method for determining 3-D size distribution of coarse aggregates. Bull. Eng. Geol. Environ. 64: 159–166.

Fernlund, J.M.R. 2005b. Image analysis method for determining 3-D shape of coarse aggregate. Cem. Concr. Res. 35: 1629–1637.

Fernlund, J.M.R. 2005c. 3-D image analysis size and shape method applied to the evaluation of the Los Angeles test. Eng. Geol. 77: 57–67.

Fu, K.S., Mui, J.K. 1981. A survey on image segmentation. Pattern Recognit., 13 (1), pp. 3-16.

GIMP, 2009. (Version 2.6.8) [Software]. Available from http://www.gimp.org/

Gonzalez, R. and Woods, R. 1992. Digital Image Processing, Addison-Wesley Publishing Company, 1992, pp 518 - 519, 549.

Hollings, P., Hendry, J., Nicholson, R., Kirkland, R. 2001. Quantification of oxygen consumption and sulphate release rates for waste rock piles using kinetic cells: CluV Lake uranium mine, Northern Saskatchewan, Canada. Appl. Geochem. 16: 1215–1230

Igathinathane, C., Pordesimo, L.O., Columbus, E.P., Batchelor, W.D., Methuku, S.R. 2008. Shape identification and particles size distribution from basic shape parameters using ImageJ. Comput. Electron. Agric. 63: 168–182.

Kass, M., Witkin, A., and Terzopoulos, D.1987. Snakes: Active contour models. Int. J. Comput. Vision. 1(4): 321-331.

Kozeny, J. 1927. Ueber kapillare Leitung des Wassers im Boden. Wien, Akad. Wiss. 136(2a): 271.

Kwan, A.K.H., Mora, C.F., Chan, H.C. 1999. Particle shape analysis of coarse aggregate using digital image processing. Cem. Concr. Res. 29: 1403–1410.

Krumbein, W.C., Pettijohn, F.J. 1938. Manual of Sedimentary Petrography. Appleton-Century-Crofts: New York.

Lefebvre, R., Hockley, D., Smolensky, J. and Gélinas, P. 2001a. Multiphase transfer processes in waste rock piles producing acid mine drainage 1: Conceptual model and system characterization. J. Contam. Hydrol. 52:165-186.

Lefebvre, R., Hockley, D., Smolensky, J. and Lamontagne, A. 2001b. Multiphase transfer processes in waste rock piles producing acid mine drainage 2: Application of numerical simulation. J. Contam. Hydrol. 52:137-164.

Molson, J.W., Fala, O., Aubertin, M., Bussière, B. 2005. Numerical simulations of sulphide oxidation, geochemical speciation and acid mine drainage in unsaturated waste rock piles. J. Contam. Hydrol. 78 (4): 343–371.

Montero, I. C., Brimhall, G. H., Alpers, C. N., Swayze, G. A. 2005. Characterization of waste rock associated with acid drainage at the Penn Mine, California, by ground-based visible to short- wave infrared reflectance spectroscopy assisted by digital mapping. Chem. Geol. 215: 453–472.

Mora, C. F., Kwan, A. K. H., Chan, H. C. 1998. Particle size distribution analysis of coarse aggregate using digital image processing. Cem. Concr. Res. 28: 921–932.

Mora, C.F., Kwan, A.K.H. 2000. Sphericity, shape factor, and convexity measurement of coarse aggregate for concrete using digital image processing. Cem. Concr. Res. 30: 351–358.

Munroe, E.A., McLemore, V.T., Kyle, P., (1999). Waste rock pile characterization, heterogeneity, and geochemical anomalies in the Hillsboro Mining District, Sierra County,New Mexico. J. Geochem. Explor. 67 (1-3): 391-405

Neuner, M. 2009. Water flow through unsaturated mine waste rock in a region of permafrost. MSc Thesis, University of British Columbia, Vancouver, BC, Canada.

Ritchie, A.I.M. 1994. Sulfide oxidation mechanisms: controls and rates of oxygen transport. In: Jambor, J.L., Blowes, D.W. (Eds.), Environmental Geochemistry of Sulfide Mine-wastes. Mineralogical Association of Canada, Short Course Handbook Vol. 22, pp. 201–245.

Ritchie, A.I.M. and Miskelly, P. 2000. Geometric and physico-chemical properties determining sulfide oxidation rates in waste rock dumps. p. 277--287. In Proceeding Fifth International Conference on Acid Rock Drainage, ICARD-2000. Denver, Colorado. May 21-24, 2000. Society for Mining, Metallurgy, and Exploration Inc., Littleton, Colorado, USA.

Ritchie, A.I.M. 2003. Oxidation and gas transport in piles of sulfidic material (Chapter 4). In: Jambor, J.L., Blowes, D.W., Ritchie, A.I.M. (Eds.), Environmental Aspects of Mine Wastes, Short Course, vol. 31. Mineralogical Association of Canada, pp. 73–94.

Osher, S.J. Fedkiw, R.P. 2002. Level Set Methods and Dynamic Implicit Surfaces. Springer-Verlag. ISBN 0-387-95482-1.

Smith, L.J.D. 2009. Building and characterizing low sulfide instrumented waste rock piles: Pile design and construction, particle size and sulfur characterization, and initial geochemical response. MSc Thesis, University of Waterloo, Waterloo, ON, Canada.

Sracek, O., Choquette, M., Gélinas, P., Lefebvre, R., Nicholson, R.V. 2004. Geochemical characterization of acid mine drainage from a waste rock pile, Mine Doyon, Québec, Canada. J. Contam. Hydrol. 69(1-2), pp. 45-71.

Stockwell, J., Smith, L., Jambor, J. L., and Beckie, R. 2006. The relationship between fluid flow and mineral weathering in heterogeneous unsaturated porous media: A physical and geochemical characterization of a waste-rock pile. Appl. Geochem., 21(8): 1347–1361.

Stromberg, B., Banwart, S. 1999. Experimental study of acidity-consuming processes in mining waste rock: some influences of mineralogy and particle size. Appl. Geochem. 14: 1-16.

Tran, A.B., Miller, S., Williams, D.J., Fines, P., Wilson, G.W. 2003. Geochemical and mineralogical characterisation of two contrasting waste rock dumps – the INAP waste rock dump characterisation project. In: 6th International Conference on Acid Rock Drainage. Austral. Inst. Mining Metall. Publ. Ser. No. 3/2003, pp. 939–948.

Udden, J.A. 1914. Mechanical composition of clastic sediments. Bull. Geol. Soc. Am. 25: 655–744.

Wacker, A.G. 1969. A cluster approach to finding spatial boundaries in multispectral imagery, Laboratory for Applications of Remote Sensing Information Note 122969, Purdue University.

Wentworth, C.K. 1922. A scale of grade and class terms for clastic sediments. J. Geology. 30: 377–392.

Zucker, S.W. 1976. Region-growing: childhood and adolescence, Comput. Graphics Image Process. 5: 382-399.

Chapter 3

Amos, R.T., Blowes, D.W., Smith, L., Sego, D.C. 2009a. Measurement of wind induced pressure gradients in a waste rock pile. Vadose Zone J. 8: 953-962.

Amos, R.T., Smith, L., Neuner, M., Gupton, M., Blowes, D.W., Smith, L., Sego, D.C. 2009b. Diavik Waste Rock Project: Oxygen Transport in Covered and Uncovered Piles.

Proceedings of Securing the Future and 8th ICARD, June 22-26, 2009, Skellefteå, Sweden.

Anne, R.D. and Pantelis, G. 1997. Coupled natural convection and atmospheric wind forced advection in above ground reacting hexaps. p. 453-458. In International Conference on Computational Fluid Dynamics in Mineral and Metal Processing and Power Generation. Melbourne, Australia. 3-4 July, 1997. CSIRO, Australia.

Auer, L.H., Rosenberg, N.D., Birdsell, K.H. and Whitney, E.M. 1996. The effects of barometric pumping on contaminant transport. J. Contam. Hydrol. 24:145–166.

Bennett, J.W., Garvie, A.M., Pantelis, G., Ritchie, A.I.M., Bell, A.V., Noel, M. 1995. Comparison of measured and predicted transport processes controlling oxidation in the waste rock piles at the health steel mine site. p. 1017-1026. In T.P. Hynes and M.C. Blanchette (eds.), Sudbury ’95, Conference on mining and the environment. Sudbury, Ontraio, Canada. May 28 – June 1, 1995. CANMET, Ottawa.

Cathles, L.M., Apps, J.A. 1975. A model of dump leaching that incorporates oxygen balance, heat balance, and air convection, Metall. Trans. B 6: 617–624.

Chi, X. Waste-rock image grain-size analysis using digital image processing. Chapter 2 of this thesis.

Cooley, J.W. and Tukey, J.W. 1965. An Algorithm for the Machine Computation of the Complex Fourier Series. Math. Comput. 19: 297-301.

Howell, D.C. 2004. Fundamental Statistics for Behavioral Sciences. Thomson Wadsworth, Belmont, CA, USA

Garvie, A.M., Bennett, J.W., Ritchie, A.I.M. 1997. Quantifying the Spatial Dependence of the Sulfide Oxidation Rate in a Waste Rock Dump at Mt. Lyell, Tasmania. p. 333-349. In Proceedings of the Fourth International Conference on Acid Rock Drainage. Vancouver, British Columbia, Canada. May 30-June 6, 1997.

Holman, J.P. 2002. Heat transfer, McGraw-Hill, New York.

Lefebvre, R., Hockley, D., Smolensky, J. and Gélinas, P. 2001a. Multiphase transfer processes in waste rock piles producing acid mine drainage 1: Conceptual model and system characterization. J. Contam. Hydrol. 52:165-186.

Lefebvre, R., Hockley, D., Smolensky, J. and Lamontagne, A. 2001b. Multiphase transfer processes in waste rock piles producing acid mine drainage 2: Application of numerical simulation. J. Contam. Hydrol. 52:137-164.

Lu, N., and Y. Zhang. 1997. Thermally induced gas convection in mine wastes, International Journal of Heat and Mass Transfer, 40(11): 2621-2636.

Neuner, M., Gupton, M., Smith, L., Smith, L., Blowes, D.W., Sego, D.C. 2009. Diavik Waste Rock Project: Unsaturated Water Flow. Proceedings of Securing the Future and 8th ICARD, June 22-26, 2009, Skellefteå, Sweden.

Pantelis, G., Ritchie, A.I.M. 1992. Rate limiting factors in dump leaching of pyritic ores, Appl. Math. Modell. 16:553–560.

Pham, N., Sego, D.C., Arenson, L.U., Smith, L., Gupton, M., Neuner, M., Amos, R.T., Blowes, D.W., Smith, L. 2009. Diavik Waste Rock Project: Heat Transfer in a Permafrost Region. Proceedings of Securing the Future and 8th ICARD, June 22-26, 2009, Skellefteå, Sweden.

Press, W., Teukolsky, S, Vetterling, W., Flannery, B. 1992. Numerical Recipes in C. Cambridge University Press.

Ritchie, A.I.M. 1994. Sulfide oxidation mechanisms: controls and rates of oxygen transport. In: Jambor, J.L., Blowes, D.W. (Eds.), Environmental Geochemistry of Sulfide Mine-wastes. Mineralogical Association of Canada, Short Course Handbook Vol. 22, pp. 201–245.

Ritchie, A.I.M. and Miskelly, P. 2000. Geometric and physico-chemical properties determining sulfide oxidation rates in waste rock dumps. pp. 277-287. In Proceeding Fifth International Conference on Acid Rock Drainage, ICARD-2000. Denver, Colorado. May 21-24, 2000. Society for Mining, Metallurgy, and Exploration Inc., Littleton, Colorado, USA.

Smith, L., Moore, M., Bailey, B.L., Neuner, M., Gupton, M., Blowes, D.W., Smith, L., Sego, D.C. 2009. Diavik Waste Rock Project: From the Laboratory to the Canadian Arctic. Proceedings of Securing the Future and 8th ICARD, June 22-26, 2009, Skellefteå, Sweden.

Appendix A

The appendix includes grain size analysis results for five faces.

Photograph of the face
Grain size distribution
d50 contour

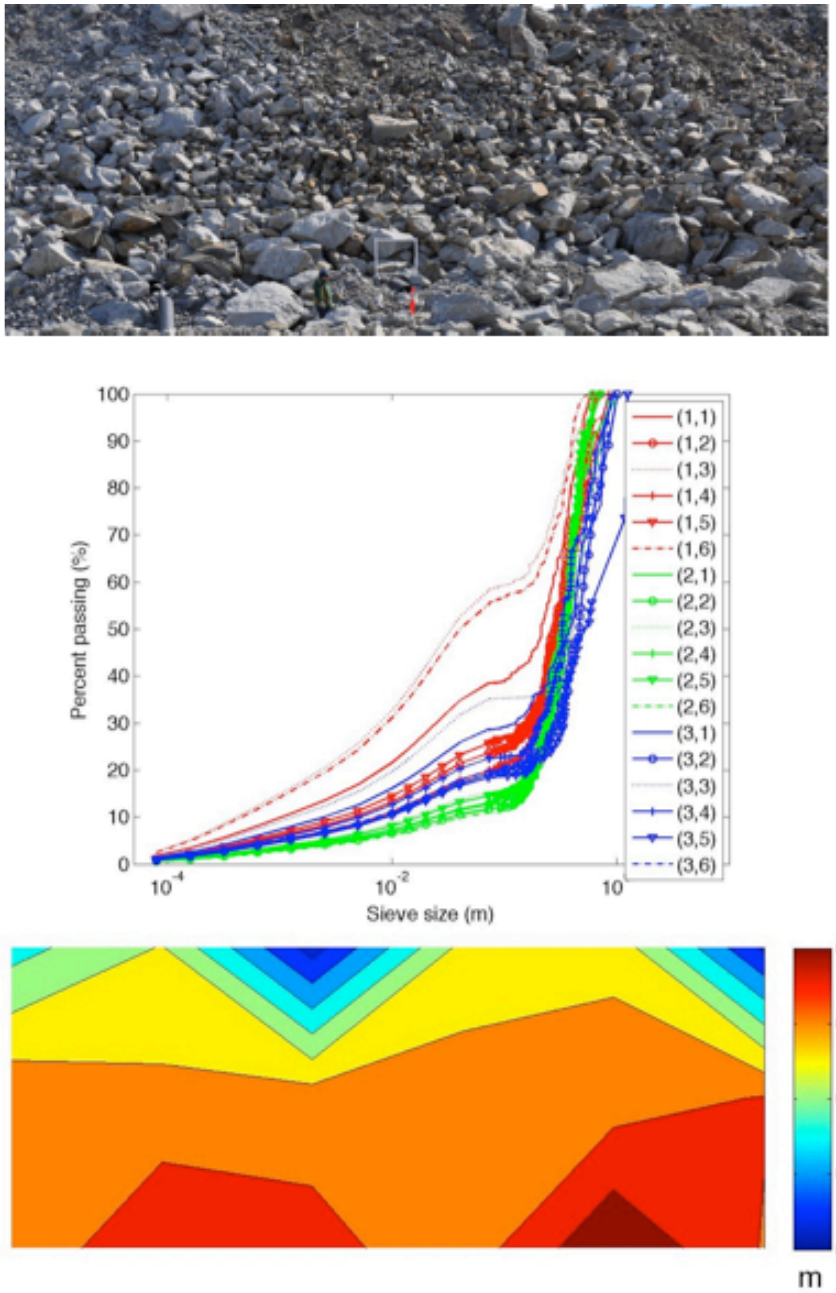

Figure A 1: TIW.

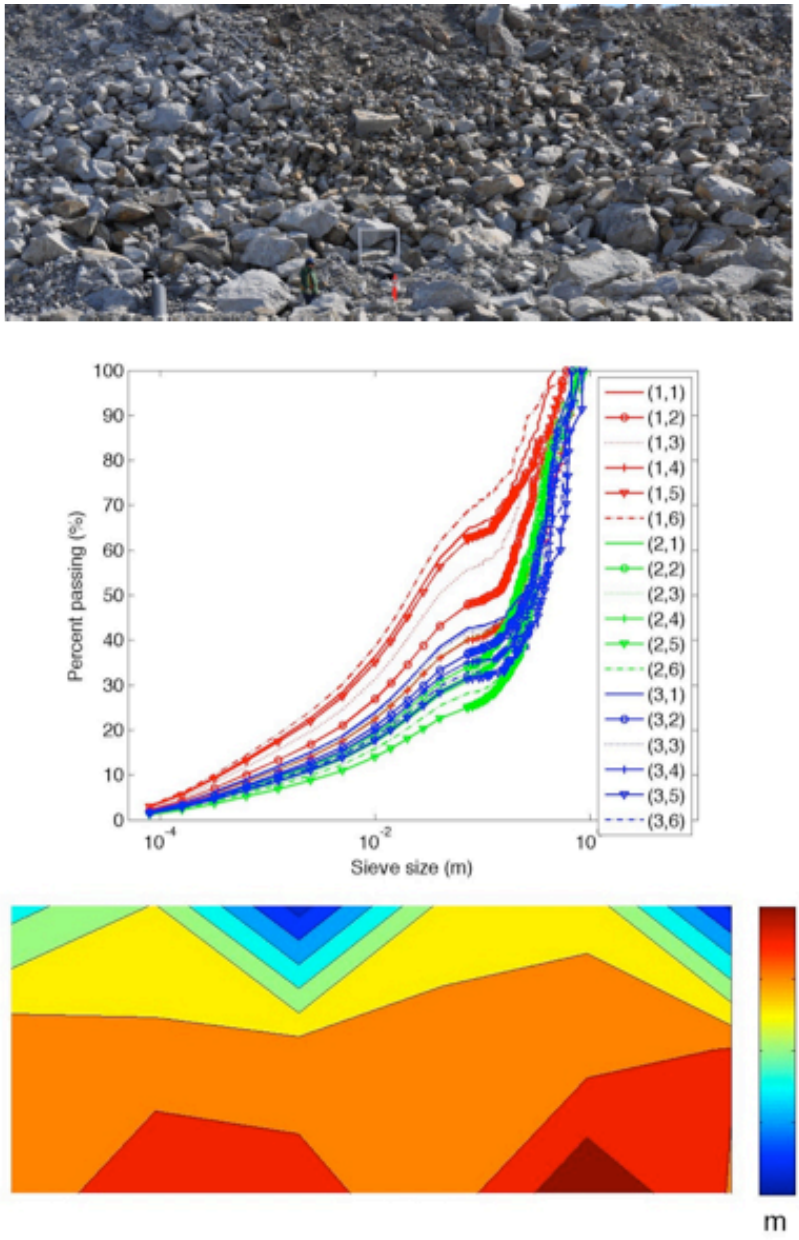

Figure A 2: TIE.

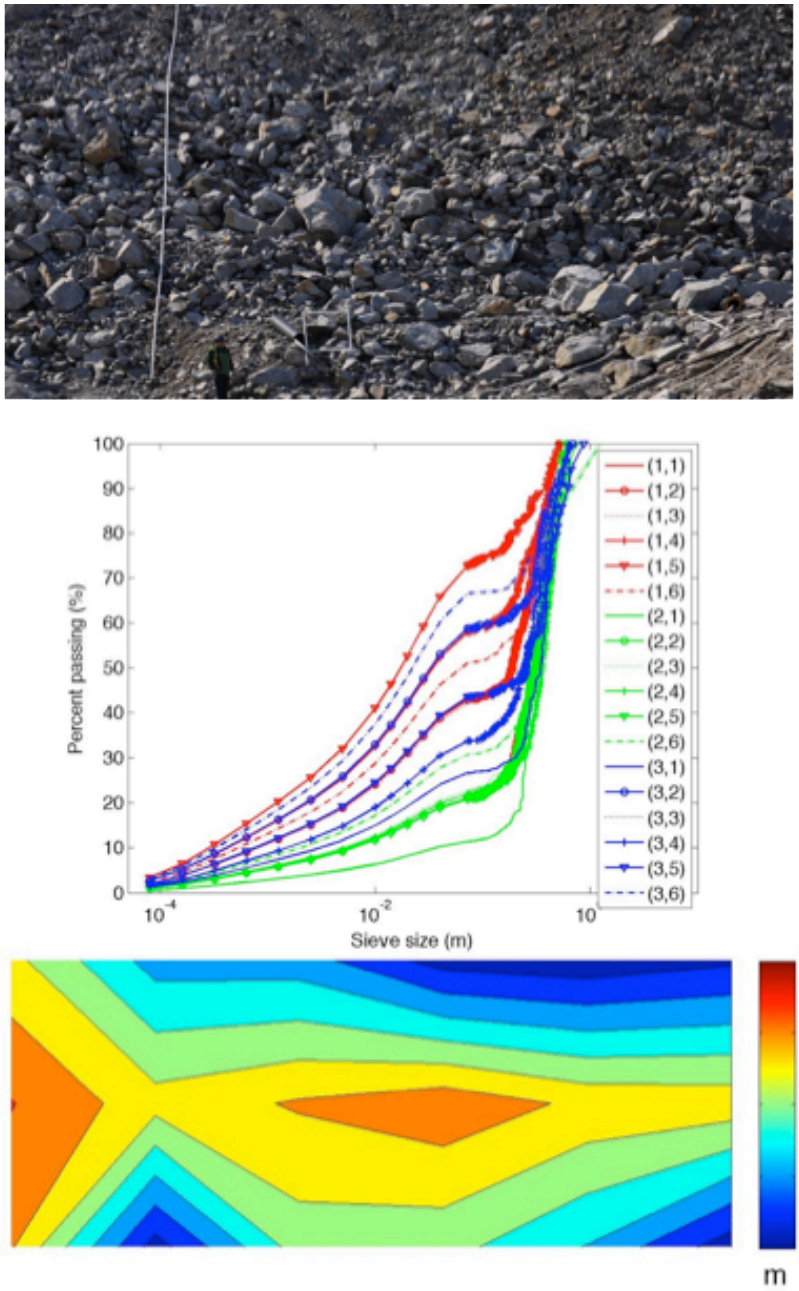

Figure A 3: TIIIN

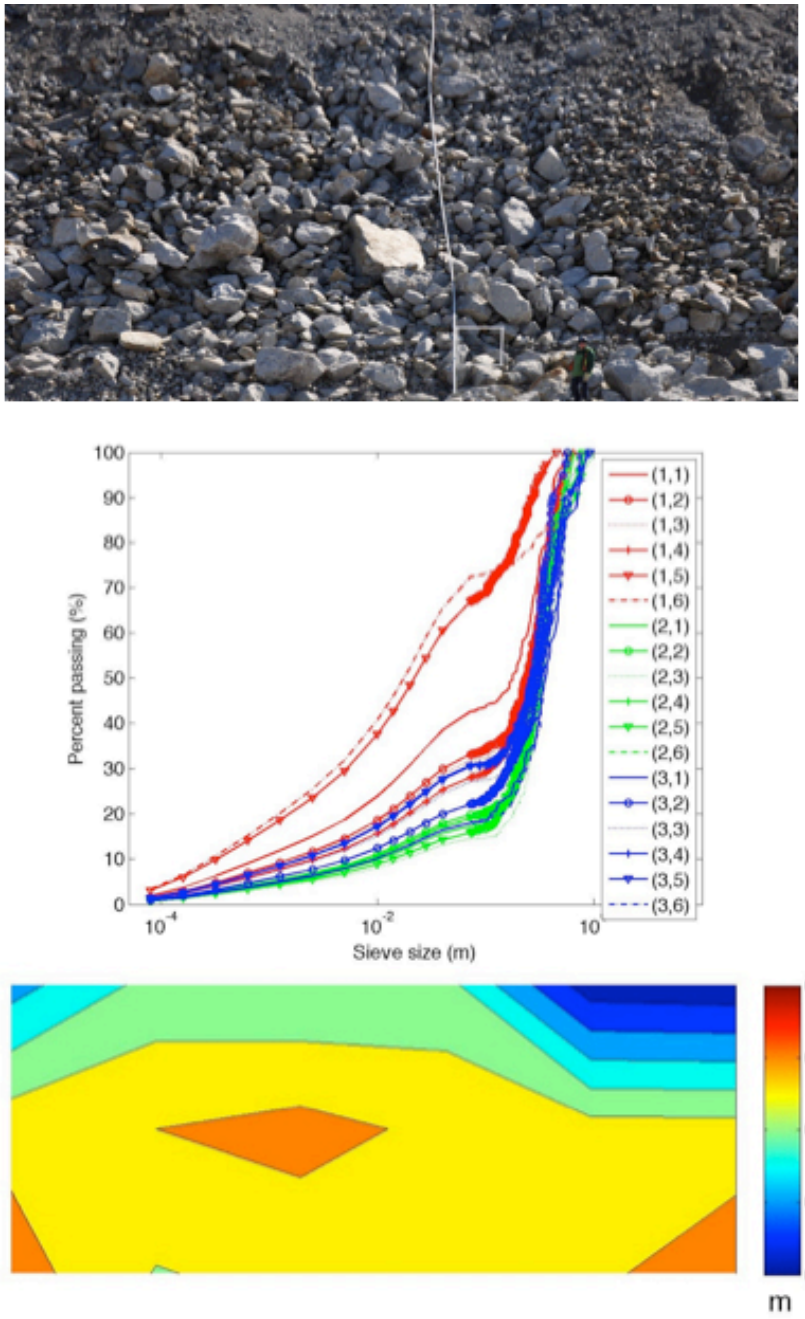

Figure A 4: TIIIW

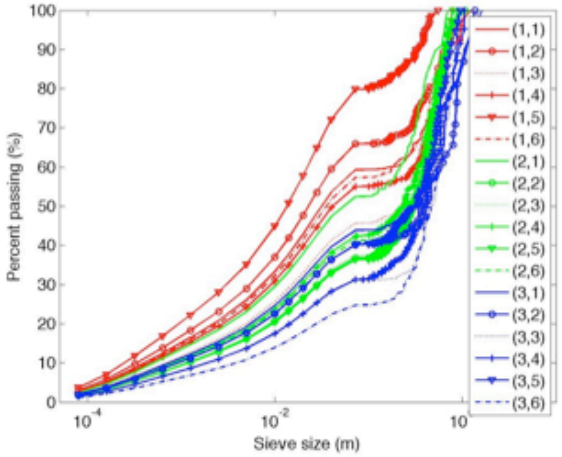

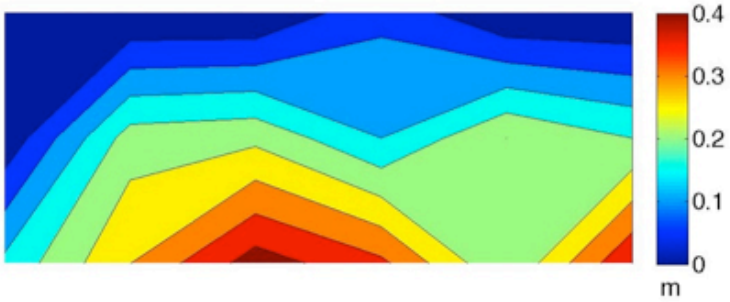

Figure A 5: TIIIS. Note that this photo has lower resolution than the others.

Appendix B

This section includes the Matlab code used to implement the region-growing based image grain-size analysis method in Chapter 2. The code was built under Matlab 2008a with digital image processing toolbox. Below is a brief description of the m-files. The user can refer to the comments in the m-files for more detailed functions of each file.

M-files include:

interface.m: user interface.

flood_fill_square.m: the main region-growing algorithm.

check_kernal.m: part of flood_fill_square.m.. It checks whether the pixel is the boundary of a region.

Overlay.m: overlay a green mask to show each step of region-growing. Memory consuming. Turn off unless for demonstration.

stats.m: moments calculations.

surface_area: surface area and mass distribution calculations.

select_bins: put grain-size analysis results into bins in Udden-Wentworth scale.

kc.m: Kozeny-Carmen permeability calculations.

larger_bins: surface area plotting.

thesis_figures: results visualization.

flood_fill_square.m

```
close all

% define intensity range of fine grains
if fine~=0
    f(f<fine)=60;
end

f = double( f(:,:,1) );
[fm,fn]=size(f);
f_orig = f;

%% get coordinates from user input
imshow(f,[]);hold on
nrect = 1;
rect = ones(1,4);% dummy first row
while waitforbuttonpress ==0 % if no button is pressed
    new_rect = getrect;

    % make sure rectangle falls inside image
    if new_rect(1) + new_rect(3) - fn >=0
        new_rect(3) = fn - new_rect(1)-2;
    end
    if new_rect(1) <= 0
        new_rect(1) = 2;
    end
    if new_rect(2) + new_rect(4) - fm >0
        new_rect(4) = fm - new_rect(2)-2;
    end
    if new_rect(2) <= 0
```

```
        new_rect(2) = 2;
    end

    plot(new_rect(1),new_rect(2),'ro');
    rect = [rect;new_rect]; % cat new coordinates to rect
    nrect = nrect + 1;

end

% round coordinates to intergers otherwise MATLAB will crash
rect = round(rect);
if size(rect) == [1 4]
    error('No seed points assigned');
end
rect = rect(2:end,:);
[m n] = size(rect);

%% edge enchancement
h = fspecial('sobel');
ff = imfilter(f,h+h','replicate');
% overlay filtered on original
% (This step is very important)
f = ff+f;

%% main flood fill program

% pre-allocate space for mask
mask = zeros(size(f));
% start with seed squares
for ii = 1:m
```

```
    mask(rect(ii,2):rect(ii,2)+rect(ii,4),...
        rect(ii,1):rect(ii,1)+rect(ii,3)) = ii;
end
mask_outline = mask;

% close off boundaries
f(1,:) = max(f(:))+11;
f(end,:) = max(f(:))+11;
f(:,1)=max(f(:))+11;
f(:,end)=max(f(:))+11;



% pre-allocate space for mean
region_mean = ones(m,1);
for ii = 1:m
    region_mean(ii,1) = mean(f(mask==ii));
end
thresh = 50;
keep_going=1;
counter = 0;

% region growing starts
while keep_going    && counter<50

    keep_going = 0;
    for ii = 1:m
        % [rows cols] = find(mask==ii);
        [rows cols] = find(mask_outline==ii);
        %mask_outline = zeros(size(f));
        mask_outline(mask_outline==ii) = 0;
```

```
% expand in 8 directions

for n = 1:length(rows)


   r = rows(n);
   c = cols(n);
   if check_kernal(r,c,rect(ii,:)) == 0

      % Up
      if abs(f(r-1,c)-region_mean(ii))<thresh && mask(r-1,c)==0
         mask(r-1,c) = ii; mask_outline(r-1,c) = ii;
         keep_going = 1;
      end

      % Down
      if abs(f(r+1,c)-region_mean(ii))<thresh && mask(r+1,c)==0
         mask(r+1,c) = ii;mask_outline(r+1,c) = ii;
         keep_going = 1;
      end

      % Left
      if abs(f(r,c-1)-region_mean(ii))<thresh && mask(r,c-1)==0
         mask(r,c-1) = ii;mask_outline(r,c-1) = ii;
         keep_going = 1;
      end

      % Right
      if abs(f(r,c+1)-region_mean(ii))<thresh && mask(r,c+1)==0
```

```
   mask(r,c+1) = ii;mask_outline(r,c+1) = ii;
   keep_going = 1;
end

% Up Left
if abs(f(r-1,c-1)-region_mean(ii))<thresh && mask(r-1,c-1)==0
   mask(r-1,c-1) = ii;mask_outline(r-1,c-1) = ii;
   keep_going = 1;
end

% Down Left
if abs(f(r+1,c-1)-region_mean(ii))<thresh && mask(r+1,c-1)==0
   mask(r+1,c-1) = ii;mask_outline(r+1,c-1) = ii;
   keep_going = 1;
end

% Up Right
if abs(f(r-1,c+1)-region_mean(ii))<thresh && mask(r-1,c+1)==0
   mask(r-1,c+1) = ii;mask_outline(r-1,c+1) = ii;
   keep_going = 1;
end

% Down Right
if abs(f(r+1,c+1)-region_mean(ii))<thresh && mask(r+1,c+1)==0
   mask(r+1,c+1) = ii;mask_outline(r+1,c+1) = ii;
   keep_going = 1;
end

seg = find(mask==ii);
region_mean(ii) = mean(f(seg));
```

```
        end % check_kernal


      end % end of for-loop
   end


   counter = counter + 1;
   %  Overlay(f_orig, mask); % uncomment this line to output to screen

end % end of while-loop

%% dilation
if fine == 0
   se = strel('disk',5);
   mask = imdilate(mask,se);
end
figure;imshow(mask,[])

%% grain size curve
diam = zeros(m,1);area_mask = zeros(m,1);
for ii = 1:m
   [rd cd] = find(mask==ii);
   if isempty(rd) || isempty(cd)
      rd =0;cd=0;
   end
   % min of two sides of rectangle
   diam(ii) = min(max(cd)-min(cd),max(rd)-min(rd));
   area_mask(ii) = length(find(mask==ii));
end
```

```
plotm = [diam,area_mask];
plotm = sortrows(plotm,1);% sort by diameters
plotm(:,2) = cumsum(plotm(:,2));% cumulatively sum colum 2

area_fine = fm*fn - plotm(end,2);
plotm(:,2) = plotm(:,2) + area_fine;

max(plotm(:))

%plotm(:,2) = plotm(:,2)/max(plotm(:));
plotm(:,2) = plotm(:,2)/(fm*fn); % convert to pecentage
```

check_kernal.m

```
function a = check_kernal(r,c,rect)

% a = 1 if (r,c) is in the kernal

if r-(rect(2)+1)>0 && r-(rect(2)+rect(4)-1)<0 ...
   && c-(rect(1)+1)>0 && c-(rect(1)+rect(3)-1)<0
   a = 1;
else
   a = 0;
end
```

interface.m

```
% This script is a interface that allows user to select images,
% assign seed regions, run region-growing algorithm and convert results
```

```
% to various formats for statistical analysis
%
% - run first cell to load and divide an image
% - run second cell to region-grow each sub-image
% - run third cell to convert all results to formats for statistics

% ask for user input
photo = input('Name of the photo, please?','s');

% load file
path_name = strcat('/Users/Sheldon/Desktop/Test Piles grain size photos/matlab/',photo,...
   '.jpg');
CO=imread(path_name);
% convert to gray scale
CO = double(CO(:,:,1));

% divide into sub-regions
if strcmp(photo,'T3W') == 1 || strcmp(photo,'T3N') == 1
   C = mat2cell(CO,[500 500 500],[500 500 500 500 500 500]);
elseif strcmp(photo,'T3S') == 1
   C = mat2cell(CO,[400 400 400],[300 300 300 300 300 300]);
elseif strcmp(photo,'T1E') == 1 || strcmp(photo,'T1W') == 1 ...
      || strcmp(photo,'T1N') == 1
   C = mat2cell(CO,[400 400 400],[500 500 500 500 500 500]);
else
   C = mat2cell(CO,[500 500 500 500],[500 500 500 500]);
end

% initialize a workspace to save outputs
work_space_name = strcat(photo,'.mat');
```

```
shit = 0;
if exist(work_space_name) == 0
   save(work_space_name,'shit')
end



%% Region-growing

%%%%%%%%%%%%%%%%%%%%%
% change these to run algorithm on different sub-regions
x = 3; y = 6;
%%%%%%%%%%%%%%%%%%%%%

% load a small region and run region growing
f=C{x,y};
fine = 0;
flood_fill_square

% save grain size curve in a vairable
name = strcat('c',int2str(x),int2str(y));% curve name
eval([name '=' 'plotm']);
% save variable in workspace
%save(work_space_name,name,'-append')

%}

%% attaching hand sample sieve analysis measurements
%  and prepare for statistics (run once after all region-growings are done)
%
```

```
% cxx: [diamter_in_pixels, %]
% cxxe: divided by reference [diameter_real, %] with Lianna's hand samples
% cxxlog: [-log2(diameter_real), %] with Lianna's hand samples
% cxxm: statistical moments

% TIII:[mm %]
TIII = [
   72.40      100.00
   40.00      90.36
   28.00      81.24
   20.00      72.33
   14.00      63.61
   10.00      56.24
   5.00       44.03
   2.50       35.16
   1.25       27.82
   0.63       21.04
   0.32       14.70
   0.16       8.88
   0.08       4.67];
% convert to m
TIII(:,1) = TIII(:,1)/1000;
TIII(:,2) = TIII(:,2)/100;

largest_grain = TIII(1,1);
% flip so in same order as image analysis
% [m %]
TIII = flipud(TIII);

load refs.mat
```

```
for ii = 1:6


   % load one group of curves
   reference = refs{ii,2};
   eval(['load ' char(refs(ii,1))])



   for i = 1:3
      for j = 1:6
         % divide by reference size
         % e.g.  c11e = [c11(:,1)/150 c11(:,2)]
         % 'e' for extended
         ce = num2str(['c' num2str(i) num2str(j) 'e']);
         c_col1_div_ref = num2str(['c' num2str(i) num2str(j) '(:,1)/'...
            num2str(reference)]);
         c_col2 = num2str(['c' num2str(i) num2str(j) '(:,2)']);
         eval([ce '=[' c_col1_div_ref ' ' c_col2  '];']);

         % truncate small sizes to attach lianna's
         % e.g.: c11e = c11e(c11e(:,1)>0.07,:)
         eval([ce '=' ce '(' ce '(:,1)>' num2str(largest_grain) ',:);']  );

         % attach lianna's
         min_percent = eval(['min(' 'c' num2str(i) num2str(j) 'e(:,2))'  ]);
         T_attach = [TIII(:,1),TIII(:,2)*min_percent];
         eval(['c' num2str(i) num2str(j) 'e=' ...
            '[T_attach;' 'c' num2str(i) num2str(j) 'e(2:end,:);];']);
```

```
% store log2 (phi)-scale data in  'cXXlog'
% e.g: c11log = [-log2(c11e(:,1)*1000), c11e(:,2)]
% NOTE: remember it's log2 and need to convert to mm by *1000
eval(['c' num2str(i) num2str(j) 'log=[' ...
    '-log2(' 'c' num2str(i) num2str(j) ...
    'e(:,1)*1000),c' num2str(i) num2str(j) 'e(:,2)];']);

% calculate surface area
% e.g. c11s = surface_area(c11e)
% c11s:
% [diam, mass_fraction, tot_surf, tot_surf./mass_fraction];
eval(['c' num2str(i) num2str(j) 's=surface_area(' ...
    'c' num2str(i) num2str(j) ...
    'e);' ]);

% calculate mass distribution with larger bins
% e.g. c11b = surface_area(c11b)
% c11s:
% [diam, mass_fraction, tot_surf, tot_surf./mass_fraction];
eval(['c' num2str(i) num2str(j) 'b=larger_bins(' ...
    'c' num2str(i) num2str(j) ...
    's);' ]);


% calculate moments
% 'select_bins' first to convert to phi-scale
% e.g. c11m = stats(select_bins(c11log));
eval(['c' num2str(i) num2str(j) 'm=stats(select_bins(' ...
    'c' num2str(i) num2str(j) ...
```

```
            'log));' ]);

        % save in workspace
        % e.g: save('T1E.mat',c36e, '-append' )
        eval(['save('"  char(refs(ii,1)) '.mat'"...
          ', "c' num2str(i) num2str(j)...
          'e","c' num2str(i) num2str(j)...
          'log", "c' num2str(i) num2str(j)...
          's","c' num2str(i) num2str(j)...
          'm","-append" )']);


      end
    end

  end
```

stats.m

```
  function gstats = stats(cxxlog)
  % calculates moments using GRAISTAT.pdf page 5
  % Manual of sedimentary petrology, 1983, available at DC
  % 'g' for grain size

  m_phi = cxxlog(:,1);
  f = cxxlog(:,2)*100;
  f_shift = [0; f(1:end-1)];
  f = f-f_shift; % convert to non-cum
```

```
    plot(m_phi,f,'.')

    gmean = sum(f.*m_phi)/100;

    gstd = sqrt(sum(f.*(m_phi-gmean).^2)/100);

    gskew = sum(f.*(m_phi-gmean).^3)/100/gstd^3;

    gkur = sum(f.*(m_phi-gmean).^4)/100/gstd^4;

gstats = [gmean gstd gskew gkur];
```

Overlay.m

```
    function Overlay(f, mask)

        m = max(f(:));
        fr = f;
        fg = f + mask / max(mask(:)) * m/2;
        fb = f;

        imshow(reshape([fr fg fb],[size(f,1) size(f,2) 3])/m, []);


    drawnow;
```

select_bins.m

```
    function bins = select_bins(cxx)
    % convert to 'phi'-scale
    % Manual of sedimentary petrology, 1983, available at DC
```

```
diam = cxx(:,1);
perc = cxx(:,2);

perc_shift = [0; perc(1:end-1)];
perc = perc -perc_shift;% convert to non-cum

%plot(diam, perc)
% [-9 -7 -5 -3 -1 1 3]

%
n_9 = perc(diam<-8 & diam >-10);
%perc_9 = max(n_9)-min(n_9)
perc_9 = sum(n_9);
if isempty(perc_9)==1
   perc_9 = 0;
end

n_7 = perc(diam<-6 & diam >-8);
%perc_7 = max(n_7)-min(n_7)
perc_7 = sum(n_7);
if isempty(perc_7)==1
   perc_7 = 0;
end

n_5 = perc(diam<-4 & diam >-6);
%perc_5 = max(n_5)-min(n_5)
perc_5 = sum(n_5);
if isempty(perc_5)==1
   perc_5 = 0;
end
```

```
n_3 = perc(diam<-2 & diam >-4);
%perc_3 = max(n_3)-min(n_3)
perc_3 = sum(n_3);
if isempty(perc_3)==1
   perc_3 = 0;
end

n_1 = perc(diam<0 & diam >-2);
perc_1 = sum(n_1);
if isempty(perc_1)==1
   perc_1 = 0;
end

p_1 = perc(diam<2 & diam >0);
%perc_p_1 = max(p_1)-min(p_1)
perc_p_1 = sum(p_1);
if isempty(perc_p_1)==1
   perc_p_1 = 0;
end

p_3 = perc(diam<4 & diam >2);
%perc_p_3 = max(p_3)-min(p_3)
perc_p_3 = sum(p_3);
if isempty(perc_p_3)==1
   perc_p_3 = 0;
end


bins = [perc_9 perc_7 perc_5 perc_3 perc_1 perc_p_1 perc_p_3];
```

```
   bins = [-9 -7 -5 -3 -1 1 3;bins]';
   plot(bins(:,1),bins(:,2),'o-')
%}


surface_area.m
   function garea = surface_area (cxxe)
   % This function calculates surface area and mass distrbution of each
   % grain size fraction
   % input: cxxe as in interface.m, the extended and di-referenced grain size
   %        distribution
   % output: described below

   diam = cxxe(:,1); % diameter
   perc = cxxe(:,2); % percentage
   density = 2650;% kg/m3
   mass_tot = 1;% total mass of sample is 1kg

   % conver to non-cumulative
   perc_shift = [0; perc(1:end-1)];
   perc = perc -perc_shift;% convert to non-cum

   plot(perc) % just to check

   mass_fraction = mass_tot*perc;% mass for each fraction
   gvol = pi/6*diam.^3; % ideal particle volume
   gmass = gvol*density; % ideal particle mass
   num_grain = mass_fraction./gmass; % number of particles of each fraction
   surf_each = 4*pi*(diam/2).^2;% ideal surface area
   tot_surf = surf_each.*num_grain;% surface area for each fraction
```

```
   % [diamter, mass of each fraction, total surface area, rario of mass and
   % surface area]
garea = [diam, mass_fraction, tot_surf, tot_surf./mass_fraction];
```

larger_bins.m

```
   function cxxb = larger_bins(cxxs)
   % put image results in larger bins so that no disconnect in mass figure
   % cxxb b for bins
   cxxb = cxxs(1:13,1:2);
   cxxb = [cxxb;0.2 sum(cxxs(cxxs(:,1)>0.0724 & cxxs(:,1)<0.2,2))];

   cxxb = [cxxb;0.3 sum(cxxs(cxxs(:,1)>0.2 & cxxs(:,1)<0.3,2))];
   cxxb = [cxxb;0.4 sum(cxxs(cxxs(:,1)>0.3 & cxxs(:,1)<0.4,2))];
   cxxb = [cxxb;0.5 sum(cxxs(cxxs(:,1)>0.4 & cxxs(:,1)<0.5,2))];
   cxxb = [cxxb;0.6 sum(cxxs(cxxs(:,1)>0.5 & cxxs(:,1)<0.6,2))];
   cxxb = [cxxb;0.7 sum(cxxs(cxxs(:,1)>0.6 & cxxs(:,1)<0.7,2))];
   cxxb = [cxxb;0.9 sum(cxxs(cxxs(:,1)>0.7 & cxxs(:,1)<0.8,2))];
   cxxb = [cxxb;0.9 sum(cxxs(cxxs(:,1)>0.8 & cxxs(:,1)<0.9,2))];
   cxxb = [cxxb;1 sum(cxxs(cxxs(:,1)>0.9 & cxxs(:,1)<1,2))];
   cxxb = [cxxb;1.1 sum(cxxs(cxxs(:,1)>1 & cxxs(:,1)<1.1,2))];
   cxxb = [cxxb;1.2 sum(cxxs(cxxs(:,1)>1.1 & cxxs(:,1)<1.2,2))];
```

kc.m

```
   function permeability = kc(d10)
   % Koseny-Carmen permeability
   n = 0.23;
   rho = 1000;% kg/m3
   g = 9.8;% m/s2
```

```
    mu = 1e-5;% Ns/m5
    Ck = 8.3e-3;

    fn = n^3/(1-n)^2;

permeability = rho*g/mu*Ck*fn*d10^2*mu/rho/g;

thesis_figures.m
    %% dilation
    dil_test = zeros(50,50);dil_holes = zeros(50,50);

    dil_holes(10:40,10:40) = 1;
    dil_test = zeros(10,10);dil_test(4:6,4:6)=1;dil_test(3,4)=1;dil_test(6,7)=1;

    for ii = 1:20
        dil_holes(ceil(10+30*rand),ceil(10+30*rand)) = 0;
    end



    se = strel('diamond',3);
    se = strel('rectangle',[3 3]);
    dil = imdilate(dil_test,se);dilh = imdilate(dil_holes,se);

    %%
    dil(4:6,4:6)=0.5;dil(3,4)=0.5;dil(6,7)=0.5;
    subplot(121);pcolor(dil_test);title('Original','FontSize',15)
    axis equal;axis([1 10 1 10]);set(gca,'Xtick',[],'Ytick',[])
    subplot(122);pcolor(dil);title('Dilated','FontSize',15)

    axis equal;axis([1 10 1 10]);set(gca,'Xtick',[],'Ytick',[])
```

```
saveas(gcf,'/Users/Sheldon/Desktop/grain size plots/dilation.jpg')


%% dilate to fill holes
subplot(121);imshow(dil_holes,[]);title('Original','FontSize',15)
subplot(122);imshow(dilh,[]);title('Dilated','FontSize',15)
saveas(gcf,'/Users/Sheldon/Desktop/grain size plots/dilation_holes.jpg')

%%
dem = imread('demostration_pic.jpg');
rg = imread('region_growing.jpg');
rd = imread('region_dilated.jpg');
gsc = imread('curve.jpg');
subplot(221);imshow(dem,[]);title('Original image')
subplot(222);imshow(rg,[]);title('Region growing')
subplot(223);imshow(rd,[]);title('Segmentation')
subplot(224);imshow(gsc,[]);title('Grain size curve')
saveas(gcf,'/Users/Sheldon/Desktop/grain size plots/flow.jpg')

%% reproducibility
% T3F2 c43
%load reprod.mat
%load reproMultiUsers.mat
clf
%
minl = 31;
run_avg = ones(minl,1);run_std = ones(minl,1);
for ii = 1:minl
   run_avg(ii) = mean([run1(length(run1)+ii-minl,2),run2(length(run2)+ii-minl,2),...
      run3(length(run3)+ii-minl,2), run4(length(run4)+ii-minl,2),...
```

```
        run5(length(run5)+ii-minl,2), run6(length(run6)+ii-minl,2),...
        run10(length(run10)+ii-minl,2), run9(length(run6)+ii-minl,2),...
        run8(length(run8)+ii-minl,2), run7(length(run7)+ii-minl,2),...
        ]);
    run_std(ii) = std([run1(length(run1)+ii-minl,2),run2(length(run2)+ii-minl,2),...
        run3(length(run3)+ii-minl,2), run4(length(run4)+ii-minl,2),...
        run5(length(run5)+ii-minl,2), run6(length(run6)+ii-minl,2),...
        run10(length(run10)+ii-minl,2), run9(length(run6)+ii-minl,2),...
        run8(length(run8)+ii-minl,2), run7(length(run7)+ii-minl,2),...
        ]);
end
%}

semilogx(run1(:,1)/70,run1(:,2)*100,'.-',run2(:,1)/70,run2(:,2)*100,'o-'...
    ,run3(:,1)/70,run3(:,2)*100,'+-',run4(:,1)/70,run4(:,2)*100,'*-',...
    run5(:,1)/70,run5(:,2)*100,'--',run6(:,1)/70,run6(:,2)*100,'d-',...
    run7(:,1)/70,run7(:,2)*100,'x-',run8(:,1)/70,run8(:,2)*100,':',...
    run9(:,1)/70,run9(:,2)*100,'v-',run10(:,1)/70,run10(:,2)*100,'s-')
hold on
semilogx(run6(:,1)/70,run_avg*100,'y^-','LineWidth',2)
semilogx(run6(:,1)/70,90*(run_avg),'m^-','LineWidth',1.5)
semilogx(run6(:,1)/70,110*(run_avg),'g^-','LineWidth',1.5)
legend('Run1','Run2','Run3','Run4','Run5',...
    'Run6','Run7','Run8','Run9','Run10','Mean','Mean - 10%',...
    'Mean + 10%','Location','Northwest')
xlabel('Sieve size (m)');ylabel('% Passing')

axis([0.1 2.5 0  100])

saveas(gcf,'/Users/Sheldon/Desktop/grain size plots/reproducbility.jpg')
```

```
%% Curves

close all
% reference info stored in refs.mat
load refs.mat
cName = 'T1E';ref = 0;
% extract reference length
for ii = 1:6
   str1 = refs{ii,1};
   if strcmp(cName, str1)==1
      ref = refs{ii,2};
   end
end
if strcmp(cName,'T1E')
   ref = 130;
end

disp(cName);disp(ref)
if ref == 0
   error('Reference not found')
end

eval(['load ' cName '.mat']);
set(0,'defaultaxesfontsize',15);
set(0,'defaultlinelinewidth',1.5);

%%%%%%%% normal x

load refs.mat
```

```
color = {'r','g','b'};sty = {'-','-o',':','-+','-v','-.'};

for ii = 1:3
   for j = 1:6
      px = strcat('c',int2str(ii),int2str(j), 'e' ); % 'e' for extended
      eval(['plot(' px '(:,1)' ',' px '(:,2)*100' ','...
         "" color{ii} sty{j} "" ')'])
      hold on
   end
end

%saveas(gcf,'/Users/Sheldon/Desktop/grain size plots/cT1E.jpg')

%axis([0.01 10 0 100])
%legend('11','12','13','14','21','22','23','24','31','32','33','34','41','42','43','44')
legend('11','12','13','14','15','16','21','22','23','24','25','26','31','32','33','34','35','36')
xlabel('Sieve size (m)');
ylabel('Percent passing (%)')
set(gcf,'color','w');
eval(['saveas(gcf,"/Users/Sheldon/Desktop/grain size plots/', 'c',cName,'.jpg")']);

%%%%%%% log-x

figure
for ii = 1:3
   for j = 1:6
      px = strcat('c',int2str(ii),int2str(j),'e');
      eval(['semilogx(' px '(:,1)' ',' px '(:,2)*100' ','...
         "" color{ii} sty{j} "" ')'])
```

```
        hold on
    end
end

axis([1e-5*5 10 0 100])
%legend('11','12','13','14','21','22','23','24','31','32','33','34','41','42','43','44')
legend('(1,1)','(1,2)','(1,3)','(1,4)','(1,5)','(1,6)',...
    '(2,1)','(2,2)','(2,3)','(2,4)','(2,5)','(2,6)','(3,1)','(3,2)','(3,3)','(3,4)','(3,5)','(3,6)')
ylabel('Percent passing (%)')
xlabel('Sieve size (m)');

set(gcf,'color','w');
eval(['saveas(gcf,"/Users/Sheldon/Desktop/grain size plots/', 'c',cName,'log.jpg")']);
%saveas(gcf,'/Users/Sheldon/Desktop/grain size plots/cT1Elog.jpg')
%%
close all
perm =1;
d50_mean = ones(1,6);d10_mean = ones(1,6);row_mean = zeros(1,3);
row_mean = zeros(6,3);
for k = 1:6
    figure
    clf
    % loop thru faces
    load refs.mat
    eval(['load ' char(refs(k,1))])
    cName = char(refs(k,1));
    pp = ones(3,6); pp10 = ones(3,6);%permeability = ones(3,6);
    for ii = 1:3
        for j = 1:6
            % load extended, ./referenced data
```

```
        px = strcat('c',int2str(ii),int2str(j),'e');
        % find d50
        px1 = eval([px '(:,1)']);px2 = eval([px '(:,2)']);
        % d50
        eval(['fiftyp=px1' '(round(' 'px2'  '*10)/10==0.5);']);

        % d10 for Hazen permeability
        eval(['tenp=px1' '(round(' 'px2'  '*10)/10==0.1);']);
        if isempty(fiftyp) == 0
           pp(ii,j) = fiftyp(1) ;
        else
           pp(ii,j) = 0;
        end
        if isempty(tenp) == 0
           pp10(ii,j) = tenp(1) ;
        else
           pp10(ii,j) = 0;
        end
        permeability(ii,j) = kc(pp10(ii,j));

        eval(['p', char(refs(k,1)) '(ii,j)=pp(ii,j);']);
        eval(['d10', char(refs(k,1)) '(ii,j)=pp10(ii,j);']);
      end
      row_mean(k,ii) = mean(permeability(ii,:));
   end

        disp('max')
        max(permeability(:))
disp('min')
min(permeability(:))
```

```
%


    if perm == 1
        contourf(flipud(log10(permeability)));colormap gray
    else
        contourf(flipud(pp10));colormap gray
    end
    colorbar
    h = colorbar;
    if perm == 0
        xlabel(h,'m');
    elseif perm == 1
        xlabel(h,'m^2');
    end
    set(h,'FontWeight','bold')
    axis equal;axis([1 6 1 3])

    if perm == 0
   %     caxis([0 0.4])
    else
        caxis([-12 -7])
    end

    set(gcf,'color','w');
    %title('d50 contour')
    axis off
%}

    d50_mean(k) = mean(pp(:));
```

```
    d10_mean(k) = mean(pp10(:));
    if perm == 0
 %      eval(['saveas(gcf,"/Users/Sheldon/Desktop/grain size plots/', cName,'.jpg")']);
    elseif perm ==1
       eval(['saveas(gcf,"/Users/Sheldon/Desktop/grain size plots/',
cName,'permeability.jpg")']);
    end


end

%over all, not used
d10meanT1 = mean(d10_mean(1:3));d10meanT3 = mean(d10_mean(4:6));
d50meanT1 = mean(d50_mean(1:3));d50meanT3 = mean(d50_mean(4:6));

% d10 mean
for k = 1:6
   eval(['Row' char(refs(k,1)) '=mean(d10' char(refs(k,1)) ',2);'])
end
RowT1 = (RowT1N+RowT1W+RowT1E)/3;
RowT3 = (RowT3W+RowT3N+RowT3S)/3;
%%
% veritcal gradient of d50
clf
set(0,'defaultlinelinewidth',2);
d50MeanT1E = ones(1,3);d50MeanT1N = ones(1,3);d50MeanT1W = ones(1,3);...
   d50MeanT3N = ones(1,3);d50MeanT3S = ones(1,3);d50MeanT3W = ones(1,3);
for ii = 1:3
   d50MeanT1E(ii) = mean(pT1E(ii,:));
   d50MeanT1N(ii) = mean(pT1N(ii,:));
   d50MeanT1W(ii) = mean(pT1W(ii,:));
   d50MeanT3N(ii) = mean(pT3N(ii,:));
```

```
    d50MeanT3S(ii) = mean(pT3S(ii,:));
    d50MeanT3W(ii) = mean(pT3W(ii,:));
end
height = 1:3;
plot(height,d50MeanT1E,'b-o',height,d50MeanT1N,'b--',height,d50MeanT1W,'b:',...
    height,d50MeanT3N,'r-o',height,d50MeanT3S,'r--', height,d50MeanT3W,'r:')


hold on

d50Mean = (d50MeanT1E + d50MeanT1N + d50MeanT1W +...
    d50MeanT3N + d50MeanT3S + d50MeanT3W)/6;
plot(height,d50Mean,'g--','LineWidth',6)
hold off
set(gca,'XTickLabel',{'Top';' ';''; '';'Bottom';})
xlabel('Pile position');ylabel('d50 (m)')
legv = legend('TIE','TIN','TIW','TIIIN','TIIIS','TIIIW','Mean','Location','SouthEast',...
    'Orientation','Horizontal');
set(legv,'FontSize',10)
eval(['saveas(gcf,"/Users/Sheldon/Desktop/grain size plots/vgradient.jpg")']);

%%
% horizontal gradient of d50
clf

d50MeanT1E = ones(1,6);d50MeanT1N = ones(1,6);d50MeanT1W = ones(1,6);...
    d50MeanT3N = ones(1,6);d50MeanT3S = ones(1,6);d50MeanT3W = ones(1,6);
for ii = 1:6
    d50MeanT1E(ii) = mean(pT1E(:,ii));
    d50MeanT1N(ii) = mean(pT1N(:,ii));
```

```
    d50MeanT1W(ii) = mean(pT1W(:,ii));
    d50MeanT3N(ii) = mean(pT3N(:,ii));
    d50MeanT3S(ii) = mean(pT3S(:,ii));
    d50MeanT3W(ii) = mean(pT3W(:,ii));
end
height = 1:6;
plot(height,d50MeanT1E,'b-o',height,d50MeanT1N,'b--',height,d50MeanT1W,'b:',...
    height,d50MeanT3N,'r-o',height,d50MeanT3S,'r--', height,d50MeanT3W,'r:')
hold on

d50Mean = (d50MeanT1E + d50MeanT1N + d50MeanT1W +...
    d50MeanT3N + d50MeanT3S + d50MeanT3W)/6;
plot(height,d50Mean,'g--','LineWidth',6)
hold off
set(gca,'XTickLabel',{'Left';' ';" ";";";";";";";";";'Right';})
xlabel('Pile position');ylabel('d50 (m)')

leg = legend('TIE','TIN','TIW','TIIIN','TIIIS','TIIIW','Mean','Location','SouthEast',...
    'Orientation','Horizontal');
set(leg,'FontSize',10)



eval(['saveas(gcf,"/Users/Sheldon/Desktop/grain size plots/hgradient.jpg")']);



%%
% compare lianna/stacey's measurements
clf
set(0,'defaultaxesfontsize',15);
set(0,'defaultlinelinewidth',1);
```

```
comp = 'T3W'; load refs.mat
eval(['load ' comp '.mat']);
load lia_plot.mat
%color = {'r','g','b'};sty = {'-','-o',':','-+','-v','-.'};
stacey = [406.4       0.865
   254         0.737
   152.4       0.525];

semilogx(c11e(:,1),c11e(:,2)*100,'k');hold on
%semilogx(lia_plot(:,1)/1000,lia_plot(:,2),'ko-','LineWidth',4)
semilogx(stacey(:,1)/1000,stacey(:,2)*100,'ko-','LineWidth',4)
%axis([0.01 10 0 100])
set(gcf, 'DefaultTextFontSize',30)
leg = legend('Image analysis','Sample','Location','Northwest');
set(leg,'FontSize',15)
for ii = 1:3
   for j = 1:6
      px = strcat('c',int2str(ii),int2str(j),'e');
      eval(['semilogx(' px '(:,1)' ',' px '(:,2)*100' ","k"'...
         ","HandleVisibility","off")']);% dont show in legend
      %   "" color{ii} sty{j} "" ')'])
      hold on
   end
end

%eval(['text(10e-5, 50,'"  comp  "')'])
%legend('11','12','13','14','15','16','21','22','23','24','25','26','31','32','33','34','35','36','Sample',
'Location','Best')
ylabel('Percent passing (%)')
xlabel('Sieve size (m)');
```

```
axis([1e-5 10 0 100])
eval(['saveas(gcf,"/Users/Sheldon/Desktop/grain size plots/',comp,'comp.jpg")']);



%% Contour
load T3F2.mat

pp = ones(4);
for ii = 1:4
   for j = 1:4
      px = strcat('c',int2str(ii),int2str(j));
      px1 = eval([px '(:,1)'])/110;px2 = eval([px '(:,2)']);
      eval(['fiftyp=px1' '(round(' 'px2'  '*10)/10==0.5)'])
      if isempty(fiftyp) == 0
         pp(ii,j) = fiftyp(1) ;
      else
         pp(ii,j) = 0;
      end

   end
end
x = 1:4; y = 1:4;
xmin = 1; ymin = 1; xmax = 4; ymax = 4;
xv = linspace(xmin, xmax, 100);
yv = linspace(ymin, ymax, 100);
[Xinterp,Yinterp] = meshgrid(xv,yv);
Zinterp = griddata(x,y,pp,Xinterp,Yinterp);

contourf(flipud(Zinterp))
```

```
set(gcf,'color','w');



%% Lianna 92kg samples
load lia_plot.mat
semilogx(lia_plot(:,1)/1000,lia_plot(:,2),'o-','LineWidth',2)
xlabel('Diameter (m)','FontSize',15);ylabel('Percent passing (%)','FontSize',15)
saveas(gcf,'/Users/Sheldon/Desktop/grain size plots/Lianna.jpg')

%%
cT3W = imread('/Users/Sheldon/Desktop/grain size plots/T3W.jpg');
cvT3W = imread('/Users/Sheldon/Desktop/grain size plots/cT3Wlog.jpg');
cvlT3W = imread('/Users/Sheldon/Desktop/grain size plots/cT3Wlog.jpg');
%subplot(2,2,[1 2]);
%imshow(cT3W,[]);
subplot(121);
imshow(cvT3W);
subplot(122);
imshow(cvlT3W);
saveas(gcf,'/Users/Sheldon/Desktop/grain size plots/curveT3W.jpg')



%% plot diameter vs. surface area
% [diam, mass_fraction, tot_surf, tot_surf./mass_fraction];
load refs.mat;set(0,'defaultlinelinewidth',.1);
close all
%color = {'r','g','b'};%sty = {'-','-o',':','-+','-v','-.'};
 color = {'-k.','.k-','.k-'};
for k = 1:6
```

```
    eval(['load ' char(refs(k,1))]) % load each face
    for ii = 1:3
        for j = 1:6
            px = strcat('c',int2str(ii),int2str(j), 's' );
            eval(['semilogx(' px '(:,1)' ',' px '(:,3)' ','...
                '" color{ii} '" ')']) 
            hold on

        end
    end
end
xlabel('Grain size (m)','FontSize',15);ylabel('Surface area (m2)','FontSize',15);
axis([10e-6 10 0 1.1])
title('Surface area distribution','FontSize',20)
saveas(gcf,'/Users/Sheldon/Desktop/grain size plots/surf.jpg')
%% plot diam vs. mass
% [diam, mass_fraction, tot_surf, tot_surf./mass_fraction];
load refs.mat
close all
%color = {'r','g','b'};%sty = {'-','-o',':','-+','-v','-.'};
color = {'k.-','.-k','.-k'};
mass_matrix=[];
for k = 1:6
    eval(['load ' char(refs(k,1))]) % load each face
    for ii = 1:3
        for j = 1:6
            px = strcat('c',int2str(ii),int2str(j), 'b' );
            eval(['semilogx(' px '(:,1)' ',' px '(:,2)' ','...
                '" color{ii}  '" ')']) 
            hold on
```

```
        end
    end
end

axis([10e-6 10 0 .3])
title('Mass distribution','FontSize',20)
xlabel('Grain size (m)','FontSize',15);ylabel('Mass of fraction ','FontSize',15);
saveas(gcf,'/Users/Sheldon/Desktop/grain size plots/mass.jpg')
%% plot moments
load refs.mat

mean_all = []; std_all = []; skew_all = []; kur_all = [];



for k = 1:6
    eval(['load ' char(refs(k,1))]) % load each face

    for ii = 1:3
        for j = 1:6
            px = strcat('c',int2str(ii),int2str(j), 'm' );
            eval(['std_all = [std_all;' px '(2)];' ])
            eval(['mean_all = [mean_all;' px '(1)];' ])
            eval(['skew_all = [skew_all;' px '(3)];' ])
            eval(['kur_all = [kur_all;' px '(4)];' ])
        end
    end
end

close all
subplot(221)
```

```
hist(mean_all)
h = findobj(gca,'Type','patch');set(h,'FaceColor','k','EdgeColor','w')
xlabel('Mean','FontSize',15);ylabel('Count','FontSize',15);
subplot(222)
hist(std_all);
h = findobj(gca,'Type','patch');set(h,'FaceColor','k','EdgeColor','w')
xlabel('Standard Deviation (Sorting)','FontSize',15);
ylabel('Count','FontSize',15);
subplot(223)
hist(skew_all)
h = findobj(gca,'Type','patch');set(h,'FaceColor','k','EdgeColor','w')
xlabel('Skewness','FontSize',15);ylabel('Count','FontSize',15);
subplot(224)
hist(kur_all)
h = findobj(gca,'Type','patch');set(h,'FaceColor','k','EdgeColor','w')
xlabel('Kurtosis','FontSize',15);ylabel('Count','FontSize',15);
saveas(gcf,'/Users/Sheldon/Desktop/grain size plots/stats.jpg')

%%
stats_all = [mean_all std_all skew_all kur_all];
save stats_all.txt stats_all -ASCII
```

Appendix C

This section lists the formulae used for method of moment calculations. Grain size diameters are converted to logarithmic Udden–Wentworth grade scale using $\phi = -\log_2 d$ where ϕ is converted Udden–Wentworth grade scale value and d is grain diameter in millimeters. The formulae are mortified from (Krumbein and Pettijohn, 1938).

$$\bar{x}_\phi = \frac{\sum f m_\phi}{100},$$

$$\sigma_\phi = \sqrt{\frac{\sum f(m_\phi - \bar{x}_\phi)^2}{100}},$$

$$Sk_\phi = \frac{\sum f(m_\phi - \bar{x}_\phi)^3}{100\sigma_\phi^3},$$

$$K_\phi = \frac{\sum f(m_\phi - \bar{x}_\phi)^4}{100\sigma_\phi^4}$$

where f is the frequency in percent,

m_ϕ is the mid-point of each fraction in ϕ-scale,

σ_ϕ is standard deviation,

Sk_ϕ is skewness, and

K_ϕ is Kurtosis.

Reference

Krumbein, W.C., Pettijohn, F.J. 1938. Manual of Sedimentary Petrography. Appleton-Century-Crofts: New York.